Nonlinear Internal Waves on the Washington Continental Shelf

Shuang Zhang

A thesis submitted in partial fulfillment of
the requirements for the degree of

Doctor of Philosophy

University of Washington

2014

Reading Committee:

Matthew H. Alford, Chair

Michael C. Gregg

Parker MacCready

Program Authorized to Offer Degree:
UW School of Oceanography

University of Washington

Abstract

Nonlinear Internal Waves on the Washington Continental Shelf

Shuang Zhang

Chair of the Supervisory Committee:
Dr. Matthew H. Alford
School of Oceanography, Applied Physics Laboratory

This dissertation studies nonlinear internal waves (NLIW) on the Washington (WA) continental shelf based on 4 years' records from a moored ADCP/thermistor chain. A strong, variable wave field is documented along with their general characteristics, generation, transport, instabilities and spatial features. Mostly propagating onshore towards the northeast, NLIWs take a variety of forms, including internal solitary waves, solitary wave trains and bores, but nearly all are mode-1 depression waves that arrive semi-diurnally along with the internal tide. The NLIW energy flux is correlated with the internal tide energy flux but not the local barotropic forcing, implying that the observed NLIWs arise primarily from shoaling remotely generated internal tides rather than local generation. Estimated onshore transport by the waves can equal or exceed offshore Ekman transport, suggesting the waves may play an important role in the mass balance on the WA continental shelf.

Breaking NLIWs with overturning instabilities are examined and their Thorpe-scale-inferred turbulence documented. Categorized based on the instability mechanisms by which NLIWs induce mixing, waves are identified as shear-instability (Type I) and convective instability (Type II) waves using a Froude number criterion. Composites are constructed by averaging over all waves in each category to examine the

mean depth structure of dissipation and their relationship with the background parameters for each category, suggesting highest turbulence at the sheared interface for Type I waves and throughout the wave core for Type II.

NLIWs exhibit strong spatial variability at 6 synchronous mooring arrays deployed on the WA continental shelf. Based on their regular arrivals on 3 moorings, the same waves can be detected between mooring pairs and their travel times recorded. Using ray-tracing techniques with impacts from bathymetry only, the wave travel time is estimated as a function of wave amplitude and propagation direction. The comparison between the predicted wave travel time and observation is provided.

TABLE OF CONTENTS

LIST OF FIGURES

LIST OF TABLES

ACKNOWLEDGMENTS

I would like to express my sincerest gratitude to my advisor Matthew Alford for his extraordinary support, patience and guidance through this work. This thesis would not have been completed without all his encouragement and effort.

I also offer my sincere gratitude to Mike Gregg, Parker MacCready and Jan Newton for serving on my supervisory committee and for giving valuable suggestions, encouragement and critique. My special thanks go to John B. Mickett for his tremendous contribution to the project and being a co-author in the first chapter. My thanks also go to Barbara Hickey and Ryan McCabe for discussions on the Washington coastal environment and ecosystem; Zhongxiang Zhao for helping with data analysis and suggestions on the research; Gunnar Voet, Barry Ma, Andy Pickering, Brian Chinn, Byron Kilbourne and Jun-Hong Liang for their generous and valuable discussions.

This work was supported in part by the National Oceanic and Atmospheric Administration (NOAA) under the US IOOS grant to NANOOS, NA11NOS0120036, and the National Science Foundation under grant OCE0968131. The considerable hardware and instrumentation comprising the surface and subsurface moorings was purchased on a generous grant from the Murdock Charitable Trust. We thank three anonymous reviewers for their generous inputs. Thanks are extended to the Captain and crew of the R/V Thomas G. Thompson for deploying and servicing the moorings; Eric Boget, Mike Carpenter, Sam Fletcher, Mike Kenney, Trina Litchendorf, Keith Magness, Tim McGinnis, Nick Michel-Hart, Zoë Parsons, Chris Siani and Tim Wen

for the design and construction of the NEMO system; the U.S. Coast Guard station in La Push, Washington, for their hospitality and willingness to host our shore data station; Quileute for their tribal support in onshore loading and Jennifer Hagen for her contribution during cruises to deploy/recover ChaBa; and the Olympic Coast National Marine Sanctuary (OCNMS) for their assistance and cooperation in buoy logistics.

DEDICATION

to my dear family

Chapter 1

INTRODUCTION

In general, this thesis studies nonlinear internal waves (NLIW) on the Washington (WA) continental shelf, investigating the following questions: 1) what do they look like, 2) what are their sources and sinks, 3) why do we care about them, and 4) how can we predict them. In this chapter, an introduction to these topics is presented, followed by an overview of the thesis.

1.1 Nonlinear internal waves on continental shelves

Nonlinear internal waves (NLIW) are commonly observed on continental shelves around the globe, wherein they often appear as sharp depressions of the near-surface thermocline with opposing horizontal flows above and below. NLIWs can often be seen in the space-borne synthetic aperture radar (SAR) images (*Apel et al.*, 1985; *Farmer and Armi*, 1999; *Scotti and Pineda*, 2004), as shown by a SAR image over the Washington coast (Figure 3.1). Occurring along with the internal tide or not, most waves are observed as internal solitary waves in packets or trains (Figure 1.2). On some other occasions, the isopycnals do not return to their original rest states after the solitary waves have passed, suggesting internal bore behaviors (Figure 1.2). Most recent observational studies reported observations of NLIWs off the Oregon coast *Stanton and Ostrovsky* (1998); *Klymak and Moum* (2003); *Moum et al.* (2007a,b); *D'Asaro et al.* (2007), the New Jersey coast (*Shroyer et al.*, 2010a, 2011), Massachusetts Bay (*Scotti et al.*, 2006, 2008), and the South China Sea (*Duda et al.*, 2004; *Klymak et al.*, 2006; *Alford et al.*, 2010; *Lien et al.*, 2012). A summary of selected studies in Table 1.1

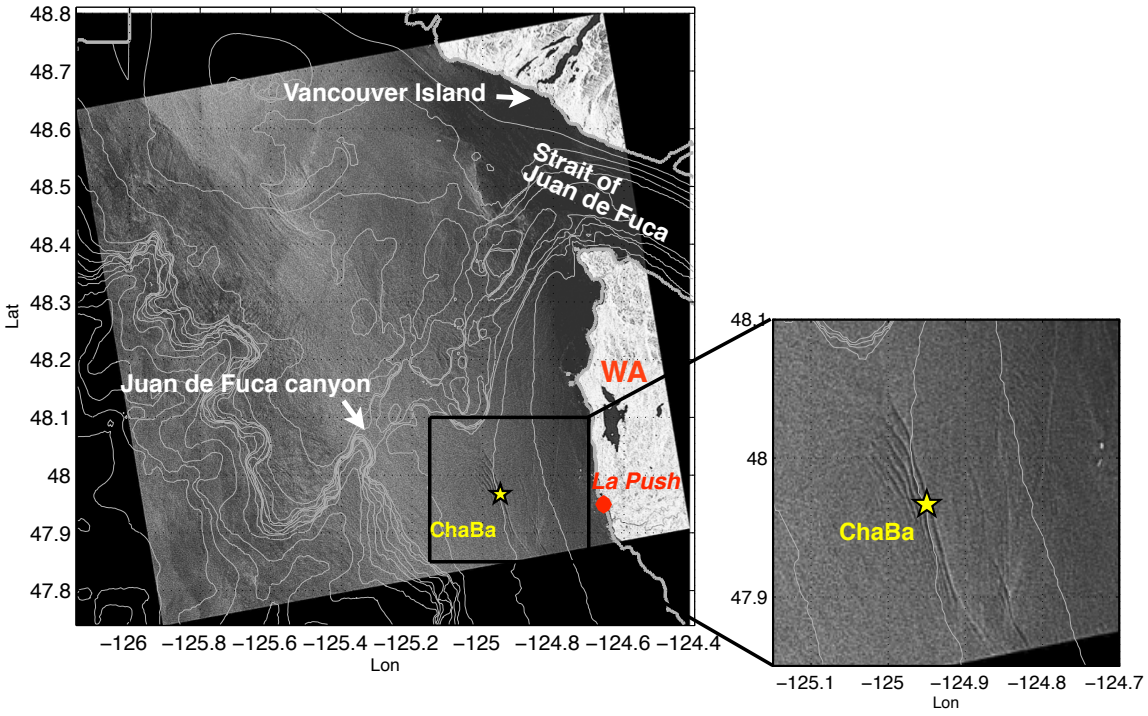

Figure 1.1: A SAR image captured by Radarsat-2 on July 16, 2011, 02:09:21 UTC with bathymetry super-imposed. The zoom-in plot shows a nonlinear internal wave train.

suggests the commonly observed NLIW amplitudes on continental shelves in relation to water depth.

A variety of generation mechanisms are possible for NLIWs in coastal oceans, mostly including 1) the formation of lee waves during one phase of the barotropic tide over ridges and banks, which are released when the flow relaxes (e.g. *Lee and Beardsley* (1974); *Farmer and Smith* (1980)), and 2) the steepening of internal tides as they shoal (e.g., *Gerkema* (1995); *Colosi et al.* (2001); *Lien et al.* (2005)). By mechanism 2), steepened internal tidal fronts normally form rank-order internal solitary wave packets under effects of nonlinearity and dispersion (e.g. *Helfrich and Melville* (2006)) as they continue to grow. Some coastal locations give rise to internal tides

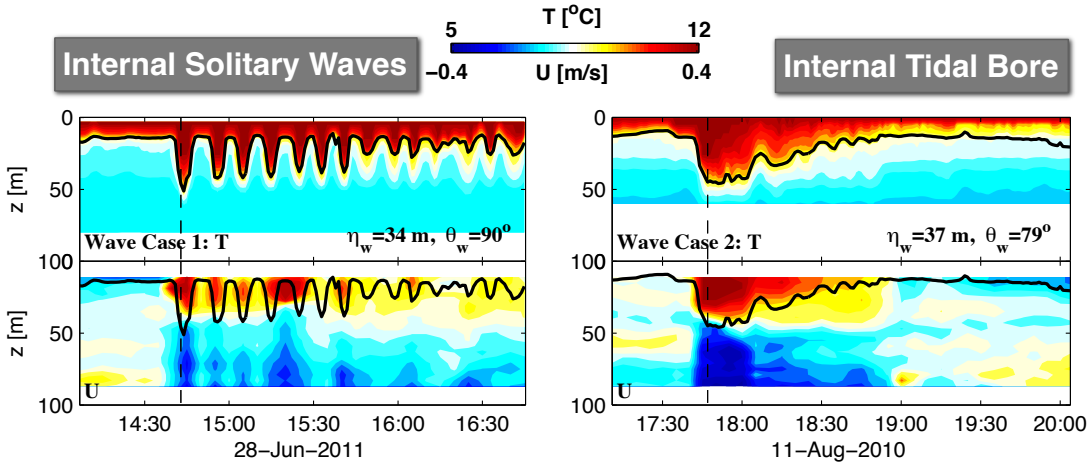

Figure 1.2: Examples of a solitary wave train (left) and a internal bore (right), showing temperature and velocity time series from a moored ADCP/thermistor chain.

Table 1.1: Selected studies of nonlinear waves observed on continental shelves and their amplitudes in relation to water depth. Table 1 in *Alford et al.* (2012).

Location	*H (m)*	*Max. Wave Ampl. (m)*	*Ratio*	*Reference*
New England Shelf	70	18	0.26	*MacKinnon and Gregg* (2003)
	147	30	0.20	*Colosi et al.* (2001)
New Jersey Shelf	70	15	0.21	*Shroyer et al.* (2011)
Oregon Shelf	80	< 20	< 0.25	J. Moum, pers. comm.
Scotia Shelf	80	25	0.31	*Sandstrom and Elliott* (1984)
	160	50	0.31	*Sandstrom and Oakey* (1995)
Okhotsk Sea	70	< 20	< 0.29	*Nagovitsyn et al.* (1991)
South China Sea	400	140	0.35	*Lien et al.* (2012)
Washington Shelf	**100**	**38**	**0.38**	**this study**

and NLIWs that are phase-locked with individual flood/ebb events. The occurrence of such dynamics usually requires sufficiently constrained geometry and tidal signals significantly stronger than either the mesoscale or other broadband internal motions (*Nash et al.*, 2012). In contrast, tidally-generated internal waves that have been radiated far from their origins may undergo propagation speed and path alteration via the spatial structure of background currents, stratification, and the mesoscale variability (e.g., *Zilberman et al.* (2011)), and are subject to decay due to dissipation (e.g., *Moum et al.* (2007a)). As a result, the generation and evolution of NLIW on the continental

shelves can become incoherent and variable (*Nash et al.*, 2012).

Nonlinear waves are of particular interest in coastal environments for their potential to transport mass and enhance mixing. NLIWs are capable of transporting mass through Stokes drift, potentially contributing to cross-shelf exchange (*Huthnance*, 1995). They can also trap parcels of water within wave cores and carry them appreciable distances due to their nonlinearity (*Lamb*, 2002; *Lien et al.*, 2012). Because of this, their capability for transporting nutrients, larvae, sediment and pollutants in coastal environments has long been acknowledged (*Sandstrom and Elliott*, 1984; *Bogucki et al.*, 1997; *Pineda*, 1999; *Klymak and Moum*, 2003).

The rapid and strong vertical displacements and sheared horizontal flows of NLIWs make them efficient at mixing. Observations of high turbulence levels within NLIWs have been reported (*Sandstrom and Oakey*, 1995; *Stanton and Ostrovsky*, 1998; *Duda and Farmer*, 1999; *Moum et al.*, 2003), making them an important mechanism for mixing in coastal regions (*Moum et al.*, 2007a,b; *D'Asaro et al.*, 2007). NLIWs create conditions favorable for instabilities and can produce mixing up to one half of the mid-water-column dissipation on continental shelves (e.g., *MacKinnon and Gregg* (2003)), as suggested by an example of breaking NLIWs in Figure 1.3. Accordingly, patterns of nutrients and other materials fluxed across the shelf by these waves will depend on the strength and time/space dependence of the mixing.

1.2 Washington (WA) Continental Shelf

Embedded in the California Current System (CCS), the Washington (WA) continental shelf (Figure 3.1) is a highly productive, topographically complex region. Dominated by a seasonal wind-driven circulation, northerly winds are predominant off the WA coast in summer/early fall, generating a cross-shelf density gradient that sus-

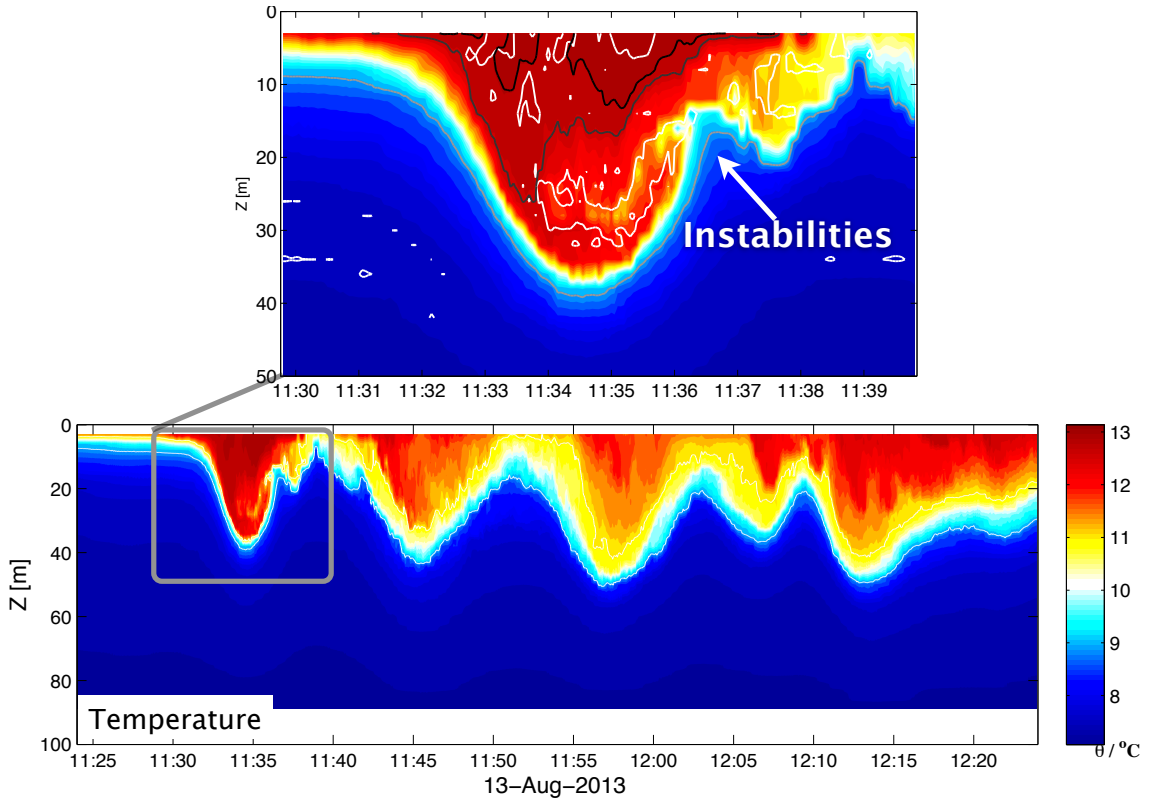

Figure 1.3: An example of a solitary wave with temperature overturning instabilities (white contours).

tains a southward shelf current. In winter/spring, winds are predominantly southerly, resulting in a northward shelf current and effectively reversing the cross-shelf circulation pattern. Seasonally averaged chlorophyll concentrations on the WA coast are several times higher than that off northern California, where the upwelling-favorable wind is several times greater (*Hickey and Banas*, 2008). The high productivity off the WA coast remains a puzzle but possibly owes to a number of oceanographic and topographic factors which may catalyze nutrient supply to the euphotic zone, e.g, submarine canyons along continental slopes(*Hickey*, 1995; *Waterhouse et al.*, 2009; *Allen and Hickey*, 2010), the Juan de Fuca eddy (*MacFadyen et al.*, 2008), and the Columbia river (*Stansfield et al.*, 2001; *Hickey and Banas*, 2003). Most recently, strong

internal tides and NLIWs in this region are reported (*Alford et al.*, 2012), potentially representing another important mechanism that can produce boosted nutrient concentrations in this region.

Although NLIWs have been studied in various coastal areas, no previous studies have reported a detailed observation of the internal waves on the WA continental shelf, mostly due to a lack of data to detect these waves in this region. A new observing system consisting of two moorings and a glider line off the WA coast has recently been designed and deployed since Year 2010, capturing strong internal tide and NLIW signals in the records. Particularly, NLIWs observed in this system appear to feature some of the strongest waves reported on continental shelves when viewed as a fraction of the water depth, exerting high potential in turbulence and mixing enhancement.

1.3 Overview of thesis

Overall, this thesis aims to deepen our understanding of NLIWs on the WA continental shelf based on a new observing system that was established and maintained during Year 2010-2013, focusing on the questions related to their characteristics, generation, propagation, transport and instabilities.

In Chapter 2, four summers/falls of temperature, salinity and velocity records from a surface mooring are used to document characteristics of nonlinear internal waves on the WA continental shelf. A large number (> 1500) of NLIWs are detected and their taxonomy (internal solitary waves, solitary wave trains and internal bores) documented. Possible wave generation mechanisms are explored, suggesting NLIWs are generated by shoaling of remotely-incident internal tides (IT) instead of by local barotropic conversion. Estimated time-mean onshore transport due to NLIWs is significant compared to the Ekman transport, suggesting the waves may be an important

mechanism for cross-shore exchange during these periods. Chapter 2 is identical to *Zhang et al.* (submitted), written with co-authors M. H. Alford and J. B. Mickett.

Chapter 3 explores instabilities in NLIWs, using data from a moored dense thermistor string accompanied by velocity measurements on the WA shelf. Waves with two types of instability mechanisms are identified, i.e., shear instabilities (Type I) and convective instabilities (Type II), similar to those identified by *Lamb* (2014) and *Shroyer et al.* (2010a). Strong temporal variability exists in mid-column NLIW-induced mixing, with strong, regular NLIWs being a dominant mixing mechanism when winds are weak. Composites of the wave-induced dissipation rate suggest that Type I waves have high dissipation confined to the trailing edge of waves, in regions of high shear, while Type II waves show elevated dissipation distributed throughout the wave core. Chapter 3 is identical to *Zhang and Alford* (submitted), written with co-author M. H. Alford.

Chapter 4 studies spatial variability and propagation of NLIWs, based on a mooring series spaced on the WA continental shelf in 2013. The waves' structures are documented as they cross the WA continental shelf and their travel times are inferred between multiple moorings using their arrivals. Theoretical estimation of wave' travel time is provided and compared to observation, suggesting that the waves' propagation is controlled by the bathymetry, and is susceptible to the existence of a strong background current. Chapter 4 is written with co-author M. H. Alford.

Chapter 2

CHARACTERISTICS, GENERATION AND MASS TRANSPORT OF NONLINEAR INTERNAL WAVES ON THE WASHINGTON CONTINENTAL SHELF

2.1 Introduction

Nonlinear internal waves (NLIWs) have been detected around the globe with a wide variety of *in situ* and remote techniques as reviewed by *Ostrovsky and Stepanyants* (1989) and *Apel et al.* (2006). Recent observational studies of NLIWs on continental shelf regions such as the Oregon coast (*Stanton and Ostrovsky*, 1998; *Klymak and Moum*, 2003; *Moum et al.*, 2007a,b; *D'Asaro et al.*, 2007), the New Jersey coast (*Shroyer et al.*, 2010a, 2011), Massachusetts Bay (*Scotti et al.*, 2006, 2008), and the South China Sea (*Duda et al.*, 2004; *Klymak et al.*, 2006; *Alford et al.*, 2010; *Lien et al.*, 2012) show that NLIWs in coastal oceans are frequent and energetic. They have been observed to transport energy (e.g., *Moum et al.* (2007b); *D'Asaro et al.* (2007)) and mass (e.g., *Inall et al.* (2001); *Shroyer et al.* (2010b)), and to serve as an effective mechanism for mixing (e.g., (*MacKinnon and Gregg*, 2003; *Moum et al.*, 2007a)), making them a potential contributor to vertical nutrient and heat flux over the shelf (e.g. *Shroyer et al.* (2010b)). For these reasons, NLIWs can also affect biological distributions (e.g., *Pineda* (1991); *Scotti and Pineda* (2007)), sediment resuspension (e.g., *Bogucki et al.* (1997); *Klymak and Moum* (2003)) and underwater acoustics (*Apel et al.*, 2006).

In coastal oceans, NLIWs are usually believed to be generated either by (i) the release of internal lee waves or hydraulic jumps generated by barotropic tidal flow

over topographic features (e.g. *Lee and Beardsley* (1974); *Farmer and Smith* (1980); *Maxworthy* (1980); *Farmer and Armi* (1999)); or (ii) nonlinear transformation of the baroclinic (internal) tide as it propagates over slope-shelf topography (e.g., *Gerkema* (1995); *Colosi et al.* (2001); *Lien et al.* (2005); *Helfrich and Grimshaw* (2008); *Alford et al.* (2010); *Nash et al.* (2012)). In mechanism (ii), internal tides in coastal regions usually come from multiple locations (e.g., *Nash et al.* (2012); *Alford et al.* (2012)), possibly including remote and local sources. A superposition of multiple internal tides may produce NLIWs with mixed properties and result in no particular phase relationship with the barotropic tide (*Inall et al.*, 2000; *Nash et al.*, 2012). Additionally, variations in phasing between internal/barotropic tides and their oblique angle of incidence on the irregularly-shaped continental shelf would be expected to modulate the formation, shape and propagation of the waves.

NLIWs can take a large variety of shapes and properties, including bores, undular bores, solitary waves, and wave trains (e.g., *Ostrovsky* (1978); *Gerkema* (1995); *Henyey and Hoering* (1997); *Stepanyants* (2006)). The morphology and evolution of NLIWs have been analyzed in previous numerical and laboratory studies (e.g., *Maxworthy* (1980); *Helfrich and Melville* (1986)), but the factors determining the shape and size of NLIWs are poorly understood.

NLIWs are capable of transporting mass through Stokes drift and/or trapped cores, potentially contributing to cross-shelf exchange (*Huthnance*, 1995). *Shroyer et al.* (2010b) reported that the onshore transport by NLIWs over a short period of time on the New Jersey shelf was comparable to a weak downwelling wind sustained over a much longer time, as also found on the Malin Shelf (*Inall et al.*, 2001). An extreme case of NLIW mass transport is a trapped core, wherein waves trap water and carry it appreciable distances (*Lamb*, 2002; *Lien et al.*, 2012). Plankton accumulation and transport in propagating nonlinear internal fronts have been reported and

explored (e.g., *Pineda* (1999); *Scotti and Pineda* (2004)), as well as sediment resuspension and transport of bottom material (*Bogucki et al.*, 1997; *Klymak and Moum*, 2003).

The Washington (WA) continental shelf (Figure 2.1a) is a highly productive, topographically complex region. Flow is generally dominated by a strong seasonal shelf current (southward in summer and northwestward in winter), primarily driven by winds that shift direction from northwesterly (upwelling-favorable) in summer to southerly (downwelling-favorable) in winter (*Hickey*, 1989; *Hickey and Banas*, 2003). Seasonally averaged chlorophyll concentrations on the WA coast are several times higher than off northern California, where the upwelling-favorable wind is several times greater (*Hickey and Banas*, 2008). The high productivity off the WA coast remains a puzzle but possibly owes to 1) submarine canyons along continental slopes which can enhance upwelling (*Hickey*, 1995; *Waterhouse et al.*, 2009; *Allen and Hickey*, 2010); 2) a strong seasonal mesoscale feature known as the Juan de Fuca eddy (*MacFadyen et al.*, 2008); 3) the Juan de Fuca Strait and 4) the Columbia river (*Stansfield et al.*, 2001; *Hickey and Banas*, 2003). These factors, individually or together, may catalyze nutrient supply to the euphotic zone. Most recently, strong NLIWs in this region are reported (*Alford et al.*, 2012), potentially representing another important nutrient-supply mechanism. One example of a 6-trough solitary wave train propagating onshore was captured by a high-resolution Synthetic Aperture Radar (SAR) over this region on July 16, 2011, 02:09:21 UTC (Figure 2.1b). The same wave train was detected from surface mooring *"ChaBa"* (Figure 2.1d), deployed in 100-m deep water off the WA coast. Based on the mooring record, the wave train has a total of 6 solitary waves, with a largest wave of 28 m and a mean propagation direction towards $\sim 55^o$ True (details in Section 3.2), consistent with the SAR image.

In this study, four summer/fall time series of data from the *"ChaBa"* mooring are

used to document > 1500 observed waves (Figure 2.2), and the background conditions that affect them. A distinct advantage of this dataset is that a variety of wave types (Figure 2.3) and background conditions are captured in the long time series. Therefore, the temporal variations and potential relationships between NLIWs and background currents, stratification and the internal tide can be investigated. One limitation of this dataset, however, is errors arising from non-ideal vertical and temporal sampling. These are carefully examined in the analysis. The goals of this study are to 1) document the highly variable morphologies and properties of the NLIWs (amplitude, velocity, propagation direction, energetics and seasonal features); 2) obtain clues to their generation mechanism by examining their relationship with background conditions and the internal tide; and 3) estimate the onshore mass transport due to the waves and its possible implications.

This chapter is organized as follows. The experimental setup, data and techniques are presented in Section 3.2, including calculations of wave properties and errors associated with sampling using the dataset. Main results are presented in Section 2.3, including the oceanographic context (Section 2.3.1), basic wave features and their statistics (Section 2.3.2), their relationship with the internal tide (Section 2.3.3), and their on-shore transport (Section 2.3.4), followed by a discussion in Section 4.5 and conclusions in Section 3.7.

2.2 Experimental details

2.2.1 Data

Observations are from the *"ChaBa"* surface mooring and Seaglider *SG187*, both maintained by University of Washington as aspects of the Northwest Association of Networked Ocean Observing Systems (NANOOS). *ChaBa* (47^{o}58.0′N, 124^{o}57.0′ W)

was deployed for four successive summers/falls (July 17 - October 17 in 2010, May 22 - August 29 in 2011, May 27 - November 20 in 2012, and April 24 - September 23 in 2013) in 100-m deep water about 25 km off La Push, WA (Figure 2.1, 2.2). *ChaBa* consists of a surface buoy housing meteorological instruments and communication, a subsurface instrument cage, and a string of instruments mounted along an 81-m mooring wire. A 230-kg depressor weight keeps the wire vertical, while a length of chain below keeps the instruments within a 100-m watch radius of the anchor on the seafloor. Data used in this study mainly include temperature and salinity measurements from conductivity-temperature-depth (CTD) sensors and velocity records from an acoustic Doppler current profiler (ADCP) mounted in the subsurface cage. During 2010-2012, temperature was measured at depths 0.5, 5, 11, 15, 20, 26, 40, 51, 60 m and 80-m (Figure 2.2, panels c, f, i; no 80-m sensor in 2010) with Seabird Electronics (SBE) 37 MicroCAT CTDs and SBE 39 T-loggers. Salinity was measured at depths 0.5, 11, 26 and 51 m by SBE 37s. The SBE 39s sampled every minute and the SBE 37s sampled every two minutes. In 2013, 40 SBE 56 T-loggers spaced over a 2-m interval between the surface and 80-m depth were added to the mooring, sampling temperature every 3 seconds over the battery lifespan (Figure 2.2*l*). A downward-looking 300 kHz Workhorse ADCP at 3-m depth recorded near-full-depth velocity profiles every 5 minutes in 2010-2012 (Figure 2.2, panels d, g, j), and every 1 minute in 2013 (Figure 2.2m) over a two-month period. Wind measurements are from National Data Buoy Center (NDBC) Station 46041 at Cape Elizabeth, located at $47^o21.0'$ N, $124^o42.5'$ W, about 60 km away from *ChaBa* to the southeast (Figure 2.1a, 2.2a). Other oceanic and meteorological properties, e.g., oxygen, nitrate, chlorophyll, pH, pCO_2 were sampled on the mooring wire or from the surface buoy, but are not discussed in this paper. Near-full-depth profiles of temperature and salinity complementing the vertically discrete *ChaBa* data are from Seaglider *SG187*, which ran across the WA continental slope/shelf between 47^o N, 127^o W and 48^o N, 125^o W (Figure 2.1, ac) during 2010 - 2012, giving a profile every 4 - 9 hours, depending on water depth.

2.2.2 Methods

Time series of temperature (T) and alongshore velocity (U) over the full deployment in 2010-2013 (Figure 2.2) illustrate a marked semidiurnal internal tide, along with large spikes indicating nonlinear internal waves in their zoom-in plots (Figure 2.3). In this section, we document techniques used to calculate the wave properties and discuss potential errors due to sampling.

Baroclinic velocities

Because wave-induced mooring motion is essentially vertically uniform, it contaminates the depth-averaged measured velocity $\mathbf{u}_{\mathrm{BT}}$ but not the baroclinic velocity $\mathbf{u}_{\mathrm{BC}}$ on timescales of seconds to minutes. Profiles of total velocity are constructed by first removing the depth-mean, time averaging the depth-mean over a three-point median filter to remove the mooring motion, and then adding it back to the depth-varying values. We define the baroclinic velocities as $\mathbf{u}_{\mathrm{BC}} = \mathbf{u} - \mathbf{u}_{\mathrm{BT}}$, where $\mathbf{u}_{\mathrm{BT}}$ is the corrected depth-average flow, and $\mathbf{u}$ is corrected total velocity. $\mathbf{u}_{\mathrm{BC}}$ is not affected by mooring motion.

Estimation of stratification N^2

Measurements of salinity (S) from SBE 37s on the mooring are sampled every two minutes and with a lower vertical resolution than T. Values of S at depths where only T is measured are estimated from a slowly-varying T-S relationship, using a linear piece-wise T-S fit from the mooring data or glider data when available. Details of the T-S fit and calculation of the stratification profile $N^2(z)$, where $N = \sqrt{\frac{g}{\rho}\frac{\partial \rho}{\partial z}}$ is the

buoyancy frequency, g is gravitation acceleration, ρ is potential density, are described in Appendix.

Semidiurnal tide quantities

Semidiurnal barotropic and baroclinic tides are extracted from the moored records via bandpass filtering. The internal tide velocity, vertical displacement, energy, energy flux and their modal decompositions are calculated following standard procedures (e.g., *Alford and Zhao* (2007)). Mode-1 internal tides are obtained from the filtered time series by performing a least square inverse.

Calculation of NLIW properties

a) Amplitude. Wave amplitude η_w is defined as the maximum isotherm displacement inside the wave event, i.e. $\eta_w = \eta(z,t_w)|_{max}$, where $\eta(z,t_w) = z(t_0) - z(t_w)$, $z(t_w)$, $z(t_0)$ are the isotherm depth during the wave event and in the reference state, respectively. An example of the calculation of $\eta(z)$ is illustrated in Figure 2.4, where $\eta(z,t_w)$ is calculated as the vertical distance between the temperature profiles inside the wave ($T(z,t_w)$) and the reference state ($T(z,t_0)$). The difficulty in the designation of the reference state t_0 has been described in *Shroyer et al.* (2010a). We define t_0 to be 15 min before wave arrives. η_w is defined positive for depression waves, as no elevation waves are detected. Perturbations with $\eta_w > 10$ m are classified as NLIWs.

b) Velocity and direction. The horizontal wave velocity vector in Earth coordinates ($\mathbf{u}_w = (u_w, v_w)$) is calculated as velocity measurements in the wave event minus the background flow (*Chang et al.*, 2011), i.e. $\mathbf{u}_w(z) = \mathbf{u}(z,t_w) - \mathbf{u}(z-\eta(z),t_0)$, in which $\mathbf{u}(z,t_w)$ and $\mathbf{u}(z-\eta(z),t_0)$ are the measured velocities inside the wave and their background states along isopycnals, respectively. t_0 is again defined as 15 min

before the wave arrival. Mode-1 depression waves have opposing deep/shallow flows, such that the wave propagation direction θ_w is consistent with the direction of the shallow flow. Therefore θ_w is calculated as $tan^{-1}\frac{v_w(z)}{u_w(z)}$ in the shallow flow following *Chang et al.* (2011), using the fitted slope of v_w over u_w. The horizontal wave velocities in wave coordinates (U_w, V_w) are calculated by rotating u_w, v_w towards the wave propagation direction. Because the motion of the surface buoy renders vertical motions unusable (*Alford et al.*, 2012), the vertical wave velocity W_w is estimated by $\frac{\Delta\eta(z)}{\Delta t}$, which is usually an order of magnitude smaller than the horizontal velocities, similar to other observational studies (e.g., *Moum et al.* (2003); *Lien et al.* (2013)).

Errors in θ_w are estimated by comparing θ_w within the same wave train, under the assumption that waves within a train propagate in the same direction. Wave trains consisting of three or more waves are used in this analysis and θ_w usually has a standard deviation of $\sim 8^o$ (e.g., Figure 2.1 and Figure 2.3, Case 2), with a maximum difference of $\sim 20^o$ between the waves.

c) Phase speed. For energy flux, we require knowledge of the phase speed c, as the phase speed equals the group speed for non-dispersive waves. We do not have direct observations of c, and mooring motion precludes calculation of c from the lateral separation of the ADCP beams following *Scotti et al.* (2005). Instead, c is estimated from the Dubreil-Jacotin-Long (DJL) model (*Long*, 1953; *Stastna and Lamb*, 2002), i.e.

$$\bigtriangledown^2\eta + \frac{\partial_z\bar{U}(z-\eta)}{c_{\mathrm{DJL}} - \bar{U}(z-\eta)}[\partial_x^2\eta + (1-\partial_z^2\eta)^2 - 1] + \frac{\bar{N}^2(z-\eta)}{[c_{\mathrm{DJL}} - \bar{U}(z-\eta)]}\eta = 0 \qquad (2.1)$$

where η is the displacement, $\bigtriangledown^2 = (\partial_x^2 + \partial_z^2)$ (x, z is the horizontal and vertical direction in wave coordinates), $\bar{U}$ and $\bar{N}$ are the background velocity and stratification, respectively, and c_{DJL} is the calculated phase speed. Because it is fully nonlinear

and non-hydrostatic, the DJL model is a decent simulation of these waves in terms of wave shape and phase speed, and is applicable for steady waves of all amplitudes (*Stastna and Lamb*, 2002; *Henyey*, 1999; *Lamb*, 2003; *Lien et al.*, 2012). The steady approximation is a good one at our site considering the relatively flat bottom. Previous observational studies suggest that c_{DJL} is typically within 10% of the observed c (*Lien et al.*, 2012). This error in our estimation of phase speed is projected onto the wave energy, energy flux and transport calculations, which are discussed later in this paper.

d) Duration time and wave width. The wave duration time τ_w is defined as that between the start and end of a wave event, i.e., between the times when the isopycnal displacement is greater than 2% of the maximum isotherm displacements before and after wave arrivals. Wave width at half amplitude $\lambda_{1/2}$ is that between the half downwelling and upwelling displacement, estimated from time series with the assumption that $c = c_{\mathrm{DJL}}$, which introduces about 10 % error into the calculation.

e) Energetics. The wave energy is the sum of available potential energy and kinetic energy. Available potential energy density $E_a(z)$ (units: J m^{-3}) is calculated following *Scotti et al.* (2006) and *Lamb* (2007), as

$$E_a(z) = g \int_{\bar{\rho}(z)}^{\rho(z)} [z - z_0'(s)] ds \tag{2.2}$$

in which $\rho(z)$, $\bar{\rho}(z)$ are the density profiles inside the wave and in the reference state, respectively; $z_0'(s)$ satisfies $\bar{\rho}(z_0'(s)) = s$ for a monotonic reference density profile $\bar{\rho}(z)$. So defined, APE is the total energy required to restore isopycnals to the upstream reference state (*Holliday and McIntyre*, 1981), and is consistent with *Moum et al.* (2007b) and *Shroyer et al.* (2010a) when integrated over the entire domain used to calculate the reference state (*Winters and Barkan*, 2013). *Kang and Fringer* (2010)

discussed three definitions of APE in the context of NLIWs and concluded that (2) is the preferred one, since use of (2) introduces the smallest errors when computing the energy conservation laws.

The kinetic energy density $E_k(z)$ is defined as $E_k = u_w^2 + v_w^2 + w_w^2$. Since the vertical velocity w_w is usually an order of magnitude smaller than the horizontal velocities, and we do not directly measure it, the horizontal kinetic energy density E_{hk} is used to approximate E_k. E_{hk} is calculated as $E_{hk} = \frac{1}{2}\rho_0(\bar{\mathbf{U}}^2 + \mathbf{U}_w^2 + 2 * \bar{\mathbf{U}} \times \mathbf{U}_w)$ following *Lamb* (2010), where $\mathbf{U}_w$ and $\bar{\mathbf{U}}$ are the horizontal wave velocity and background velocity in wave coordinates. With this formulation, the presence of a sheared background current may introduce important consequences for the evolution of the mechanical energy in the system (*Lamb*, 2010).

Integrating E_a over depth and the horizontal extent for each individual wave, wave available potential energy E_A (units: J m^{-1}) is calculated as $E_\mathrm{A} = \int\int cE_a(z)dzdt$. A constant wave propagation speed of c_DJL is assumed here, which introduces $\approx 10\%$ error into the wave energy calculation. Similarly, wave kinetic energy E_K and total energy E_w are calculated for each wave in the dataset.

Sampling errors

The spatial and temporal resolution of the temperature and velocity sampling in 2010, 2011 and 2012 are not ideal for nonlinear internal wave detection. The vertically discrete CTD measurements and the 5-min sampling of ADCP in 2010-2012 impact the calculation of wave properties. In 2013, we substantially improved the vertical resolution of the temperature measurements (2 m) and the sampling frequency of both temperature and velocity (3 sec and 1 min, respectively). Temperature records in 2013 are used to estimate the impacts of vertically discrete measurements and gaps

over the water column on the calculation of η_w and E_A in 2010-2012. Velocity records in 2013, sampled every 1 min, are subsampled each 5 min to examine the effects of the temporal resolution of velocity data in 2010-2012 on U_w and E_{HK}. These effects are discussed below.

Temperature data in 2010-2012 have variable vertical spacing and gaps (Figure 2.2), which generally fall into three categories: 1) discrete temperature measurements over the water column at a vertical spacing of $dz = 6$ m, which represents most of the periods when sensors were functioning (e.g., June-July, Figure 2.2, cfi); 2) a gap in temperature measurements between a depth of 15 m and 60 m, which represents a significant portion of the data in Year 2012 after a sensor stopped functioning (e.g., September, Figure 2.2i); 3) a gap extending to the surface (e.g., late September 2010 - October 2010, Figure 2.2c). The effects of 6-m-spaced T measurements (Category 1) on the estimation of η_w and E_A are small (Figure 2.4b, 2.5). When gaps occur over the middle water column (Category 2), η_w is underestimated by an average of 24% and the E_A estimation is considerably scattered (Figure 2.4c, 2.5). When gaps are close to the surface (Category 3), the NLIW detection is unreliable due to their surface-intensified structures (not shown) and these records are removed in the analysis. Gray regions in Figure 2.2 indicate periods when coverage was adequate for reliable wave detection (Category 1, 2).

The 5-min velocity data in 2010-2012 are marginal for waves with typical duration of 10 - 20 minutes, therefore affecting the wave velocity and kinetic energy. An example of a wave train consisting of three waves observed on May 6, 2013 (Figure 2.6) suggests that the 5-min sub-sampling captures the waves, but tends to under-estimate the wave velocity depending on the sampling time. The maximum wave velocity $U_{\max}$ is underestimated by an average of 14%, and the wave horizontal kinetic energy E_{HK} estimation is scattered with a standard deviation of 32% (Figure 2.7). These errors

propagate into the energy flux and transport calculations, which are discussed later in Section 2.3.

2.3 Results

2.3.1 Oceanographic context

Washington's continental shelf has a strong seasonal wind-driven current. In spring/summer, winds are predominantly northerly (Figure 2.2a) and drive a southward shelf current (Figure 2.2, panels d, g, j, m; Figure 2.8d, black lines). In fall/winter, winds are predominantly southerly, resulting in a northward shelf current and effectively reversing the cross-shelf circulation pattern (Figure 2.2, dgjm; Figure 2.8d, grey lines). As a consequence of this and presumably increased wind mixing as fall storms set in, there is a clear distinction in the stratification between upwelling and downwelling seasons (Figure 2.8, panels a-c). In spring and summer, stratification is concentrated near the surface, with weaker stratification and deeper thermocline seen in winter. Event-scale (3 - 7 day) wind reversals (southerly winds) are commonly observed (Figure 2.2a, filled areas), which are typically weaker in spring/summer and stronger in fall, primarily caused by storms. During storms, currents often reverse and mixed layer depth increases.

2.3.2 Wave properties

Time series of wave amplitude η_w in all four years (Figure 2.2, panels b, e, h, k) suggest that waves are present much of the time. A weak seasonal pattern is suggested in that η_w remains generally smaller in spring and early summer (with most waves showing $\eta_w < 30$m), increasing near the end of August and September (with more occurrence of $\eta_w > 30$m). In the record of 2012, the only year when the mooring re-

mained in the water until December, no NLIWs are detected after October 15 (Figure 2.2h), likely due to the greatly reduced stratification. Storms also appear to impact the presence of waves (e.g., May 15, June 1 and June 29 in 2013), when the number of detectable NLIWs significantly decreased. However, these factors do not explain why there are more and stronger waves in some periods (e.g., September 14-19, 2010; June 16-24, 2011), with fewer and weaker waves in some other periods (e.g., July 26-30, 2011; June 16-22, 2012). Instead, NLIW occurrence is correlated with the internal tide energy flux, as we will demonstrate in Section 2.3.3.

Detected wave amplitude η_w has most common values of 10 - 20 m (Figure 2.9a), with an average of 15 m and a maximum of 52 m (Figure 2.3, Case 4). The percentage of waves with amplitude greater than 40 m (30 m) is 0.4% (3.7%), out of a total of 1533 waves. The DJL phase speed c_{DJL} mostly falls between 0.4 - 0.6 m s^{-1} (Figure 2.9b), typical for internal waves on shelves. Wave width at half amplitude $\lambda_{1/2}$, defined as the distance over which the amplitude decreased by half, assuming $c = c_{\mathrm{DJL}}$, is mostly between 100 and 300 m, with a mean of 260 m (Figure 2.9c). A small percentage of waves have $\lambda_{1/2}$ extending to 500 m or even 1000 m (Figure 2.9c), which correspond to the long-lived internal bores.

Wave energy E_w displays a considerable range from 10^4 to 10^8 J m^{-1}, with a typical magnitude of 1 MJ m^{-1} (Figure 2.9d). The ratio between E_{A} and E_{K} falls close to the line of 1:1, which is expected for stable waves, but displays an order of magnitude scatter (Figure 2.9, e-f). Part of the reason for this scatter is due to our limited sampling as discussed earlier. Another possible source of error is associated with the estimation of the reference state, for both E_{A} and E_{K} calculation, particularly when wave signals are weak compared to background signals. With these errors in consideration, the fact that E_{A} is higher on average than E_{K} by fraction of $\sim 20\%$ agrees with studies by *Lamb and Nguyen* (2009),*Moum et al.* (2007b), *Shroyer et al.*

(2010a) and *Lien et al.* (2013), indicating the potential of shoaling waves or the effect of spatial variations in the background current (*Lamb*, 2003, 2010).

Wave propagation direction θ_w is primarily towards the northeast (Figure 2.1a, red dots), with a most common value of 50^o T. Most scatter in θ_w is due to weaker waves, while the most energetic waves propagate towards the northeast or north-northeast almost exclusively. The similarity of θ_w to the direction of internal tide energy flux (Figure 2.1a, red arrow), suggests that the two may have the same energy source (*Alford et al.*, 2012). NLIW are directed slightly more toward the east than the internal tide due to the depth dependence of the wave speed, which could be explained by bathymetric refraction and the smaller wave speed of the internal tide compared to NLIWs. That is, the phase speed of internal waves decreases as water depth decreases, such that their wave crests continuously adjust to follow the isobaths (Figure 2.1b), making the nonlinear internal waves propagate more towards the east than the internal tide.

All 1533 detected waves are all mode-1 waves of depression, but have very different forms, which we loosely group into three categories based on the wave width $\lambda_{1/2}$. Waves are categorized as internal solitary waves (ISW, $\lambda_{1/2} < 500$ m), solitary wave trains (including more than one ISW) or internal bores ($\lambda_{1/2} > 500$ m). Examples of a single internal solitary wave, a solitary wave train, and an internal bore are given by Case 1, Case 2 & 4, and Case 3 in Figure 2.3, respectively. Internal bores account for 8.5% of the observed NLIWs, with the rest being ISWs in a train ($\sim 74\%$) or alone ($\sim 18\%$).

The occurrence of each wave type is not yet predictable (Figure 2.2), although more bores tend to be observed in September and October while solitary waves are more common in spring (e.g., Figure 2.2, Year 2010, 2012). The complexity of wave

taxonomy is not surprising in a topographically complicated coastal region like the WA coast, and is presumably related to the complex generation/evolution process and the temporal and/or spatial variation in the background shear and stratification.

2.3.3 Relationship with the internal tide

As discussed earlier, NLIWs are primarily generated by (i) lee waves, or (ii) nonlinear transformation of the baroclinic tide as it propagates onshore. The hypothesis in this study is that NLIWs off the WA coast are primarily generated by mechanism ii), which is supported by the phase relationship between NLIWs and the internal/barotropic tide, as well as correlation between their energy fluxes.

Strong mode-1, semi-diurnal internal tides exist in the record (e.g., Figure 2.10b), with typical downward phase propagation, indicating upward energy propagation. Mode-1 internal tide energy flux F_{IT}, calculated following *Alford* (2003), *Nash et al.* (2005) and *Alford and Zhao* (2007), is toward the north-northeast in all four years, with a mean of about 80 W m^{-1} (Figure 2.1a). Because internal tide fluxes from a regional numerical model are substantially smaller, *Alford et al.* (2012) concluded that the internal tides have a remote source, possibly the Mendocino escarpment. Semidiurnal barotropic tidal currents in this region are about 0.2 m s^{-1}, with ellipses oriented along-shelf (*Alford et al.*, 2012).

NLIWs generally arrive semi-diurnally with the internal tide, usually at isotherm depressions (e.g., Figure 2.10, a-c). The phase relationship is examined by the arrival time of NLIWs relative to the zero-crossing of the tidal phase based on the internal tide velocity ($\mathrm{U_{bc}}$), displacement (η_{bc}) and barotropic tide velocity ($\mathrm{U_{bt}}$). Most NLIWs in this period arrive together with the internal tide at a phase lag between -0.4π and 0.4π for $\mathrm{U_{bc}}$ and between 0.4π and 1.4π for η_{bc} (Figure 2.10, e-f). Note

that there is also a peak in the wave arrival time for the the barotropic tide (Figure 2.10d), because the internal tide and the barotropic tide are likely to be phase-locked during this time. In other periods, the waves arrive fairly irregularly and without clear tidal modulation (not shown).

If NLIWs arise from the internal tide, then their energy fluxes should be correlated (*Nash et al.*, 2012). Following *Moum et al.* (2007b), energy flux f_E (units: W m^{-1}) for each wave is calculated as:

$$f_E = c \langle E_z \rangle \tag{2.3}$$

in which $\langle E_z \rangle$ is the depth-integrated total energy density averaged over a wave length, and c is approximated by c_{DJL}. Because the waves are episodic, f_E is averaged over every 48-h window as

$$\langle f_E \rangle_{48h} = \tau_{w_i} f_{E_i} / 48h \tag{2.4}$$

in which τ_{w_i}, f_{E_i} are the duration and energy flux of the i-th NLIW, respectively. The average value of $\langle f_E \rangle$ (used as the short form of $\langle f_E \rangle_{48h}$ hereafter) is 144, 57 and 61 W m^{-1} in 2010, 2011 and 2012, respectively (2013 data are removed in this analysis due to their short velocity records). The magnitudes of $\langle f_E \rangle$ and F_{IT} are similar, and generally weakly correlated (Figure 2.11, a-c). On the other hand, the local barotropic forcing F_{BT} (Figure 2.11d), computed by $\langle N_{\mathrm{B}}^2 u_{\mathrm{BT}}^2 \rangle$ (*Baines*, 1974), where N_B^2 is the stratification within 40 m of the bottom, u_{BT} is the barotropic tidal currents in the cross-shelf direction, is visually unrelated with $\langle f_E \rangle$. Note this measure of barotropic forcing is an approximation to the forcing at shelf break, and has a nonexistent, or at best irregular, spring/neap cycle, typical for coastal regions (*Nash et al.*, 2012).

Calculated correlation coefficients R between $\langle f_E \rangle$ and F_{IT} are 0.59, 0.3 and 0.32 in 2010, 2011 and 2012, respectively, all of which are significant at a level of 95% based on t-test statistics. By contrast, correlation coefficients R_0 between $\langle f_E \rangle$ and F_{BT},

with values of -0.11, 0.1 and 0.01 in the three years, are not statistically significant. Note that $\langle f_E \rangle$ and F_{IT} are not entirely independent since the NLIW signals, in particular internal bores, project onto the semi-diurnal internal tide motions, as discussed in *Nash et al.* (2012). The correlation between the flux magnitude, similar direction of NLIWs and the internal tide, and the lack of correlation with the barotropic tide suggest that NLIWs are formed when remote internal tide steepen as they propagate onshore, instead of by direct local conversion from the barotropic forcing. It is noted that the correlation between $\langle f_E \rangle$ and F_{IT} are significant but not high, suggesting the importance of other factors such as bathymetry, background currents and shear.

2.3.4 Cross-shore transport

Nonlinear internal waves provide a mechanism for the transport of water mass over the continental shelf, making them a potentially important avenue for lateral movement of fluid, nutrients, larvae, and other biota as discussed earlier. *Huthnance* (1995) suggested that NLIWs may contribute significantly to cross-shore exchange in some locations, with a typical depth-integrated transport $\bar{U}_T \sim 1$ m^2 s^{-1}. This idea has been investigated using numerical models (*Lamb*, 1997) and observational tools (*Inall et al.*, 2001; *Shroyer et al.*, 2010b). *Shroyer et al.* (2010b) found an average NLIW transport of 0.3 m^2 s^{-1} over New Jersey's shelf, similar to the observations by *Inall et al.* (2001) on the Malin Shelf. Following *Lamb* (1997), *Huthnance* (1995) and *Shroyer et al.* (2010b), vertically-integrated transport due to NLIWs is calculated as

$$\bar{U}_T = \int \Delta(z)/\tau(z) dz \tag{2.5}$$

where $\tau(z)$, approximated by the wave duration time, is the amount of time a parcel of water at a given equilibrium depth is advected by the wave; $\Delta(z)$ is the particle transport distance due to Stokes drift, defined as $\Delta(x,z) = \int_{x'_{\mathrm{start}}}^{x'_{\mathrm{end}}} \frac{U_w(x,z)}{c - U_w(x,z)} dx'$ follow-

ing *Lamb* (1997) and *Shroyer et al.* (2010b) in wave coordinates. U_w was calculated by subtracting the background velocity interpolated along isopycnals (assuming streamlines follow isopycnals) and evaluated along constant density surfaces to find Δ as a function of undisturbed depth (Figure 2.12d). Note that this expression does not to take into account the vertical motion of particles which is an order of magnitude smaller than the horizontal velocity. The calculation requires $U_w < c$ (as $c \to U_w$, $\Delta \to \infty$), which is valid for about 99% of the waves detected in our study. Integration of $\Delta(z)$ over the surface to the first zero-crossing point gives an estimate of U_T and $\bar{U}_T$ is calculated as the average of U_T for each wave. The daily averaged onshore transport is then calculated as $\left\langle \bar{U}_T \right\rangle = \sum_{i=1}^{n} \tau_{w_i} \bar{U}_{T_i}/24h$, in which n is the number of waves within the day, τ_{w_i} is the duration of the i-th wave. $\left\langle \bar{U}_T \right\rangle$ has a mean (median) of 0.48 (0.36), 0.16 (0.08) and 0.49 (0.28) $\mathrm{m^2\ s^{-1}}$ in Year 2010, 2011 and 2012, respectively. Here we assume waves propagate at the DJL speed, i.e., $c \approx c_{\mathrm{DJL}}$, which includes the 10% uncertainty in c into the calculation of $\Delta(z)$ (Figure 2.13, gray). If c is close to U_w then the 10% uncertainly would translate into much larger uncertainties in the transport distance (*Lamb*, 1997). Additionally, the strongest transports would be expected to be up shallow, above our direct velocity measurements.

As a comparison, northerly wind off the WA coast generates an offshore wind-driven Ekman transport in the surface layer, leading to an onshore transport below the surface and near-shore coastal upwelling due to mass conservation. The Ekman transport is calculated as $U_E = \tau_s/(\rho_0 f)$ (*Ekman*, 1905), where τ_s is the along-shelf component of the wind stress (Figure 2.2a), $\rho_0 = 1025\ \mathrm{kg\ m^{-3}}$ is a nominal background density, and f is the Coriolis parameter. Averaged over the upwelling periods, U_E has a mean (median) of 0.21(0.15), 0.20 (0.15), and 0.19 (0.12) $\mathrm{m^2\ s^{-1}}$ during *ChaBa* deployments in Year 2010, 2011 and 2012, respectively. Here U_E is about one third smaller than the value off the Oregon coast (*Lentz*, 1992), as a result of the weak upwelling-favorable winds off the WA coast comparing to the rest of US West coast

(*Hickey and Banas*, 2008). Comparing the daily average NLIW transport to onshore Ekman transport balancing the surface-layer offshore transport in three years (Figure 2.13), the time-integrated effect of the strong but episodic NLIW transport is significant compared to the weak but sustained Ekman transport, making the waves a potentially important contributor to the local mass balance.

2.4 Discussion

Nonlinear internal waves observed in this study have a large variety of shapes and properties, including internal solitary waves, solitary wave trains and internal bores. The formation, evolution and breaking of NLIWs have been analyzed in previous numerical and laboratory studies, presumably depending on bathymetry features, tidal forcing, background stratification/currents and the earth's rotation (e.g., *Maxworthy* (1980); *Helfrich and Melville* (1986); *Legg and Adcroft* (2003); *Venayagamoorthy and Fringer* (2012)). The change in the relationship between these factors should lead to different evolution and dissipation as the wave propagates, thereby giving different shapes at the observational site (*Ostrovsky*, 1978; *Gerkema*, 1995; *Stepanyants*, 2006). Additionally, variations in the oblique angle of incidence of the internal tides on the irregularly-shaped continental shelf would be expected to modulate the formation and steepening of the waves. A full understanding of the generation and evolution of the NLIWs in the complicated coastal system with modulations/re-directions by local low-frequency flows and bathymetry is beyond the scope of this study, and presumably requires more observational studies and three-dimensional, non-hydrostatic numerical simulations.

As shown, the nonlinear internal waves appear to transport water mass. The nitrate transport by nonlinear internal depression waves might be expected to be small because nitrate is minimum near the surface. However, the onshore mass transport

due to NLIWs reaches a depth of $\sim$ 20 m (Figure 2.12, lower right), where the nitrate concentration is usually much higher than the surface layer. Assuming an offshore nitrate concentration of 1 μM (*Banas et al.*, 2009) is transported by the waves onto a nitrate-free shelf, the onshore flux for a typical wave crest with an long-shelf length of 50 km is about 1.2 kg nitrate s^{-1} (assuming $U_T = 0.38$ m^2 s^{-1}, the time-average mass flux from previous section). Integrating the nitrate flux over the upwelling season (90 days), the total nitrate input due to NLIWs is up to 0.9×10^7 kg, about an order of magnitude smaller than the inputs from other sources, such as the Strait of Juan de Fuca, coastal water, canyon enhancement and the Columbia river (*Hickey and Banas* (2008)). It is noted that this simple calculation is based on a number of assumptions and approximations, including constant nitrate concentrations inside wave crests and a linear relationship between U_{w} and $\Delta(z)$ (which is a convex function according to *Lamb* (1997)). This near-surface transport would potentially be more significant to buoyant larvae or seeds of marine plants that need to be transported back onshore to settle. More detailed biogeochemical observations in the region are needed and are the focus of on-going work.

2.5 Conclusions

We document observed characteristics of nonlinear internal waves (NLIWs) on the Washington continental shelf, using four summers/falls of temperature, salinity and velocity records from a surface mooring. A large number ($>$ 1500) of NLIWs are detected and their taxonomy (internal solitary waves, solitary wave trains and internal bores) documented. Wave characteristics in the four years have similar features: onshore propagation directions towards the northeast; significant amplitudes relative to water depth (up to 51 m in 100 m water); and wave energy up to $\sim O(10^8$ J $m^{-1})$. Waves are generally weak in spring/early summer, strong in late summer/fall, and absent in winter, presumably due to variations in background stratification and cur-

rents that impact wave generation and propagation.

NLIWs appear to be generated by shoaling of remotely-incident internal tides (IT) instead of by local barotropic conversion, suggested by 1) semi-diurnal wave arrivals are often phase-locked with the internal tide; 2) the propagation direction of NLIWs and the IT energy flux direction are consistent, with NLIWs steered more onshore by the bathymetry; 3) NLIW and IT energy flux are correlated; and 4) NLIW energy flux and the local barotropic forcing are uncorrelated.

Estimated time-mean onshore transport due to NLIWs (0.38 m^2 s^{-1}) is significant compared to the Ekman transport, suggesting the waves may be an important mechanism for cross-shore mass transport during these periods. More detailed biogeochemical observations and modeling are required to estimate the effects of these waves on local nutrient supply and productivity.

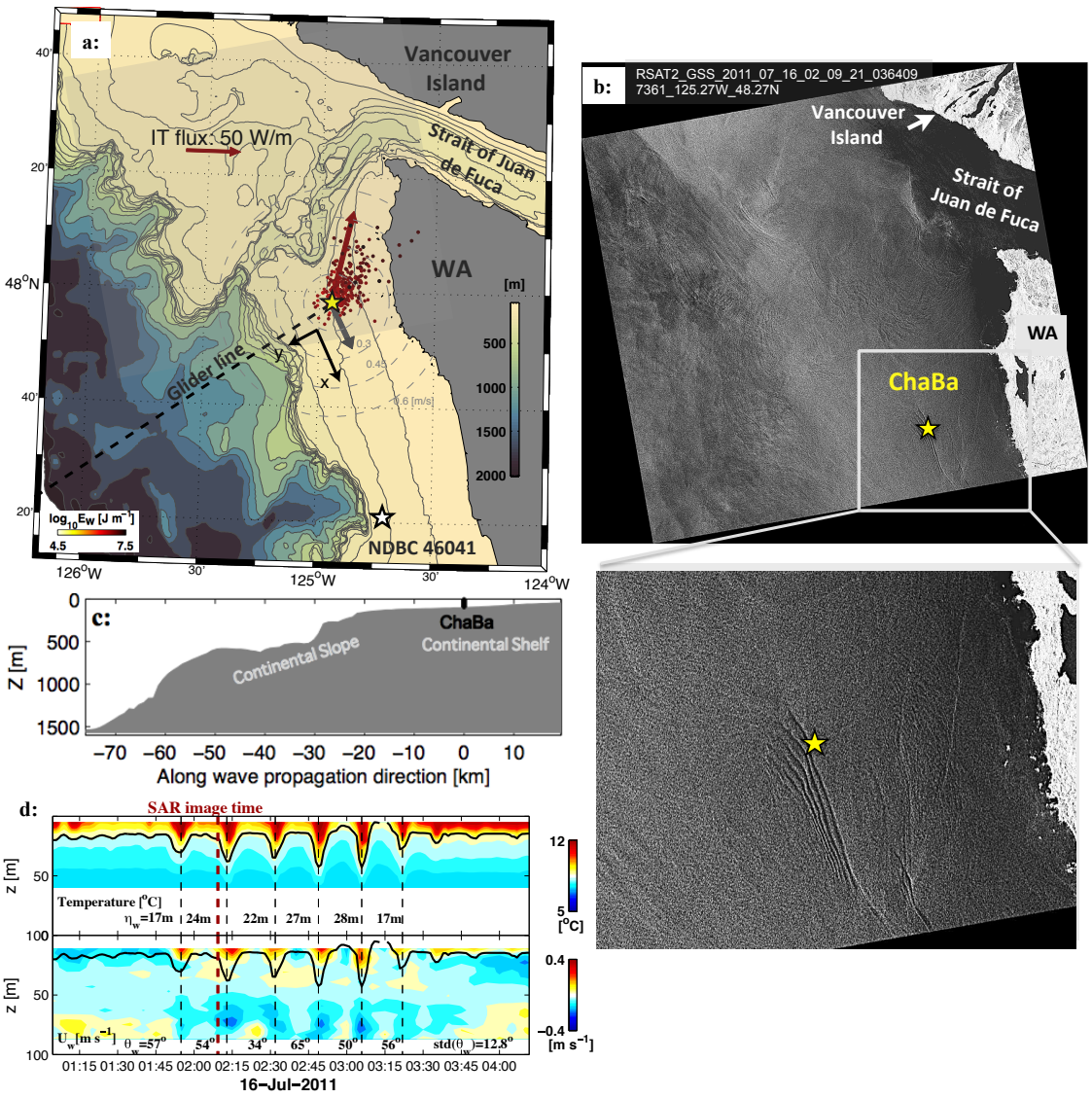

Figure 2.1: (a) Site map showing bathymetric features, along with *ChaBa* mooring (yellow star), NDBC buoy (white star), time-mean semidiurnal mode-1 internal tide energy flux F_{IT} (red arrow) and the Seaglider SG187 line (black dashed line) across the continental slope/shelf. Along-shore flow (gray arrow, positive x corresponds to positive values in Figure 2.2, panels a, d, g, j and m) and the NLIW velocity (red dots, colored by their log-scale energy) are shown in a polar plot. The along-shore and cross-shore coordinates are marked by black arrows; (b) a SAR image taken by Radarsat-2 on July 16, 2011, 02:09:21 UTC over the shaded area in (a) with a zoomed-in plot, capturing a wave train passing by *ChaBa* (yellow star); (c) cross-shelf bathymetry of the area following the glider line in a); (d) time series of temperature and velocity in wave coordinates from *ChaBa* for the wave train detected in (b). Calculated maximum isotherm displacements are plotted in black lines. Black vertical dashed lines indicate wave troughs. Values of wave amplitude η_w, propagation direction θ_w and the standard deviation of calculated θ_w are marked. The red dashed line indicates the time when the SAR image in (b) was taken.

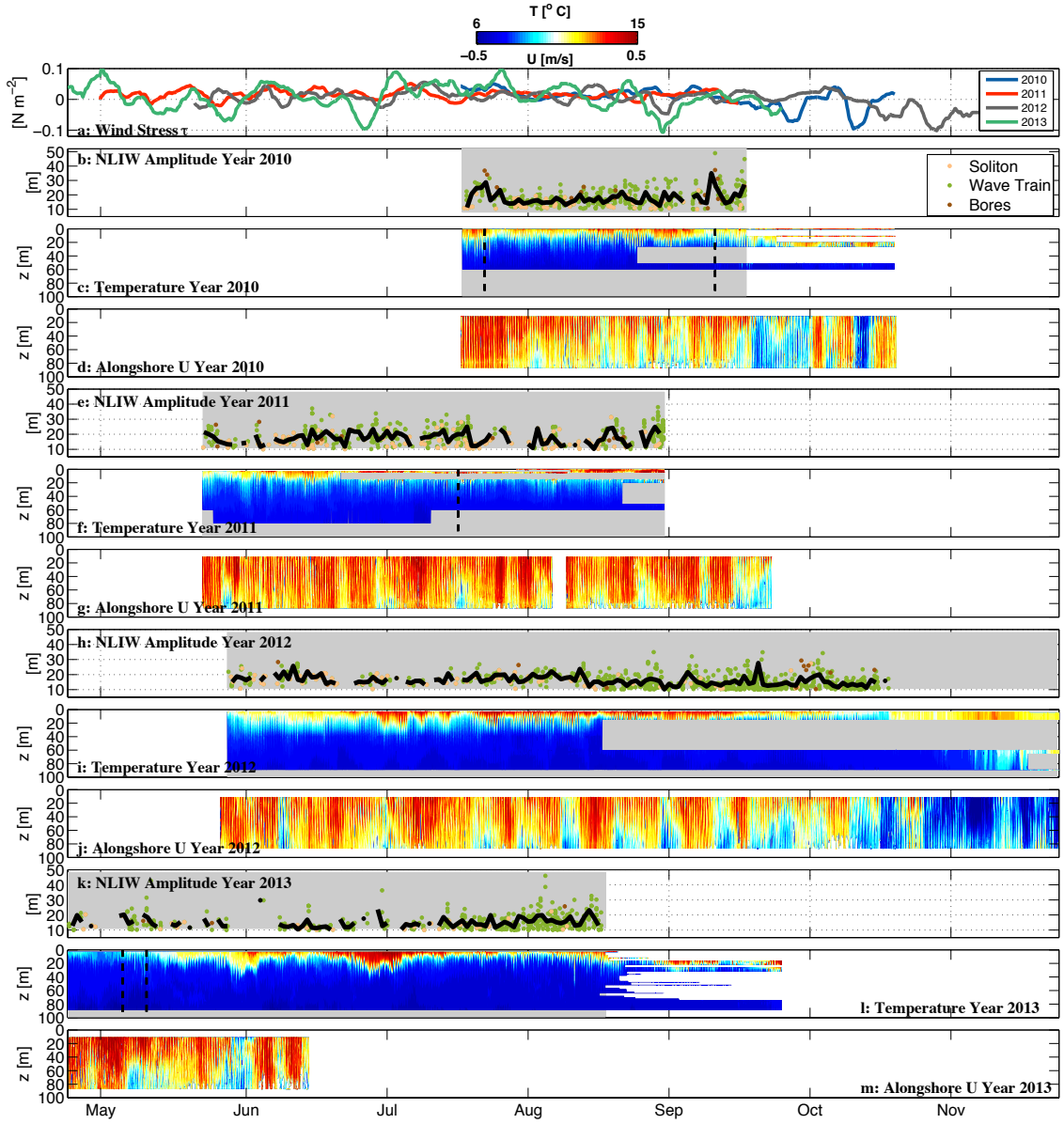

Figure 2.2: Data and nonlinear internal wave summary, showing wind stress for all four years (a); NLIW amplitude (b), colored by wave type (see text), and the running 1-day mean (black); temperature (c); and alongshore velocity (d) measured at *ChaBa* in 2010. Positive values in (a) and (d) correspond to positive x in Figure 2.1a. (e-g): as in (b-d) but for 2011. (h-j): as in (b-d) but for 2012. (k-m): as in (b-d) but for 2013.

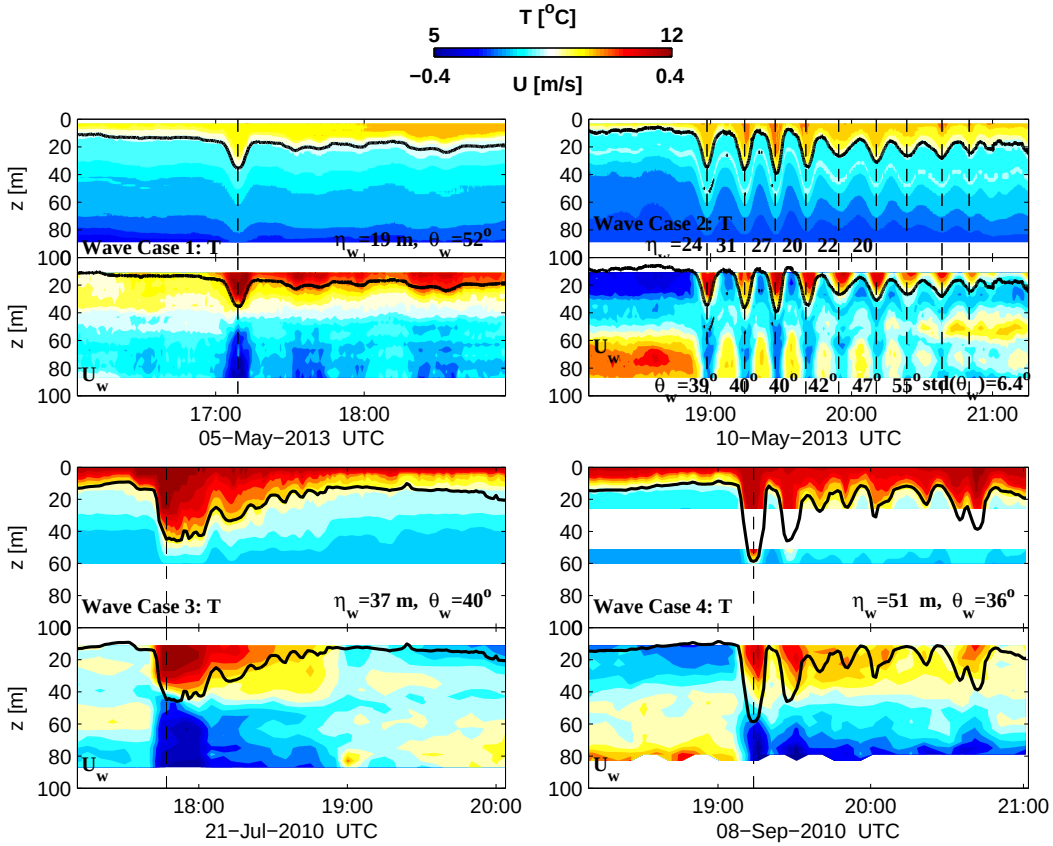

Figure 2.3: Four examples of NLIWs detected in the moored records, showing time series of temperature (T) and velocity along wave propagation directions (U_w) for a solitary internal wave (Case 1), a solitary wave train (Case 2), an internal bore (Case 3), and the largest wave in the record (Case 4). Vertical dashed lines indicate detected wave troughs. Maximum isotherm displacements are overplotted in black.

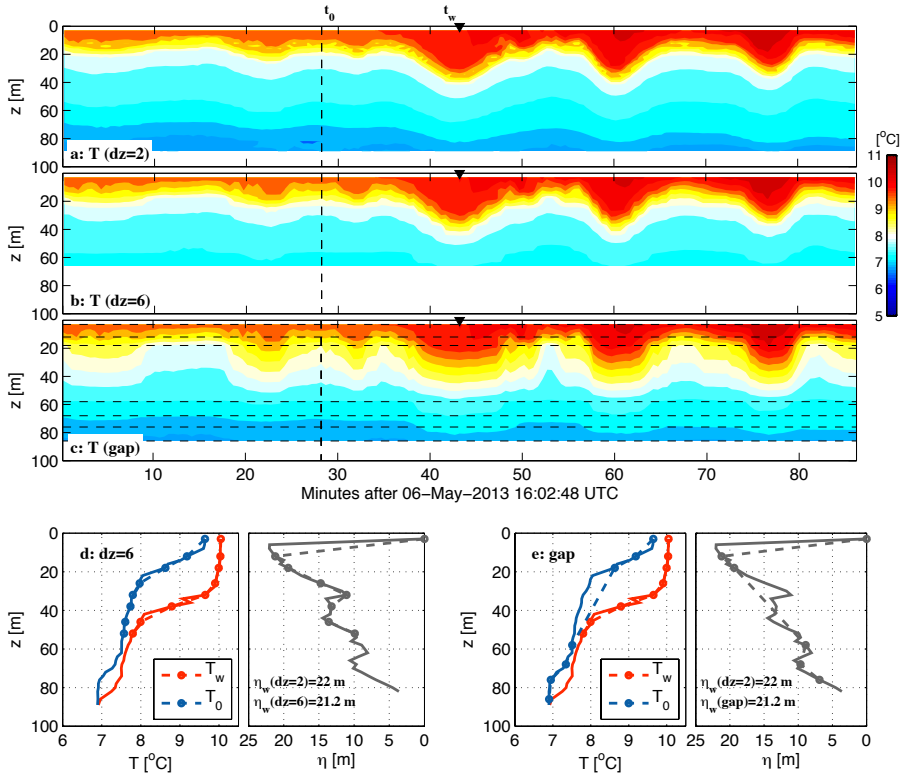

Figure 2.4: (top) Temperature time series for a wave detected in Year 2013, showing three cases: a) the original sampling with a vertical spacing of $dz = 2$ m; b) subsampled with $dz = 6$ m; and c) subsampled with a gap in the mid-water column. Vertical dashed lines in (c) are depths of measurements. (d) Temperature profiles within the wave (T_w, red) and in the reference state (T_0, blue), and the corresponding isotherm displacements ($\eta(z, t_w)$, gray) calculated in the subsampled case of $dz = 6$ (dashed) compared to the full-resolution data (solid). (e) as in (d) but for the subsampled case with a gap.

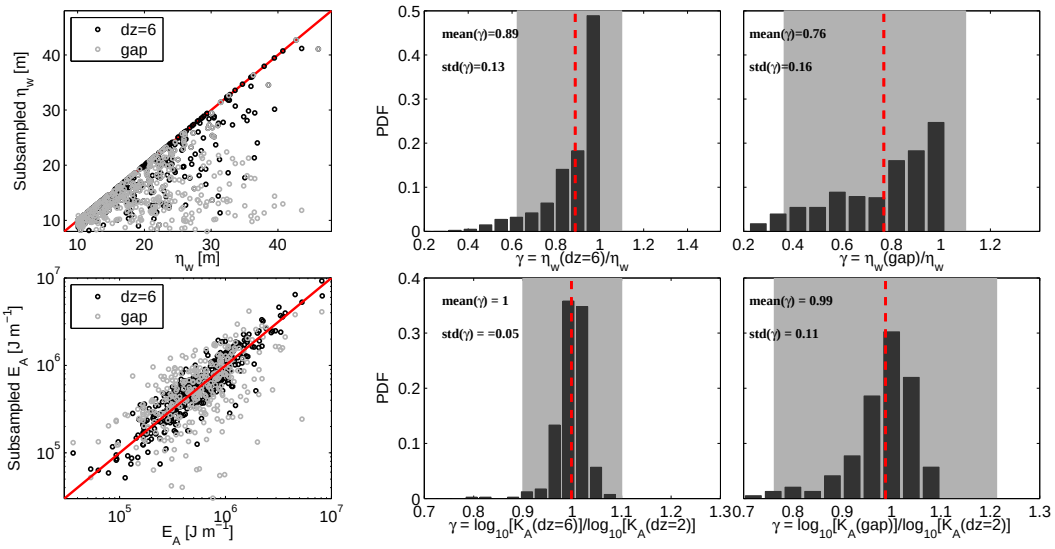

Figure 2.5: (upper panels) Examination of the sampling effects on η_w estimation, including (left) a scatter plot showing the subsample cases and the original data for η_w analysis and PDF plots showing the ratio between η_w calculated from two subsample cases: $dz = 6$ (middle) and a gap in the mid-water column (right). (lower panels) Same analysis but for E_A estimation. Red dashed lines indicate sample means. Gray indicates theoretical 95% confidence intervals.

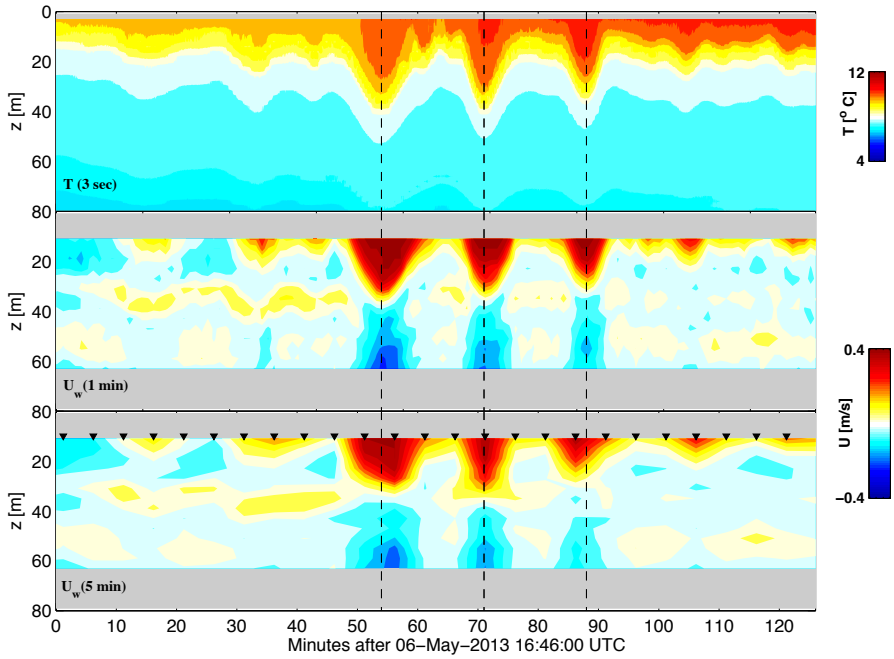

Figure 2.6: Temperature, 1-min velocity and subsampled 5-min velocity for a wave detected on May 6, 2013. Vertical dashed lines denote detected wave troughs. Black triangles denote the 5-min subsampling time.

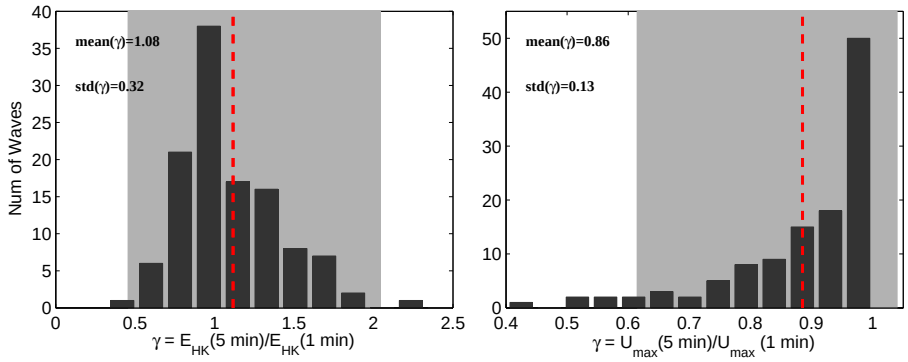

Figure 2.7: PDF plots of the ratio between 5-min subsample velocity data and the original velocity data, for calculated wave kinetic energy E_{HK} (left) and the maximum wave velocity $U_{\max}$ (right). Red dashed lines indicate sample means. Gray indicates theoretical 95% confidence intervals.

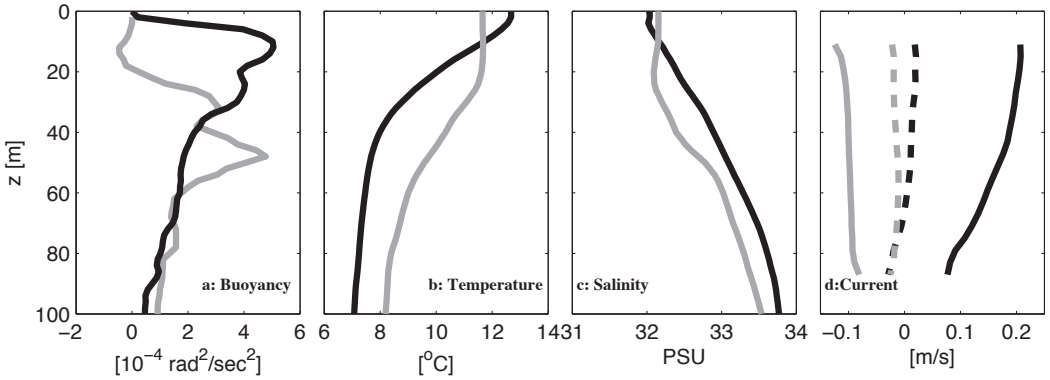

Figure 2.8: Profiles of background stratification N^2 (a), temperature (b) and salinity(c) from the glider. (d) Background along-shore (solid) and cross-shore (dashed) currents in spring/summer (black) and fall/winter (gray) from the mooring.

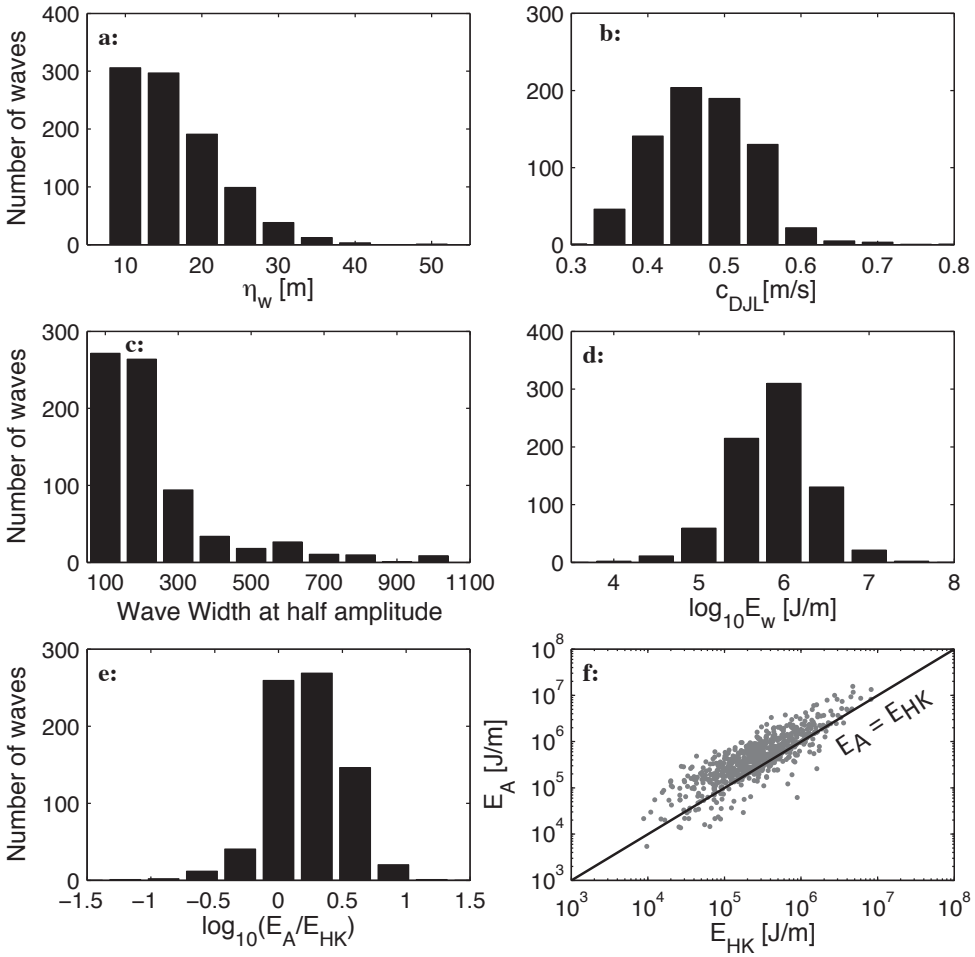

Figure 2.9: Histograms of basic features of NLIWs detected in 2010, 2011 and 2012, including (a) wave amplitude η_w, (b) DJL phase speed c_{DJL}, (c) wave width at half amplitude $\lambda_{1/2}$, (d) log-scale total energy $\log_{10}E_w$, (e) log-scale ratio of wave available potential energy E_{A} over horizontal kinetic energy E_{HK}, and (f) a scatter plot of E_{A} over E_{HK}, with 1:1 indicated by a black line.

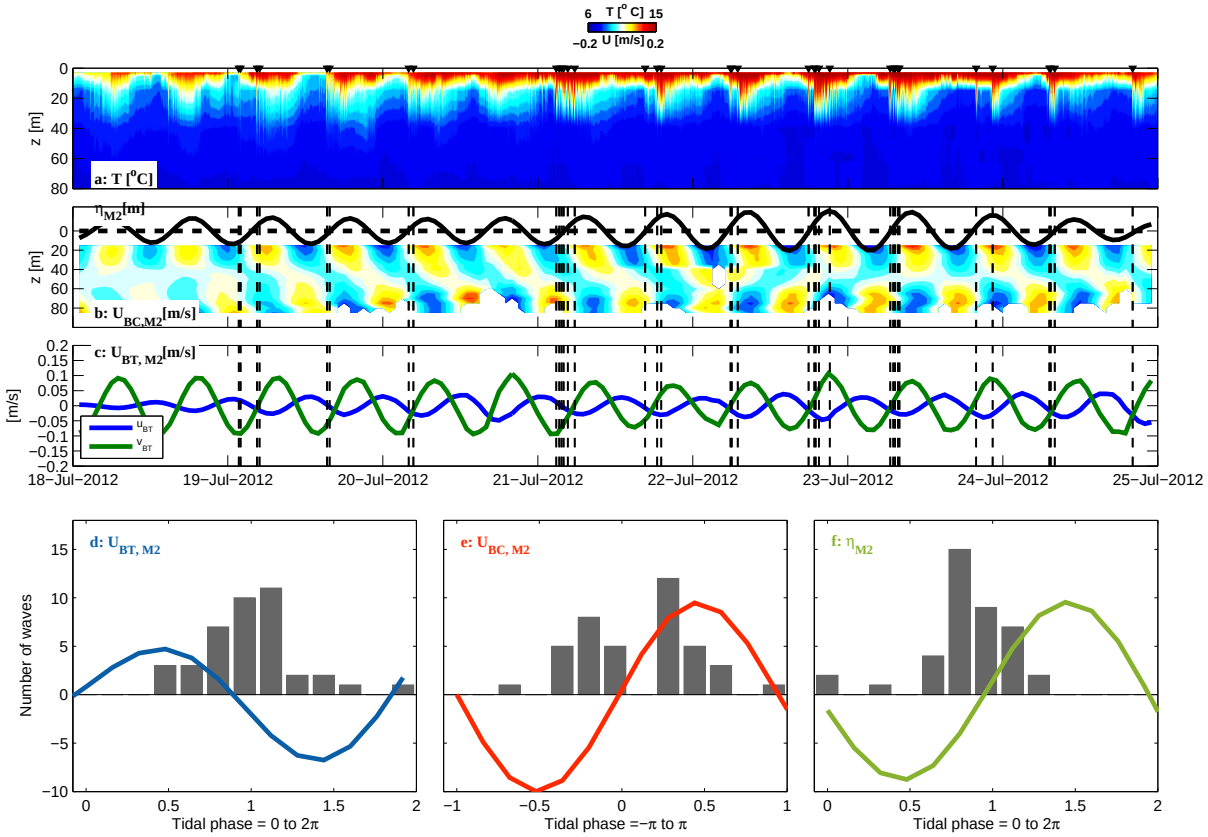

Figure 2.10: A 7-day period during July 18-25, 2012, showing temperature (a), semidiurnal baroclinic velocity in the wave propagation direction U_{bc} and isopycnal displacement η_{IT} at a depth of $z = 15$ b), and semidiurnal barotropic velocities U_{bt}, V_{bt}(c), with wave arrival times indicated by black triangles in (a) and vertical dashed lines in (b) and (c), respectively. Histograms of number of waves with arrival times relative to the tidal phase of U_{bt}, U_{bc} and η_{IT} are shown in (d) - (f), respectively.

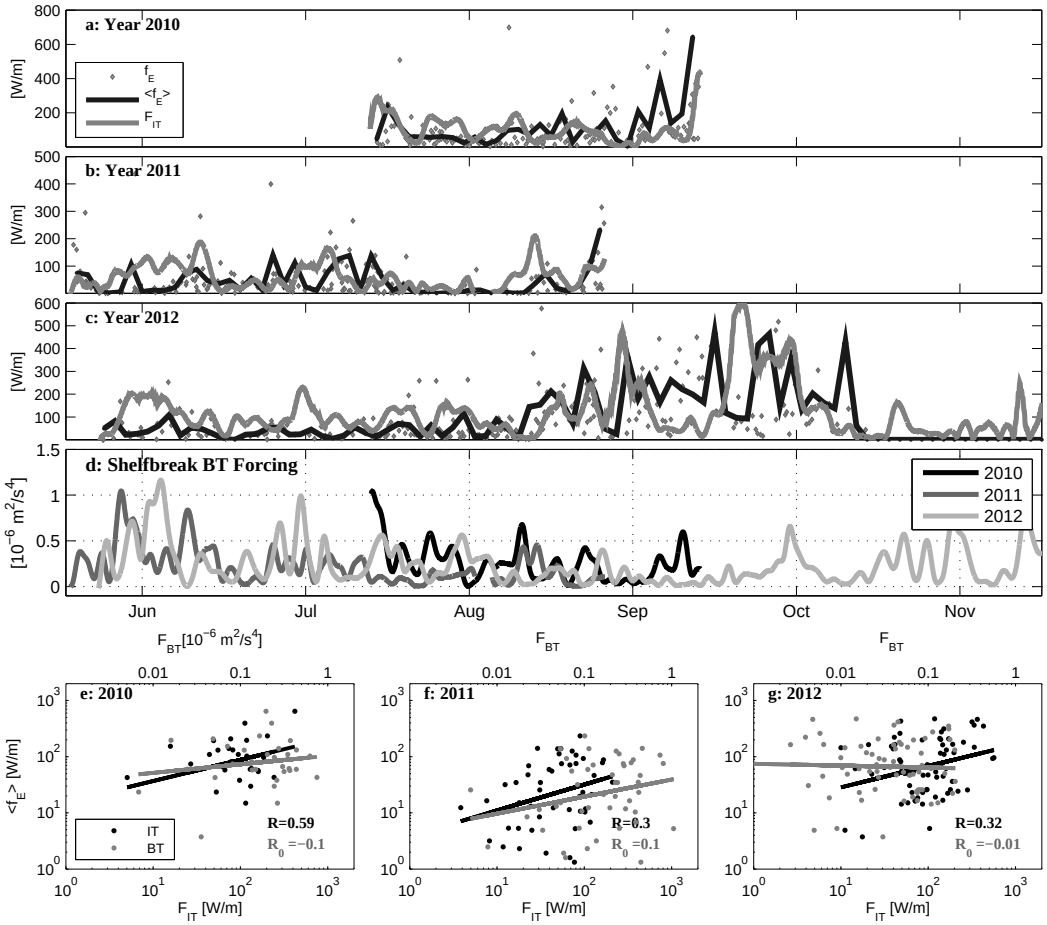

Figure 2.11: (a)-(c) Time series of 48-h averaged NLIW energy flux ($\langle f_E \rangle$, black lines), contribution to the energy flux from individual NLIW ($f_{\rm E}$, grey dots), and mode-1 IT energy flux ($F_{\rm IT}$, gray lines) in 2010, 2011 and 2012; (d) local barotropic forcing over the shelf break ($F_{\rm BT}$); (e)-(g) scatter plots of $\langle f_E \rangle$ over $F_{\rm IT}$ (black) and $F_{\rm BT}$ (grey), with corresponding values of correlation coefficients R and R_0 noted, for records in 2010, 2011 and 2012. Lines indicate the best fits in linear scale in each case.

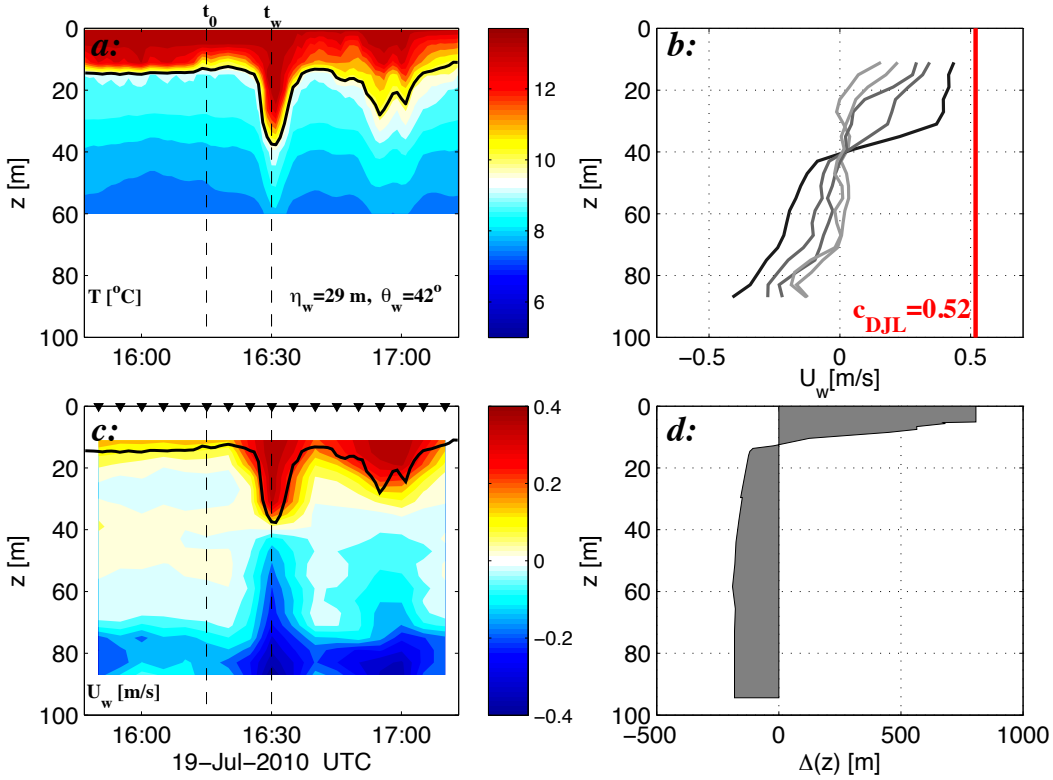

Figure 2.12: Temperature and velocity for a wave detected on July 19, 2010 (left). Maximum isotherm displacements are overplotted in black. Vertical dashed lines indicate the background state (t_0) and the wave trough (t_w). Black triangles indicate sampling times of velocity. Wave velocity profiles (colored by the isotherm displacements; black indicates the wave trough, i.e., maximum displacements) compared to the DJL phase speed c_{DJL} (upper right). The Stokes drift profile $\Delta(z)$ at the wave trough (lower right).

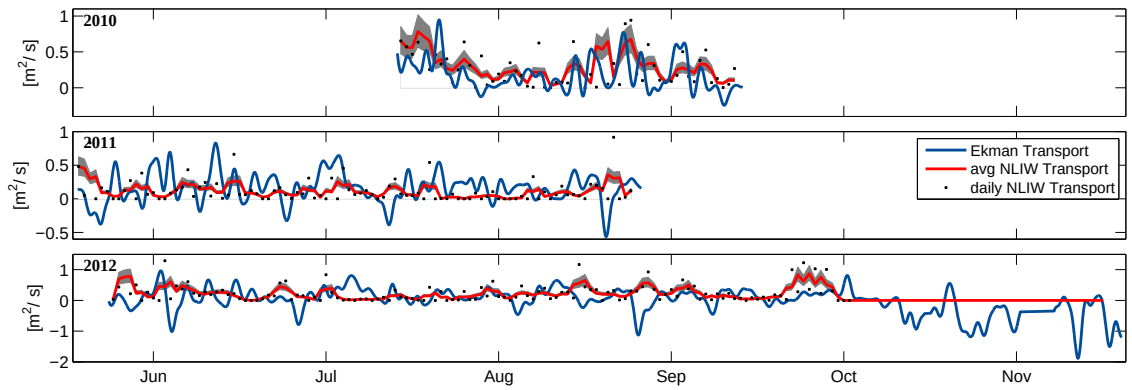

Figure 2.13: Three years (2010-2012) of the 1-day low-passed Ekman transport (blue lines) in the cross-shore direction (positive means offshore), daily averaged onshore transport due to the NLIWs (black dots) and its moving average (red lines) in the cross-shore direction (positive means onshore). Gray indicates error bars due to the 10% uncertainty in phase speed.

Chapter 3

BREAKING NONLINEAR INTERNAL WAVES ON THE WASHINGTON CONTINENTAL SHELF

3.1 Introduction

Nonlinear internal waves (NLIWs) are commonly observed on continental shelves around the globe. Observations of high turbulence levels within NLIWs have been reported (e.g. *Sandstrom and Oakey* (1995); *Stanton and Ostrovsky* (1998); *Duda and Farmer* (1999); *Moum et al.* (2003); *MacKinnon and Gregg* (2003)), making them an important mechanism for mixing in coastal regions (e.g. *Moum et al.* (2007a,b); *D'Asaro et al.* (2007)). NLIWs create conditions favorable for instabilities and can produce one half of mid-water-column dissipation on continental shelves (e.g., *MacKinnon and Gregg* (2003)). This indicates that energy of NLIWs is not simply deposited in the surf zone but that a considerable portion is lost as it propagates onshore over the shelf (*Moum et al.*, 2003, 2007a). Accordingly, patterns of nutrients and other materials fluxed across the shelf by these waves will depend on the strength and time/space dependence of the mixing. Mixing associated with internal waves has been tied to enhanced vertical nutrient fluxes, in some cases controlling local productivity, e.g., the New Zealand shelf (*Sharples et al.*, 2009), the Scotian shelf (*Sandstrom and Elliott*, 1984) and off the coast of Mauritania (*Schafstall et al.*, 2010). Breaking internal waves at Dongsha Atoll in the South China Sea have a possible role of the microbial food web on nutrient regeneration in a tropical reef ecosystem (*Wang et al.*, 2007).

Lamb (2014) described four primary instability mechanisms through which NLIWs can result in mixing: 1) shear instabilities triggered by NLIW-induced vertically

sheared currents, 2) convectively wave cores, 3) instabilities in the bottom boundary layer, and 4) wave break during sudden shoaling at abrupt topography. The former two mechanisms are dominant for mid-column mixing apart from rapid bathymetric changes, and are consistent with the observations in *Moum et al.* (2003) and *Shroyer et al.* (2010a), where they observed billow-like structures associated with NLIWs, and categorized them as Type I and Type II waves based on the two mechanisms (Figure 3.2), respectively. While pioneering, one shortcoming of the previous studies was their inclusion of a small number of waves. Hence, the generality of the results and their dependence on wave properties such as velocity, shear and wave amplitude displacement is unknown.

In this study, we take advantage of a 6-month moored time series on the Washington (WA) continental shelf (Figure 3.1 shows a SAR image with a wave train) in which we capture 657 waves at high vertical and temporal resolution. Data from the moored densely-spaced thermistor string accompanied by velocity measurements (details in next section) show waves with two types of instability mechanisms, similar to those identified by *Lamb* (2014) and *Shroyer et al.* (2010a): I. high dissipation confined to the sheared interface of waves (wave #1 in Figure 3.3), and II. elevated dissipation distributed throughout the wave core, in regions of high and low shear (wave #2 in Figure 3.3). The large number of waves allows us to form composites and to examine the relative importance of each mixing mechanism based on statistics. This study expands previous studies of *Moum et al.* (2003) and *Shroyer et al.* (2010a) by 1) documenting NLIW-induced instabilities and their temporal variation; 2) categorizing waves based on instability mechanisms (shear instability and convective instability/unstable cores); and 3) exploring general patterns of NLIW-induced mixing from composites based on a longer time series of dataset.

A major shortcoming of our dataset is the lack of direct microstructure measure-

ments. Instead, we employ the method of Thorpe scales, which measures the outer scale L_T of turbulence by resorting statically unstable profiles, whence the dissipation rate ϵ can be estimated (e.g., *Dillon* (1982)). The method has been demonstrated in multiple experiments (e.g., *MacKinnon and Gregg* (2005); *Alford et al.* (2006)) to give values of ϵ within a factor of two of direct measurements of turbulence (with the caveat that recent modeling work by *Mater et al.* (2013) gives rise to the possibility that epsilon from overturns is biased high as much as 2-6 in some regions; these effects are still being explored). However, the 2-m vertical spacing between sensors is relatively coarse for detection of overturning events, allowing us to examine a minimum dissipation rate of $\sim O(10^{-6}) - O(10^{-5})$ W m^{-1}, with a stratification $N^2 \sim O(10^{-6}) - O(10^{-3})$. Therefore, while the largest events generally dominate the mean value (*Levine and Boyd*, 2006; *Alford and Pinkel*, 2000b), smaller turbulence patches are not detected. We consider these effects in our analysis.

This chapter is organized as follows. The experimental setup, data and techniques are presented in Section 3.2. Background oceanographic background and basic characteristics of NLIWs are described in Section 3.3. Wave categorization based on instability mechanisms is documented in Section 3.4. Temporal variability in NLIW-induced instabilities and their relationships to the background parameters are reported in Section 3.5. Composites of wave-induced dissipation rates and the general structure in each category are discussed in Section 3.6, followed by a summary and conclusion in Section 3.7.

3.2 Experimental Details

3.2.1 Data

Data used in this study are from the *"ChaBa"* surface mooring, designed and maintained by University of Washington as part of the Northwest Association of Networked

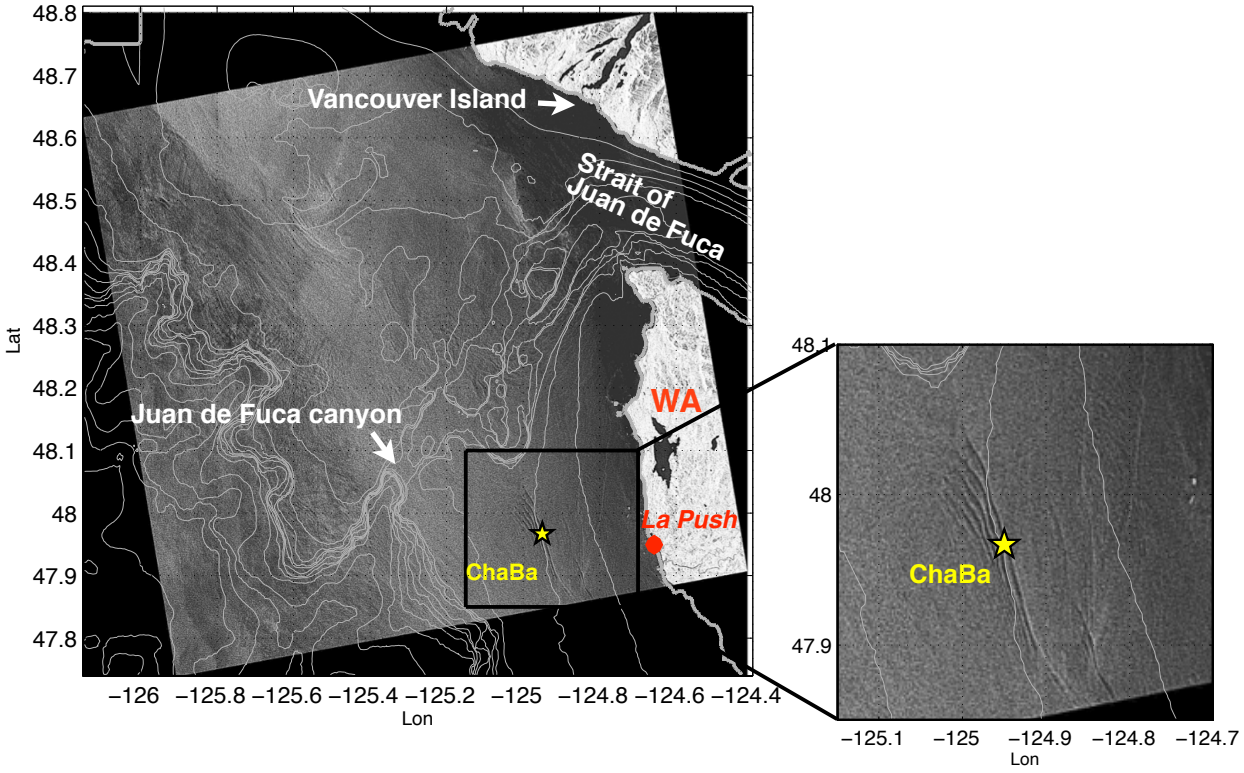

Figure 3.1: A SAR image captured by Radarsat-2 on July 16, 2011, 02:09:21 UTC with bathymetry super-imposed, The zoom-in plot shows a nonlinear internal wave train passing by the *ChaBa* mooring (yellow star)

Ocean Observing Systems (NANOOS). *ChaBa* (47^{o}58.0′N, 124^{o}57.0′ W) was deployed for five successive summers/falls from 2010-2014 in 100-m deep water $\sim$ 25 km off La Push, WA (Figure 3.1). Data used in this study are from the deployment of *ChaBa* during April 24 - September 23, 2013, mainly include temperature and salinity measurements from conductivity-temperature-depth (CTD) sensors mounted along an 81-m mooring wire, and velocity records from an acoustic Doppler current profiler (ADCP) mounted in a subsurface cage. Temperature was measured every 3 seconds by 40 Seabird Electronics (SBE) 56 T-loggers spaced over a 2-m interval between the surface and 80-m depth (Figure 3.3b). A downward-looking 300 kHz Workhorse ADCP at 3-m depth recorded near-full-depth velocity profiles every 1 minute from

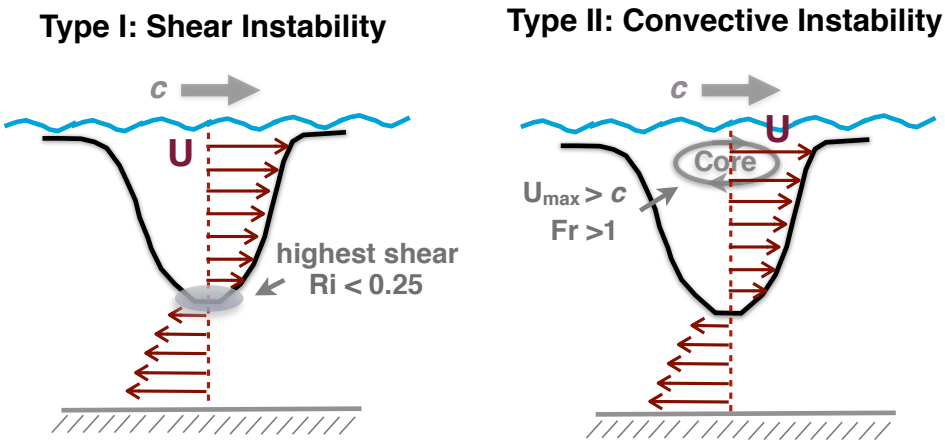

Figure 3.2: A cartoon showing two types of waves: shear-instability waves (Type I) and convective-instability waves (Type II).

Aril 24 to June 14 until the batteries died (Figure 3.3c). Wind measurements (Figure 3.3a) are from National Data Buoy Center (NDBC) Station DESW1 at Destruction Island, located at $47^o40.5'$ N, $124^o29.1'$ W, about 30 km away from *ChaBa* to the east.

3.2.2 Calculation of dissipation rate using Thorpe scale

We do not measure turbulence directly in this experiment, and surface wave pumping precludes calculation of dissipation rates using the Bachelor wavenumber method (*Batchelor*, 1959; *Dillon and Caldwell*, 1980; *Alford and Pinkel*, 2000a; *Moum and Nash*, 2009). We instead estimate dissipation rate using overturning (Thorpe) scales L_T computed from the vertically discrete thermistors following *Levine and Boyd* (2006). Dissipation rate ϵ is given by $\epsilon = 0.64 L_T^2 N^3$ (*Dillon*, 1982), where N is the sorted profiles of stratification. An example of NLIW on Aug 13, 2013 detects temperature overturns up to 15 m (Figure 3.4). In this example, temperature profiles plunge through the wave's leading edge to maximum displacement (25 m), indicating the drop of pycnocline during the passage of this wave. Before the maximum dis-

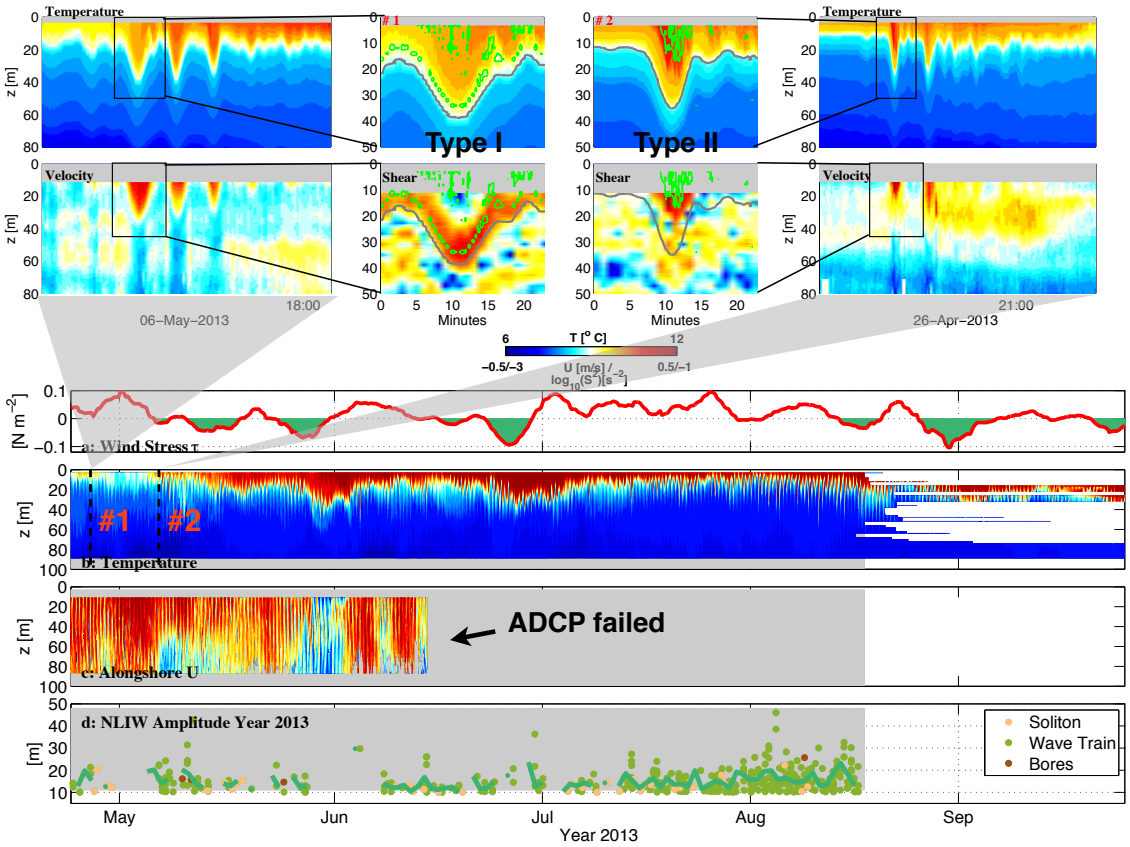

Figure 3.3: Time series of the mooring data and nonlinear internal wave examples, showing along-shore wind stress (a, southeastward as positive and green areas as reversals); temperature (b); alongshore velocity (c, southeastward as positive); and NLIW amplitude (d), colored by wave shape (see text), and their running 1-day mean. Black dashed lines in (b) indicate arrivals of two wave examples #1 and #2 (subplots) for Type I and Type II waves (see text), respectively. Waves in subplots are given by time series of temperature, velocity and 4-m vertical shear. Gray and green contours indicate the 9^{o}C isotherm and temperature inversions, respectively.

placement, turbulent overturns start at $\sim$ 5 m near the interface, corresponding to a dissipation rate of $O(10^{-5}) - O(10^{-4})$ W kg^{-1}. Immediately after the maximum displacement, overturns develop to 15 m and the interface then becomes actively turbulent throughout the trailing edge and the wake of this wave. Depth-integrated dissipation (Figure 3.4d) has a maximum value ($\sim$ 9 W m^{-2}) immediately following the maximum displacement, with secondary peaks right before the wave trough and in the turbulent wake.

Though 4 times finer than that of *Levine and Boyd* (2006), our sensor spacing of 2 m is relatively coarse given the strong coastal stratification at our site. The minimum detectable overturn of 2 m corresponds to a Thorpe displacements $L_T^{\min}$ of $\sim$ 1 m and a sensitivity of dissipation rate $\epsilon^{\min} \sim O(10^{-6}) - O(10^{-5})$ W kg^{-1}, depending on N. As an example of mixing events that are nearer to our detection threshold, a series of small overturns (2 m - 5 m) are recorded along the interface of a wave on August 9, 2013 (Figure 3.5) and the corresponding dissipation rates are estimated to be $\epsilon^{\min} \sim O(10^{-6})$ W kg^{-1} near the interface.

Persistent lateral thermohaline intrusions exist at our site, usually below the thermocline (e.g., Figure 3.7 and Figure 3.8). Since they are statically stable, these would introduce large overestimates in the Thorpe Scale calculation if not properly screened. Therefore, we focus on mixing within the thermocline above a certain isotherm depth, which is a value between $8^o - 9^o$C to exclude largest deep intrusions during the period. Also, intrusions generally have much longer duration than NLIWs ($\sim 10 - 15$ min). Thus they are easily distinguished by comparing the time scale of overturning events to that of the waves.

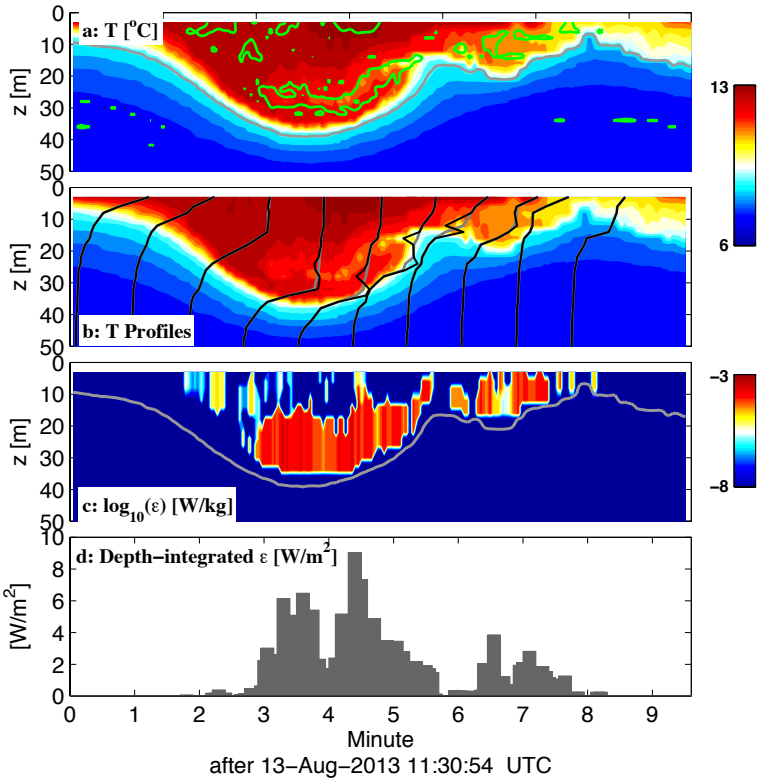

Figure 3.4: A wave example with large temperature overturns detected on August 13, 2013, showing (a) temperature time series (green and gray contour temperature inversions and the 9^{o}C isotherm, respectively); (b) temperature profiles (black) every 30 sec and their sorted profiles (grey dashed); (c) estimated dissipation rate based on Thorpe scales (grey contours the 9^{o}C isotherm); and (d) depth-integrated dissipation rate.

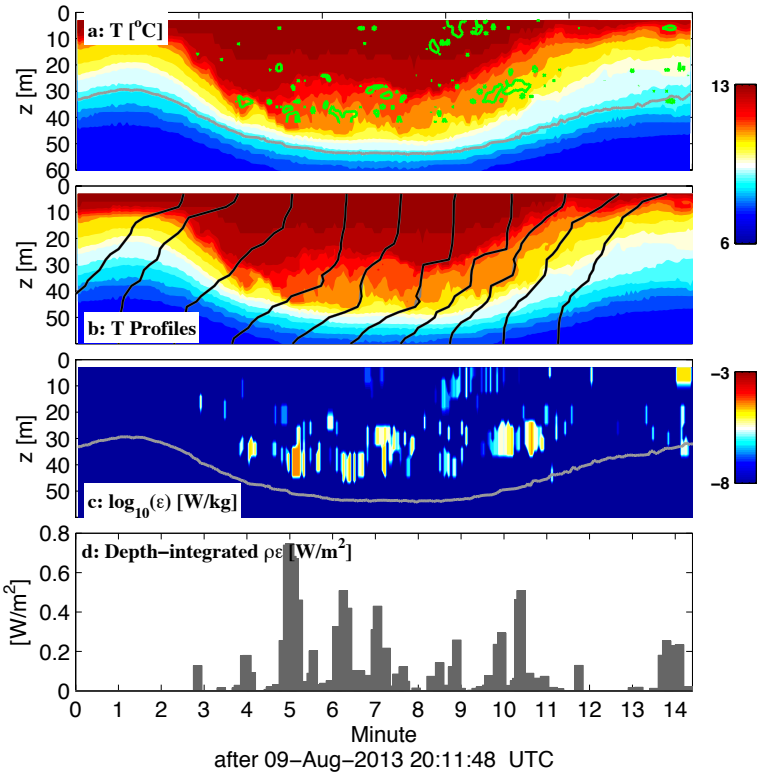

Figure 3.5: Same as Figure 3.4 but for a wave with small temperature overturns detected on August 9, 2013.

3.3 Oceanographic background and basic characteristics of NLIW

The Washington's continental shelf has a seasonal wind-driven circulation. In summer/early fall, northerly winds are predominant (Figure 3.3a), generating a cross-shelf density gradient that sustains a southward shelf current (Figure 3.3c). The observed stratification is strong and concentrated near the surface (Figure 3.3b). In late fall, winds are stronger and predominantly southerly (Figure 3.3a). A northward shelf current dominates the region (Figure 3.3c), resulting in weaker stratification and a deeper pycnocline (Figure 3.3b).

Nonlinear internal waves on the WA shelf (an example shown by a SAR image in Figure 3.1) show a variety of morphologies, including internal solitary waves, solitary wave trains and bores, but are primarily mode-1 depression waves propagating onshore towards the northeast (*Zhang et al.*, submitted). 657 NLIWs are detected in the records in 2013, of which almost all are internal solitary waves arriving in wave trains, with only a few bores (Figure 3.3d). Most arrive semi-diurnally with the internal tide depressions. Because their energy flux is in the same direction and correlated in magnitude with that of the internal tide, *Zhang et al.* (submitted) concluded that they are hypothesized to be generated by shoaling of the internal tide with remote sources. Waves have significant amplitudes relative to water depth (up to 45 m in 100 m water) and energy up to $\sim O(10^8$ J m$^{-1})$. Waves are generally weak in spring/summer and strong in fall (Figure 3.3d), presumably due to variations in background stratification and shear. Unfortunately, our ADCP stopped functioning before the period of strongest waves, so the velocity analysis below is on the early period of weaker waves (Figure 3.3d).

3.4 Categorization of NLIWs based on instability mechanisms

Given that the mid-column mixing at our site is possibly affected by a combination of different processes (winds, tides, etc.), our focus here is instabilities within NLIWs or NLIW-driven mixing. A total of 318 waves out of 657 waves observed (48.4%) are detected to have overturning events and their dissipation rates calculated following the method described in Section 3.2.2. Other waves, for both large and small amplitudes, do not have any detectable turbulence. As previously discussed, based on their instability mechanisms, NLIWs can be grossly categorized into shear-instability (Type I) waves and convective-instability/unstable-core (Type II) waves. An example of a Type I wave (Figure 3.6, left), displays a thin layer of overturns with enhanced dissipation at the wave interface, consistent with the region of highest shear and low Richardson number (~ 0.25). On the other hand, an example of Type II wave (Figure 3.6, right) shows high turbulence levels near the surface, co-located with the largest velocity.

Here we attempt to group observed NLIWs into these two categories based on a dimensionless number representing each wave. It is generally accepted that Richardson number $Ri < 0.25$ ($Ri = \frac{N^2}{S^2}$, where stratification $N^2 = -\frac{g}{\rho}\frac{d\rho}{dz}$, ρ is the potential density, and shear $S^2 = (\frac{\partial u}{\partial z})^2$) indicates shear instability (Type I) (*Miles*, 1961; *Howard*, 1961; *Bogucki and Garrett*, 1993), and Froude number $Fr > 1$ ($Fr = \frac{u}{c}$, where c is the phase speed) indicates convective instability (Type II) (*Gill*, 1982). Because our shear records are under-resolved (4-m bins), we use Froude number Fr for wave characterization, i.e., $Fr < 1$ for non-convective instabilities (Type I) and $Fr > 1$ for convective instabilities (Type II). Approximated by the Dubreil-Jacotin-Long (DJL) phase speed (*Stastna and Lamb*, 2002), i.e., $c \approx c_{\mathrm{DJL}}$ (details discussed in *Zhang et al.* (submitted)), examples of a Type I (Figure 3.6, left) and Type II wave (Figure 3.6, right) have a Froude number of 0.8 and 1.3, respectively, consistent with this catego-

rization.

We can only make the classification based on a subset of the waves with velocity measurements due to the early failure of the ADCP (Figure 3.3, Section 3.2.1), i.e., 130 waves with overturns detected during Apr 24 - Jun 14. Based on this categorization, 108 waves are classified as Type I waves and 22 as Type II waves.

3.5 Temporal variability in midcolumn NLIW-induced mixing

Background conditions have a profound but complicated impact on the NLIW and their mixing, as demonstrated by two week-long examples (Figure 3.7, Figure 3.8). During summer/early fall, when winds are relatively weak and northerly (Figure 3.3a), strong, regular NLIWs are abundant throughout the records (Figure 3.3d). A 7-day period during Aug 7-14, 2013 shows a mean wind speed of 2.2 m s^{-1}, mostly towards the south (Figure 3.7a). A total of 97 NLIWs are detected in this period (Figure 3.7, bd), all of which are mode-1 depression waves. NLIWs generally arrive semi-diurnally in wave trains at internal tide depressions, with a mean (max) wave amplitude of 18 m (36 m). Stratification is strong during this period, with a stable, shallow mixed-layer depth of $\sim 5-8$ m (the depth where temperature is 0.2^oC absolute difference from surface). Enhanced dissipation rates ($\sim O(10^{-6})$ W kg^{-1}) occur twice a day in the thermocline, closely following the arrivals of nonlinear internal wave trains during this period (Figure 3.7, cd).

During spring, when winds are much stronger and frequent storms exist, fewer and smaller NLIWs are detected (Figure 3.3), whose arrivals are irregular. A 7-day period during May 1-8, 2013 shows strong and oscillating winds, with a mean wave speed of 3.4 m s^{-1} (Figure 3.8a). During most of the record, near-surface water is sufficiently mixed by winds, decreasing the stratification in the upper water column and bringing

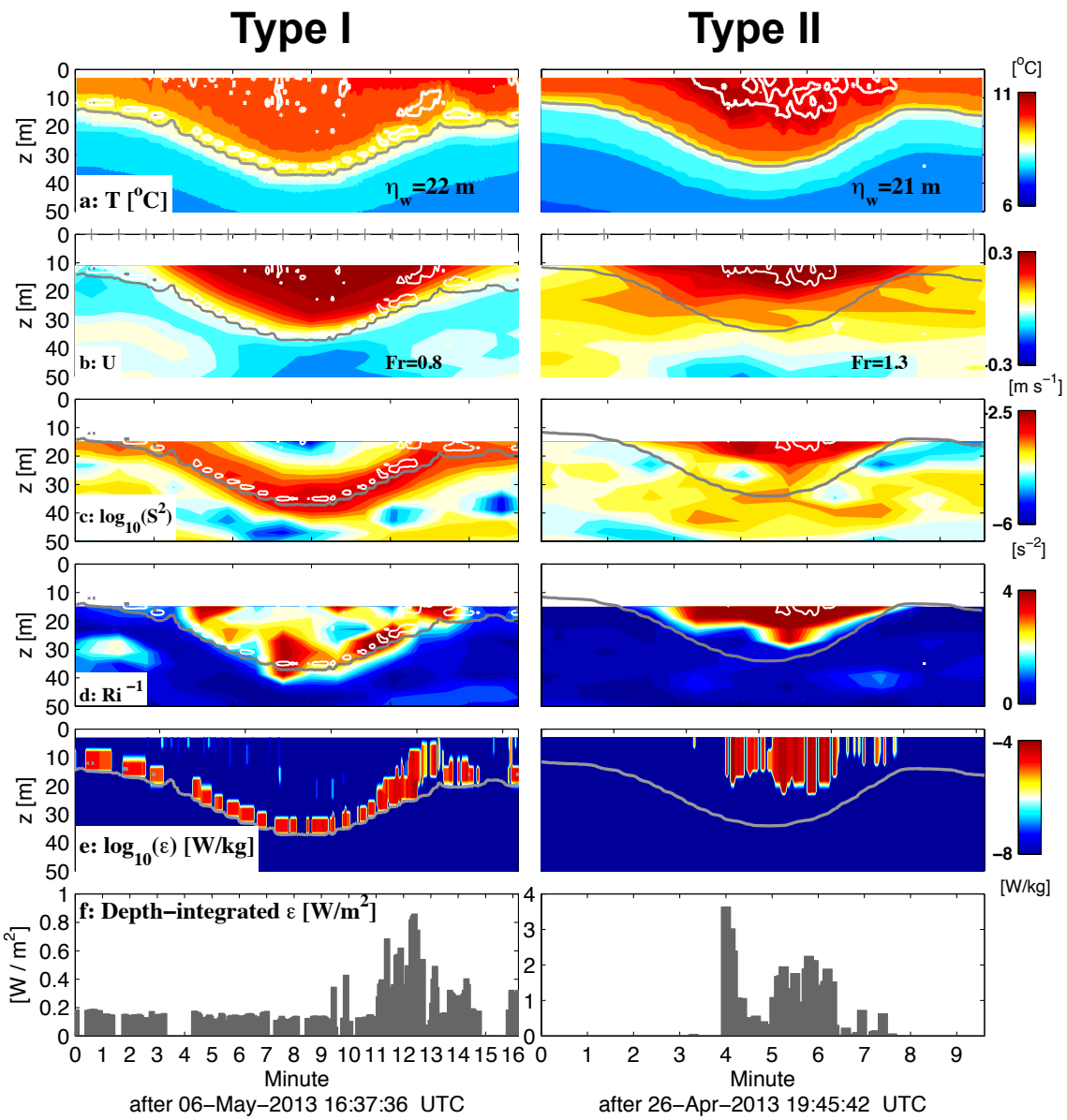

Figure 3.6: Examples of a Type I (left) and a Type II (right) wave, showing times series of temperature (a), velocity along wave propagation direction (b), 4-m velocity shear $log_{10}(S^2)$ (c), Richardson number reverse Ri^{-1}(d), dissipation rates $log_{10}(\epsilon)$ (e), and depth-integrated dissipation (f). Green contours temperature inversion.

down the mixed-layer depth to $\sim 12 - 17$ m. Only 15 NLIWs are detected in this period, with a mean (max) wave amplitude of 14 m (24 m) (Figure 3.8, bd), much smaller than those detected in Figure 3.7, presumably due to the weak stratification and lack of a strong pycnocline to serve as a waveguide. Dissipation in the thermocline ($\sim O(10^{-5})$ W kg^{-1}) is strong and visually not associated with arrivals of NLIWs. It is noted winds slow down from 5 m s^{-1} to 2 m s^{-1} on May 6, accompanied by the growth of strong, regular NLIWs, which are more correlated with the enhanced dissipation rates during May 7-8.

Although these examples suggest that background conditions may have a fundamental impact on formation and evolution of NLIWs, no strong correlations between the waves' dissipation rates and background parameters (e.g., stratification, shear, wave amplitudes) are detected in our records (Figure 3.9). Similarly, the occurrence of each wave category (Type I & II) is irregular as demonstrated in Figure 3.8 (d). Our ADCP was not functioning during some periods with strong NLIWs (e.g., Figure 3.7), thus no wave categorization or their relationship to the background is possible in these periods. Statistical results suggest that though more commonly observed, Type I waves are not typically of larger amplitude than Type II waves (Figure 3.9a). But Type II waves generally have large velocities (> 0.4 m s^{-1}) due to the criterion of $Fr > 1$, with a mean velocity about twice of that of Type I waves (Figure 3.9b).

3.6 Composites of the dissipation rates and other wave quantities

3.6.1 Calculation of wave composites

The average depth structure of waves' quantities (e.g., dissipation rate, shear, velocity) are examined by composite or average the depth values within each category, which take advantage of the similarity in the shape of most waves ("$sech^2$-like"). Bores

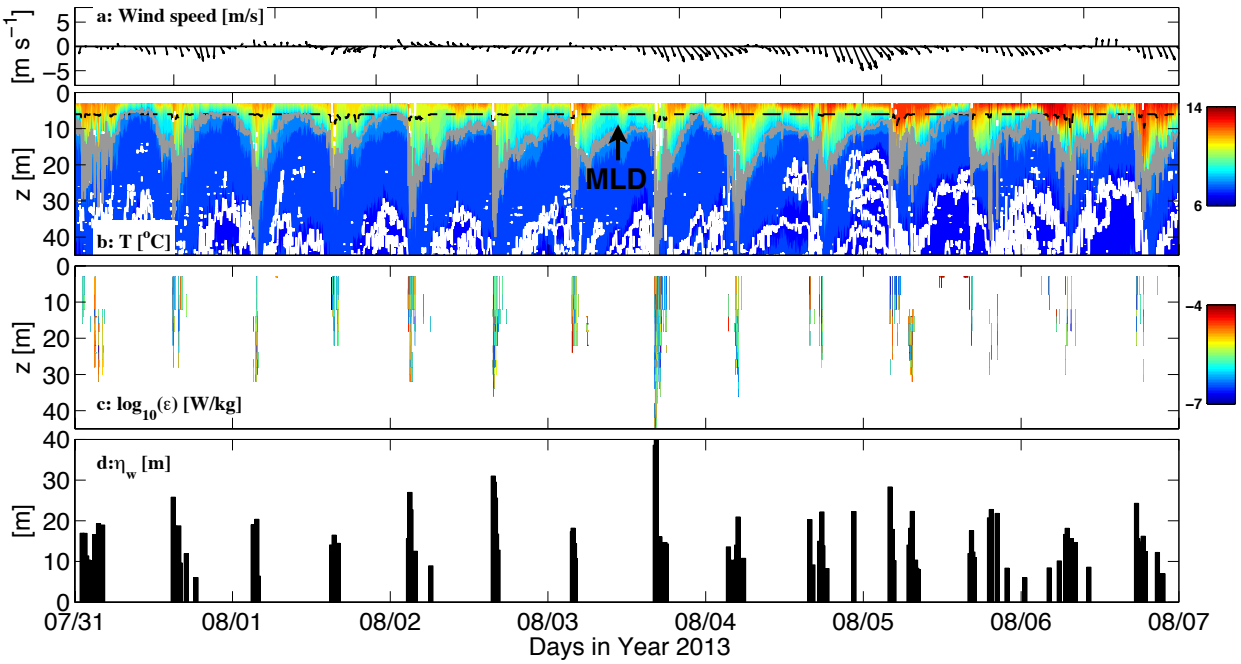

Figure 3.7: A 7-day period showing a scenario of weak winds and strong waves during August 7-14, 2013, with time series of wind speed (a), temperature (b), dissipation rate (c), and NLIW amplitude (d). The black dashed line and grey lines in (b) indicate mixed-layer depth (MLD) and the 9^{o}C isotherm, respectively.

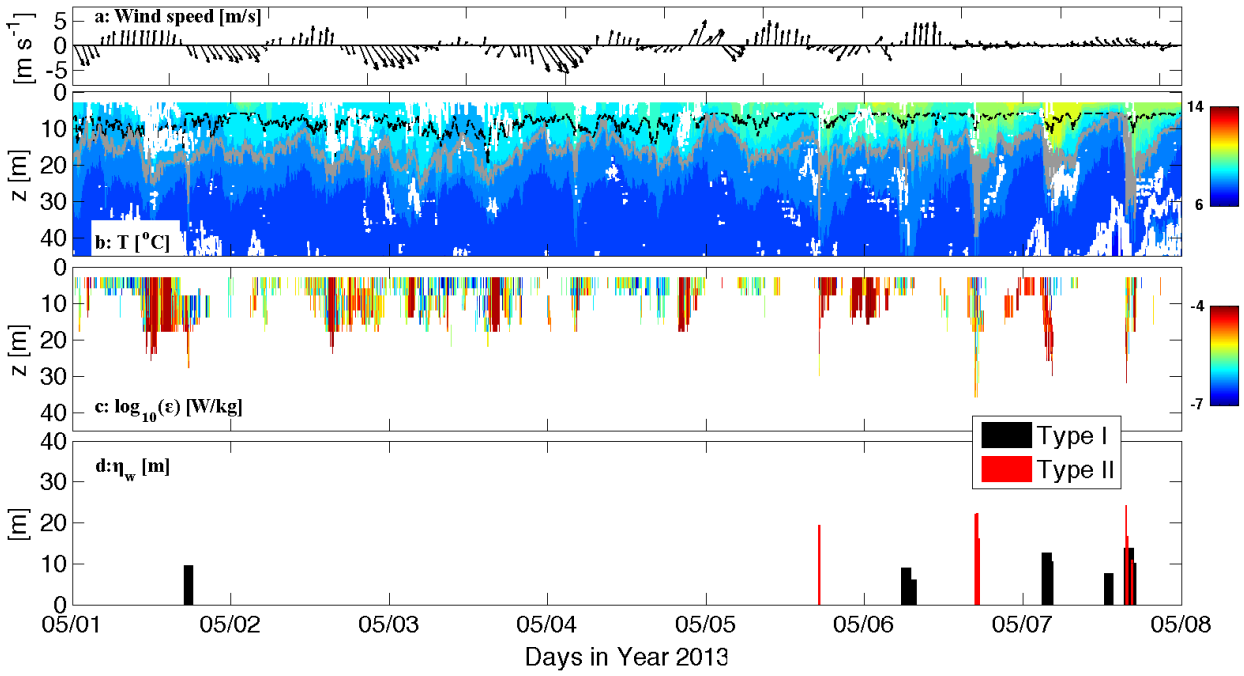

Figure 3.8: A 7-day period showing a scenario of weak winds and strong waves during May 1-8, 2013, with time series of wind speed (a), temperature (b), dissipation rate (c), and NLIW amplitude (d), colored by wave category (Type I as black and Type II as red). The black dashed line and grey line in (b) indicate mixed-layer depth (MLD) and the 8.5^{o}C isotherm, respectively.

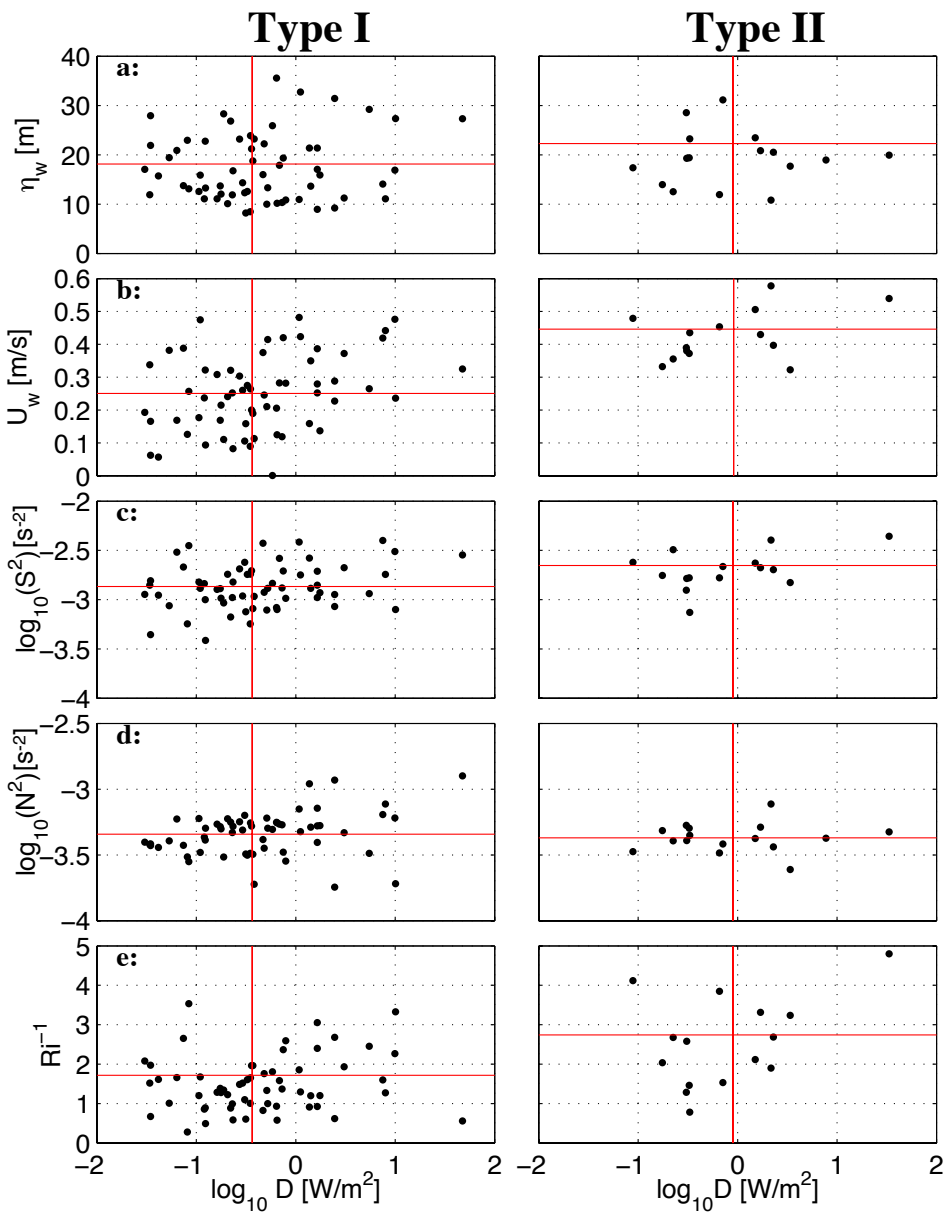

Figure 3.9: Scatter plots showing depth-integrated dissipation rate $log_{10}D$ v.s. wave amplitude η_w (a), maximum velocity within waves U_w (b), shear $\log_{10}(S^2)$ (c), stratification $\log_{10}(N^2)$ (d), Richardson number inverse R_i^{-1} (e) for Type I (left) and Type II (right) waves, with their mean values plotted by red lines.

are a notable exception but only a few bores are detected in the record (Figure 3.3d). The composite wave is generated by first computing the maximum displacement η_w and horizontal wavelength λ_w of each wave, where $\lambda_w = c \cdot t$ and c is approximated by c_{DJL} (discussed in Section 3.4). Then, all waves are averaged together in the normalized coordinates along the wave propagation direction $(\tilde{X}, \tilde{H})$ shown in Figure 3.10, where $\tilde{X} = (X - X(\eta_w))/\lambda_w$, X, $X(\eta_w)$ are the horizontal distance in the wave propagation direction and at the maximum wave displacement, respectively, and $\tilde{H} = H/\eta_w$, H is the vertical displacement. The composite wave quantities, including the composite velocity $\tilde{U}$, 4-m vertical shear $\tilde{S}^2$, Richardson number $\tilde{R}i$, dissipation rate $\tilde{\epsilon}$ and depth-integrated dissipation $\tilde{D}$, are calculated by averaging the values in the normalized wave coordinates over a particular wave set, i.e., Type I, Type II or all the waves (Figure 3.10, b-f).

Of all the 318 waves with detectable overturning events, the composite wave displacement $\tilde{\eta}$ has a typical soliton-like shape (Figure 3.10a), with opposing velocities in the upper/lower depth (Figure 3.10b). In spite of its coarse 4-m vertical resolution, the composite shear has maximum values at the wave interface (Figure 3.10c), roughly co-locates with low Richardson number (Figure 3.10d). Note that due to the early failure of the ADCP, a subset of 130 waves are included in the composites for Figure 3.10, b-d. The composite dissipation rates have enhanced values at the wave interface and inside the wave core (Figure 3.10e), with their depth-integrated values peak at the wave trough (Figure 3.10f). The highest $\tilde{\epsilon}$ values (Figure 3.10e) and $\tilde{D}$ (Figure 3.10f) occur at the wave trough and extend towards the trailing edge, as seen by *Moum et al.* (2003). They suggested that compressed streamlines ahead of the wave trough generate a thin layer of accelerated fluid with high strain and initiate shear instability at the wave trough, which in turn generates a trailing edge and turbulent wake after the trough (their Figure 22). The existence of this pattern in many-wave composites confirms the general importance of the mechanism. Dissipation rate is

also elevated throughout the wave core (Figure 3.10f, gray contours), indicating the average effect of Type II waves.

3.6.2 Composites within each wave category

The composites over all waves show high dissipation at the interface (expected for Type I) and in the wave core (expected for Type II). We form composites for each wave type ($Fr < 1$ and $Fr > 1$, respectively) to attempt to distinguish the structure of the two instability mechanisms.

For the Type I wave state (108 waves: $Fr < 1$), composite shear is concentrated along the wave interface (Figure 3.10, c1), roughly aligned with enhanced composite dissipation rate (Figure 3.10 c1, grey contours). The composite Richardson number is maximum in the same region, but higher than the critical value (Figure 3.10, d1), similar to observations in *Moum et al.* (2003), likely owing to the insufficient sampling resolution (4-m) of velocity. The composite dissipation rate $\tilde{\epsilon}$ is maximum in the region of high values of shear (Figure 3.10, e1), with the highest dissipation rates at the wave trough and extending towards the trailing edge (Figure 3.10, f1). Depth-integrated dissipation value peaks at 1 W m^{-2} around the wave trough (Figure 3.10, f1) but is higher at the trailing edge than the leading edge, consistent with *Moum et al.* (2003).

For the Type II wave state (22 waves: $Fr > 1$), composite dissipation rate has a very different pattern from Type I, showing a maximum inside the wave core (Figure 3.10, e2), mostly in regions of low shear (Figure 3.10, c2). Enhanced $\tilde{\epsilon}$ for Type II waves concentrates in the wave core, mostly in agreement with the region of largest composite velocity (Figure 3.10, b2), expected for waves with convective instabilities, when water speed is faster than the wave propagation speed. Note that the average

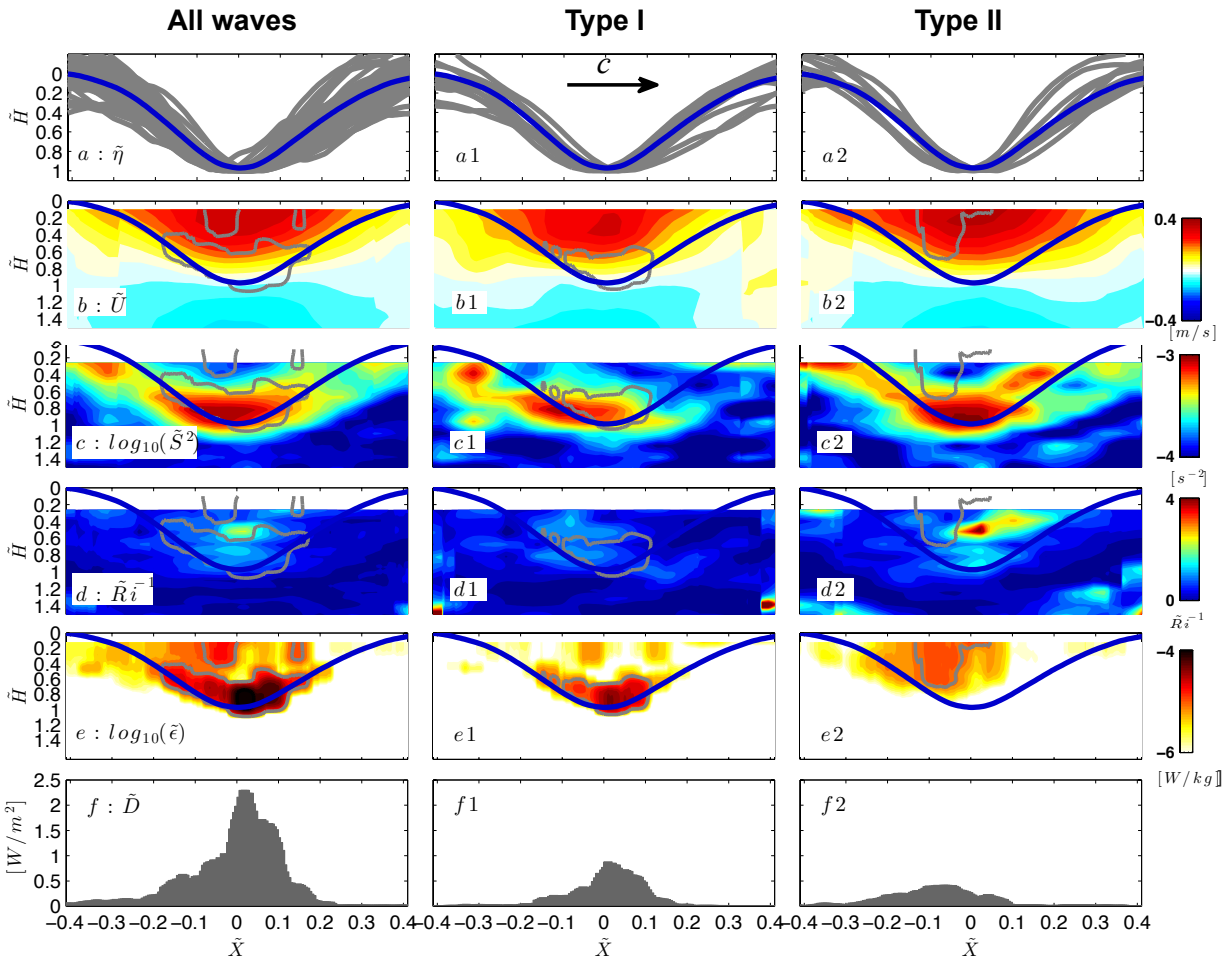

Figure 3.10: Composites for all the waves (left), Type I (middle) and Type II (right) waves in a normalized wave coordinate (see text), showing (a) wave maximum isotherm displacements (gray) and their composite (blue); (b) composite velocity; (c) composite 4-m vertical shear; (d) inverse Richardson number; (e) composite dissipation rate; and (f) depth-integrated dissipation. Gray lines in (b)-(e) indicate 10^{-5} W kg^{-1}.

$\tilde{U}$ within Type II waves is much larger (0.28 m s^{-1}) than the Type I wave (0.1 m s^{-1}) because of the $Fr > 1$ criterion. Depth-integrated dissipation has a small peak at 0.5 W m^{-2}, but generally widely spread throughout the core and the trailing edge (Figure 3.10, f2).

Comparing the composite quantities for Type I, Type II and all the waves (Figure 3.10), $\tilde{\epsilon}$ in Type I suggests stronger, highly focused dissipation in contrast to that in Type II, which is weaker and widely spread over the wave core, typically not as large as those observed in the first category. This is consistent with observations in *Shroyer et al.* (2010a), that they observe most waves with highest dissipation are shear-driven and focused in the trailing edge. Note that the composite dissipation of all waves is applied to a longer dataset (318 waves) through September 2013, while the categorization of waves are only applied to waves with velocity (130 waves). Considering that waves are generally much stronger and more dissipative in August and September, as a seasonal feature of these waves (Section 3.3, Figure 3.3d), $\tilde{\epsilon}$ in Figure 3.10e has larger values than that within each category (Figure 3.10; e1, e2).

3.7 Summary and conclusions

We document observed instabilities in nonlinear internal waves (NLIWs) on the Washington (WA) continental shelf based on a 6-month time series of mooring data. Detectable (> 2 m) overturning instabilities were found in 318 waves out of a total 657 waves and their Thorpe-scale-inferred turbulence documented. Strong temporal variability exists in wave-induced mixing. The wave-induced instability is highly variable in depth and time, with no correlation with background parameters such as wave amplitude or stratification.

In spite of this absent correlation with background states, composites were used

to demonstrate that the spatial structure of the waves' dissipation could be grouped into two classes: shear-instability (Type I) and convective-instability (Type II), as identified by *Moum et al.* (2003) and *Shroyer et al.* (2010a) based on a much smaller sample. Using a Froude number (Fr) criterion, 108 waves are identified as Type I ($Fr < 1$) waves and 22 as Type II ($Fr > 1$) in the 130-wave record with velocity measurements. Composites within each wave category shows that enhanced dissipation rates focus at the interface and in the high-shear area for Type I waves, while Type II waves have elevated dissipation throughout the wave core. Overall, Type I waves are more common, and provide more mixing per wave, suggesting that shear instability is the more important of the two mechanisms at our location.

Chapter 4

SPATIAL VARIABILITY AND PROPAGATION OF NONLINEAR INTERNAL WAVES ON THE WASHINGTON CONTINENTAL SHELF

Nonlinear internal waves (NLIWs) are commonly observed in stratified oceans around the globe, most frequently on continental shelves and marginal seas such as the Oregon coast (e.g., *Stanton and Ostrovsky* (1998); *Klymak and Moum* (2003); *Moum et al.* (2007a); *D'Asaro et al.* (2007)), the New Jersey coast (e.g., *Shroyer et al.* (2011)), Massachusetts Bay (e.g., *Scotti et al.* (2006)), and the South China Sea (e.g., *Duda et al.* (2004); *Klymak et al.* (2006); *Alford et al.* (2010); *Lien et al.* (2012)). It is important to understand their formation, propagation, evolution and dissipation in coastal regions, because they have been observed to transport energy (e.g., *Moum et al.* (2007b); *D'Asaro et al.* (2007)) and mass (e.g., *Inall et al.* (2001); *Shroyer et al.* (2010b)), and to serve as an effective mechanism for mixing (e.g., *MacKinnon and Gregg* (2003); *Moum et al.* (2007a)). NLIWs are usually generated by interaction of tidal currents with bathymetric features such as lee-wave mechanisms released behind ridges or banks (e.g. *Lee and Beardsley* (1974); *Farmer and Smith* (1980); *Maxworthy* (1980); *Farmer and Armi* (1999)), and steepening internal tides at slope-shelf topography (e.g., *Gerkema* (1995); *Colosi et al.* (2001); *Lien et al.* (2005); *Helfrich and Grimshaw* (2008); *Nash et al.* (2012)). By the steepening internal tide mechanism, non-linearized tidal fronts usually form rank-ordered internal solitary wave packets under effects of nonlinearity and dispersion as they grow (e.g. *Helfrich and Melville* (2006)). NLIWs may propagate a long distance from the generation site and retain their shapes without dispersion (*Stanton and Ostrovsky*, 1998; *Klymak et al.*, 2006;

Lien et al., 2012).

A rich, variable nonlinear internal wave field has been reported on the Washington (WA) continental shelf by *Alford et al.* (2012) and *Zhang et al.* (submitted). A satellite image captured an internal solitary wave packet propagating 60^o True (clockwise from north) on the shoaling WA shelf towards the coast (Figure 4.1, lower right). Using statistics based on a large number of waves detected from a long-term mooring system *"ChaBa"* off the WA coast in 2010-2013, general characteristics, generation and instability of these waves have been studied (*Zhang et al.*, submitted; *Zhang and Alford*, submitted). However, one mooring cannot give the spatial structure or information regarding generation, propagation or dissipation of the waves, which remain unknown. As a first step towards these goals, a series of moorings deployed in summer 2013 along five east-west transects spaced off the Washington coast by the Olympic Coast National Marine Sanctuary (OCNMS) were instrumented with temperature measurements sufficient to detect the waves, which typically have 10 - 15 minutes' duration. Comparison between the OCNMS moorings (Figure 4.1, blue stars) and *ChaBa* mooring (Figure 4.1, yellow star) indicates that strong spatial variability exists in the characteristics of NLIWs in this region (e.g., Figure 4.2). By examining their arrival times at different moorings, observed travel times of these waves are compared to their predicted values, which are determined from the DJL equation (described later), taking into account the wave amplitude and direction observed at *ChaBa*. We interpret disagreement between the observed and predicted values the possible importance of background currents in the propagation speed of the waves.

In this chapter, we document the arrival and characteristics of 9 wave packets as they transit 6 moorings on the WA continental shelf (Figure 4.2), with the aim of better understanding their spatial characteristics, evolution, propagation and dynamics. The primary goals of this study are to 1) document the waves' structure as they

cross the WA continental shelf; 2) infer waves' travel times between multiple moorings using their arrivals; 3) estimate wave travel times and compare to theoretical predictions. After first discussing the dataset and our methods, the results will be presented in three parts. First, the waves' spatial characteristics based on multiple moorings will be presented, and their comparison will be discussed. Second, observed travel times between mooring pairs will be computed, and compared to theoretical predictions. Third, wave travel times will be estimated using ray-tracing techniques. We will present the predicted travel times as a function of the wave propagation direction and amplitude and discuss their comparison to observation. A discussion and conclusions follow.

4.1 Data and methods

4.1.1 Mooring "ChaBa"

A surface mooring *"ChaBa"* ($47^o58.0'$N, $124^o57.0'$ W), designed and maintained by University of Washington as aspects of the Northwest Association of Networked Ocean Observing Systems (NANOOS), was deployed for five successive summers/falls from 2010-2014 at a depth of 100 m $\sim$ 25 km off La Push, WA (Figure 4.1). Operational during April 24 - September 23, 2013, *ChaBa* consists of a surface buoy, housing meteorological instruments and communication, a subsurface instrument cage, and a string of instruments mounted along an 81-m mooring wire. Data used in this study mainly include temperature and salinity measurements from conductivity-temperature-depth (CTD) sensors and velocity records from an acoustic Doppler current profiler (ADCP) mounted in a subsurface cage. Temperature was measured every 3 seconds by 40 Seabird Electronics (SBE) 56 T-loggers spaced over a 2-m interval between the surface and 80-m depth. A downward-looking 300 kHz Workhorse ADCP at a depth of 3 m recorded near-full-depth velocity profiles every 1 minute over the battery lifespan

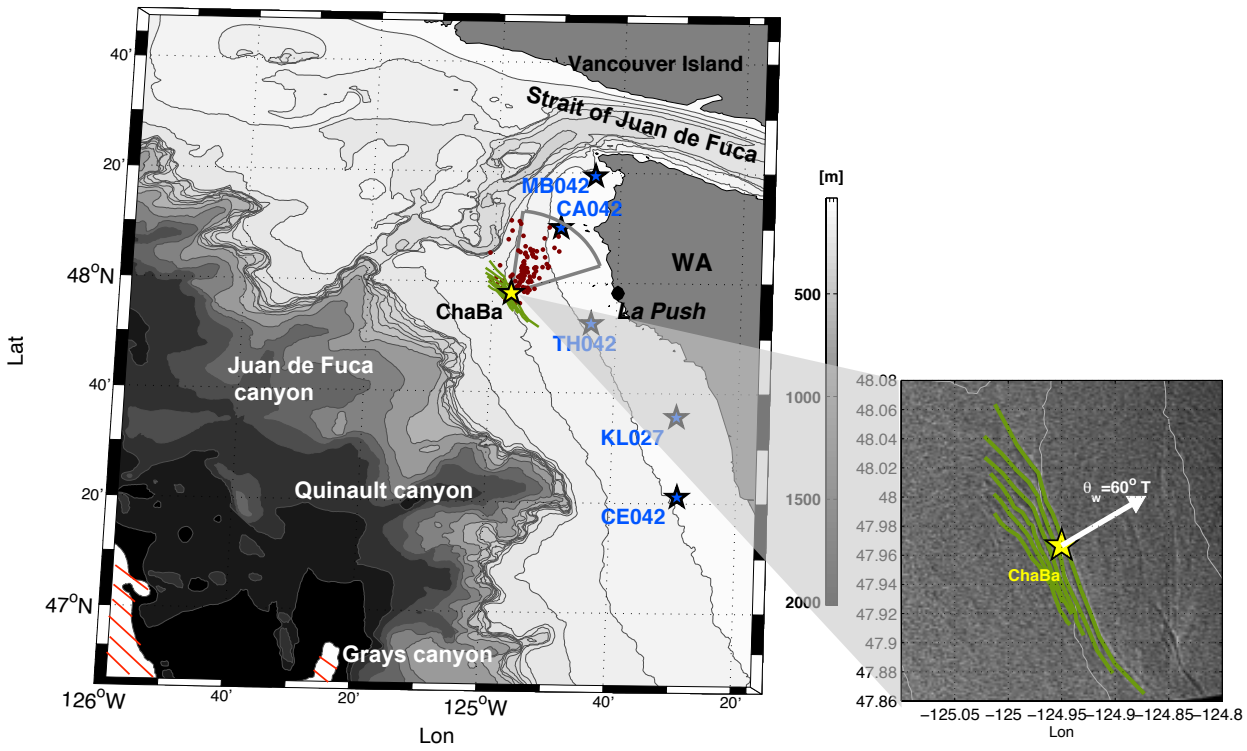

Figure 4.1: A map of the Washington coast with bathymetry and mooring locations (*ChaBa* as yellow and OCNMS moorings as blue). Locations of wave crests captured in a Synthetic Aperture Radar (SAR) image (lower right), which have a mean propagation direction of 60^{o}T, are plotted as green lines. Detected wave velocities and propagation directions at *ChaBa* are plotted as red dots in polar coordinates. The grey wedge denotes velocity directions between 10^{o}T and 80^{o}T with a radius of 0.5 m s^{-1}.

(Aril 24 - June 14).

4.1.2 OCNMS moorings

Since 2004, 13 moorings have been deployed and maintained along five east-west transects spaced off the Washington coast by the Olympic Coast National Marine Sanctuary (OCNMS) at a variety of locations. Design and instrumentation differs by moorings and years. Because nonlinear internal waves usually have a time-scale of

10 - 15 minutes, 5 moorings were instrumented with fast-sampling thermistors, i.e., CA042, TH042, MB042, CE042 at 42-m isobath and KL027 at 27-m isobath (Figure 4.1, blue stars). Data used in this study mainly include temperature measurements from onset HOBO TidbiT temperature loggers (TBI32-05+37, UTBI-001). Temperature was measured every 2 minutes at depths 0.5, 7, 12, 22, 32 m and 41 m at CA042, TH042, MB042, CE042 (Figure 4.2, bcde; thereafter CA, TH, MB and CE) and 0.5, 7, 12, 17 m and 26 m at KL027 (Figure 4.2f, thereafter KL). All five moorings were operational during the period of June 5 - October 11, 2013. Since our focus is tracking the waves across the entire array, only the overlap period of OCNMS moorings and *"ChaBa"* is considered here.

4.1.3 Calculation of wave properties: arrivals, amplitude, propagation direction and phase speed

Wave arrival time, t_w, is determined based on the time of the largest downward displacement inside a wave event (e.g., Figure 4.2, black triangles). Wave amplitude, η_w, is calculated as the maximum isotherm displacement in the wave, i.e. $\eta_w = \eta(z, t_w)_{max}$, where $\eta(z, t_w) = z(t_0) - z(t_w)$, $z(t_w)$, $z(t_0)$ are the isotherm depth during the wave event and in the reference state, respectively.

Because all detected waves are mode-1 depression waves which have opposing deep/shallow flows, the wave propagation direction θ_w is the direction of the shallow flow and is calculated as $tan^{-1}\frac{v_w(z)}{u_w(z)}$ at a depth between 10 m - 35 m following *Chang et al.* (2011), using the fitted slope of v_w over u_w. u_w, v_w are the horizontal wave velocities in Earth coordinates, calculated as velocity measurements in the wave event minus the background flow along streamlines (*Zhang et al.*, submitted). An example of wave propagation direction computed in this manner from the *ChaBa* velocities are shown in Figure 4.1b (arrow). The computed direction (60^o T) agrees well with

the orientation of wave crests detected from SAR at the same time, demonstrating the validity of the given exact technique. Uncertainty in θ_w ($\sim 10^o$) is estimated by comparing θ_w within the same wave train as discussed in *Zhang et al.* (submitted).

Wave speed at *ChaBa* is computed by solving the Dubreil-Jacotin-Long (DJL) model (*Long*, 1953; *Lamb and Wan*, 1998) using measured stratification and wave amplitude. To estimate expected travel time to other moorings without knowledge of the amplitude evolution, we solve a Sturm-Liouville (S-L) equation using stratification at *ChaBa* and the water depth at each location along the shelf. Wave speed at each location x is then computed as $c_{\mathrm{DJL}}(\mathrm{ChaBa}) \cdot c_o(x)/c_o(\mathrm{ChaBa})$. That is, nonlinear speed is computed at *ChaBa*, and then assumed to evolve with depth as would the linear speed.

4.2 Wave spatial features

Waves are strong and abundant at some locations, while weak or nearly absent at some other locations. For example, during a 5-day period of August 9 - 14, 2013, a large number (50) of nonlinear internal waves arriving in 9 wave packets are observed at *ChaBa* (Figure 4.2a), mostly semi-diurnally along with the internal tide. All mode-1, depression waves, NLIWs at *ChaBa* are sharp and narrow (Figure 4.2a), which typically last for 10 - 15 minutes. No internal bores are detected at *ChaBa* during this period. Wave amplitude η_w has a range of 8 - 32 m (Figure 4.3), with a median of 17 m. Propagation direction θ_w is primarily towards the north-east or north-northeast (Figure 4.1, red dots), with a 90% confidence level between 10^o and 80^o (Figure 4.1, wedge).

To the east of *ChaBa*, waves are evident as broad pulses superimposed on a semidiurnal internal tide at mooring CA and TH (Figure 4.2, panels b, c). Unlike mooring

ChaBa, waves at CA or TH do not display pronounced spike-like features, but are wider bores which usually last longer than one hour (Figure 4.2, panels b, c). Waves at CA and TH have the same semidiurnal frequency with waves at *ChaBa*, indicating that they might share the same generation source, possibly the shoaling internal tide. Based on 18 waves detected, wave amplitude η_w at CA ranges from 8 m to 24 m, with a median of 14 m (Figure 4.3), while η_w at TH ranges from 7 m to 15 m with a median of 10 m based on 15 waves detected (Figure 4.3).

Waves at MB, CE and KL are much weaker than at the other moorings, arriving irregularly with no detectable frequency (Figure 4.2, panels d, e, f). Both bore-like and internal-solitary-wave-like NLIWs are detected at MB (Figure 4.2d), but smaller (Figure 4.3) and less regular than that from *ChaBa* or CA. A decent number (13) of waves are detected at KL throughout the period, while there are very few waves detected at CE, suggesting that some waves at KL may be generated at bathymetric features west of KL (e.g., Quinault canyon, Juan de Fuca Canyon) and propagate eastward, instead of at locations to the south (e.g., Grays Canyon).

4.3 Corresponding waves and their observed travel times

Based on previous findings from *ChaBa* (*Alford et al.*, 2012; *Zhang et al.*, submitted) that most waves have a propagation speed of ~ 0.5 m s^{-1} towards the north-east, waves at *ChaBa* should pass by CA, and possibly TH, after approximately 12 hours and 6 hours, respectively. Waves detected at CA and TH around that time window are taken as corresponding waves/wave packets and are paired up with waves at *ChaBa*. Arrival times of corresponding waves at these moorings can be linked up via equation $t = t_w + \Delta$, where t is the wave arrival time at CA or TH, t_w is the arrival time at *ChaBa*, and Δ is the wave travel time.

We first examine the 5-day period during August 9-14, 2013 (Figure 4.2) when strong, regular NLIWs are detected at *ChaBa*, CA and TH. Due to different shapes of NLIWs, i.e., waves arrive in solitary wave trains at *ChaBa* while mostly as internal bores at CA and TH, each wave packet at *ChaBa* is treated as a single wave and its arrival time t_w to be the mean value of arrival times of the waves within the packet (Figure 4.2a, black dashed lines). Similarly, wave arrival time, t, at CA and TH is taken as the mean of the wave train or internal bore (Figure 4.2bc, black dashed lines). The observed travel time $\Delta = t - t_w$ for the 9 wave packets has a range of $\Delta_{\mathrm{CA}} = 8.5 - 10.1$ hr for CA and $\Delta_{\mathrm{TH}} = 6.3 - 10.5$ hr for TH. Note that there are no velocity measurements during this period due to early failure of ADCP (Section 4.1.1).

Another period during Jun 13-14, 2013 with two wave examples (Figure 4.4a, #1, #2) is examined when we do velocity measurements earlier in the records. For Wave #1 (Figure 4.4, upper left) which has an amplitude $\eta_w = 14$ m and a propagation direction $\theta_w = 34^o$ at *ChaBa*, the observed travel time $\Delta_{CA,1} = 10$ hr for CA (Figure 4.4b) and $\Delta_{TH,1} = 5.5$ hr for TH (Figure 4.4c). 12 hours later, another wave packet (Wave #2) with an amplitude of 21 m and a propagation direction of 55^o is detected at *ChaBa* (Figure 4.4, upper right), indicating the variability in wave propagation direction even in a short period of time. The observed travel time for Wave #2 is 9.2 hr for CA (Figure 4.4b) and 6.2 hr for TH (Figure 4.4c). Wave signals at CA are nearly as strong or even stronger than *ChaBa* during this period, while waves at TH are barely detectable, supporting the wave propagating direction towards the (north-)northeast, roughly along the line between *ChaBa* and CA (32.5^o).

4.4 Prediction of wave travel times and comparison to observation

Are the observed arrivals consistent with expected travel times of the waves as they shoal? To investigate, we provide an estimation of the wave travel time Δ as

a function of wave propagation direction θ and speed c, considering the impact from bathymetry only, i.e., no background current/shear or spatial variation in stratification. We hope to get an estimation of the variability in the travel time prediction based on bathymetry alone. By comparing the prediction with observation, the difference gives an idea of possible impacts from other factors such as background currents and shear.

4.4.1 Ray-tracing techniques

Ray paths for three initial angles at *ChaBa*, including the two examples (#1, #2) in Figure 4.4, are calculated using the depth-dependent mode-1 linear phase speed c_0 in the domain (Figure 4.5, upper) by solving a S-L equation at each location of the high-resolution bathymetry, based on the stratification profile measured at *ChaBa*. As described earlier, nonlinear speeds are accounted for by solving the DJL equation using amplitude measured at *ChaBa*, and then assuming that it scales with depth as does the linear speed c_o. To demonstrate the effect of initial propagation directions, ray paths are computed for three waves with the same initial amplitude but different directions. For Wave #1 with an initial propagation direction of 35^o at *ChaBa*, the wave crest is steered eastward as it propagates onshore (Figure 4.5, red) and reaches 55^o as it intersects CA after $\Delta_{\mathrm{CA}} = 19.8$ hr. Wave #2 with an initial propagation direction of 55^o is also steered eastward (Figure 4.5, green) but by a smaller amount. Its propagation direction reaches 65^o after 17.5 hr at the intersection with CA. On the other hand, Wave #3, which has an initial propagation direction of 80^o, remains a nearly constant propagation direction as it propagates onshore since its direction is nearly normal to isobaths (Figure 4.5, black) and arrives at CA after 13 hr, much shorter than that of the other two waves.

4.4.2 Predicted wave travel time Δ

We first examine 9 waves packets during August 9-14 in Figure 4.2 for their predicted travel times. For each wave packet, the amplitude η_w is taken as the amplitude of the leading wave, but the propagation direction θ_w is unknown due to early failure of the ADCP (Section 4.1.1). Instead, a series of θ_w is taken between 10^o and 80^o for each packet, generating predicted travel times to CA and TH for each value of θ_w following the ray-tracing techniques discussed in previous section. The predicted travel times Δ_{CA} has a range of 7-15 hr for all the 9 packets (Figure 4.2b, gray bars), with a mean of 10 hr and a root-mean-square (RMS) of 2.8 hr. The predicted travel times at TH (Figure 4.2c, gray bars) are very different and more sensitive to the initial direction from that at CA, as waves propagating more northward than 23^o can arrive at TH before *ChaBa*. Therefore, the predicted arrival times at TH, Δ_{TH}, has a range of -2 - 10 hr (Figure 4.2c, gray bars), with negative values denote that waves arrive at TH before *ChaBa*.

As discussed before, the predicted wave travel time Δ is a function of wave amplitude and propagation direction. For 4 wave packets in Figure 4.2 (amplitude $\eta_w = 9, 11, 19, 30$ m), Δ is plotted as a function of wave propagation direction θ (Figure 4.6, panel a, b, solid lines). In general, predicted Δ decreases with wave amplitude η_w for both CA and TH during this period, which is expected because larger NLIWs travel faster. Predicted Δ_{CA} increase with θ_w for $\theta_w < 32.5^o$ and decreases with θ_w after that (Figure 4.6, solid lines). Predicted Δ_{TH} always increases with θ_w in this range, with negative values for $\theta_w < 23^o$, indicating northward waves arriving at TH before *ChaBa*.

We also predict travel times for the two wave examples (Wave #1, #2) in Figure 4.4, when their velocities are observed. With the actual wave amplitudes (14 m, 21 m)

and propagation directions (34^o, 55^o), the predicted travel times at CA for Wave #1 and #2 are 13 hr (Figure 4.6a, black star) and 11.2 hr (Figure 4.6a, black triangle), respectively. The predicted travel times at TH are 3.2 hr for Wave #1 and 4.6 hr for Wave #2 (Figure 4.6b, black star and triangle). Wave #1 takes a shorter time to arrive at TH but a longer time to arrive at CA than Wave #2, consistent with our prediction that Δ_{CA} decreases and Δ_{TH} increases with θ_w for a range between $32.5^o - 80^o$.

Uncertainties in the prediction of Δ mainly due to calculation of wave speed and the assumption that no background shelf currents or spatial variation in stratification. As discussed before, the calculation of c_{DJL} has an error bar of about 10% based on previous observational studies (e.g., *Lien et al.* (2012)). The assumption that c_{DJL} scales with depth in the same way as the linear speed c_o introduces additional errors, mainly due to the spatial variation in background shear and stratification when solving a S-L equation.

4.4.3 Comparison to observation

For the 9-wave-packet set (Figure 4.2), their predicted arrival times at CA (Figure 4.2b, horizontal grey bars) are compared with the observed wave arrival times (Figure 4.2b, vertical black dashed lines). The difference between the two has a range of $0 - 6$ hr, with the waves traveling more eastward ($70^o - 80^o$) consistent with the observation (Figure 4.6a). Similarly, prediction at TH agrees better with observation for waves with eastward propagation directions (Figure 4.6b). For waves traveling more northerly ($\theta < 23^o$), the previous packets at TH are used to pair up waves at *ChaBa* (Figure 4.2c, red dashed lines), and the observed travel times agree with predictions for waves with $\theta_w \sim 15^o$ (Figure 4.2c, dash-dot lines).

For the two-wave example (Wave #1, #2) in Figure 4.4, predicted travel times at

CA are 3 hr and 2 hr longer than their observations, for Wave #1 and #2 respectively (Figure 4.4b; Figure 4.6a, red star and triangle). The predicted travel times at TH are shorter than the observation, on the contrary, by 2.1 hr for Wave #1 and 1.5 hr for Wave #2 (Figure 4.4c, Figure 4.6b). At both CA and TH, predictions for Wave #2 are in better agreement with observations, consistent with results from the first set that the predicted travel times are only consistent with more easterly directions.

Due to lack of velocity measurements, we don't know if there is inconsistency for the 9-wave-packet set, but the predicted travel time for wave #1 is inconsistent with observation (Figure 4.6, panel a, b; red and black stars). Predicted travel time for wave #2 is closer to observation, but still with a $\sim$ 2 hr deviation for both CA and TH (Figure 4.6, panel a, b; red and black triangles).

4.5 Discussion

Observed and predicted travel times do not agree for waves propagating towards $15^o - 50^o$, suggesting the importance of other factors, most likely background currents with shear and their spatial variations. Background currents affect travel time by advecting the NLIWs; additionally, background shear alters their phase speed (e.g., (*Lien et al.*, 2012)) as well as affects their evolution (e.g., (*Colosi et al.*, 2001)). Here we demonstrate a simple case that the background currents at *ChaBa* advect NLIWs and shift their propagation directions.

The Washington's continental shelf is dominated by a southward shelf current in spring/summer, which is generated primarily by the northerly alongshore wind stress (*McCreary et al.*, 1987; *Hickey*, 1989). Here we consider a background current $\mathbf{u_0}$ of 0.22 m s^{-1} equatorward in the along-shelf direction (Figure 4.7, grey arrow), which is a mean value from our mooring records over this season, in agreement with *Hickey*

(1989). A nonlinear internal wave with a wave velocity $\mathbf{u_w}$ of 0.5 m s^{-1} towards 35^o (Figure 4.7, black arrow), encounters the current at *ChaBa*, and establishes a total velocity $\mathbf{u}_{\text{total}} = \mathbf{u_0} + \mathbf{u_w}$ towards 80^o, with a magnitude of 0.52 m s^{-1} (Figure 4.7, red arrow). In fact, the 80^o actual propagation direction is consistent with observations from a cruise in August, 2014, during which most waves were found to propagate towards $\sim 35^o$ at *ChaBa* and then to turn towards 80^o after passing it (results presented elsewhere). This simple example only accounts for advection; shear would be more complicated still. Since currents on continental shelves are known to be 1) highly variable and space and time and 2) comparable to the wave speeds, they pose a major problem for accurate prediction of wave arrivals.

4.6 Conclusions

In this paper, we document the arrival and property of 11 wave packets based on the records from 6 synchronous moorings over the Washington (WA) continental shelf, with the aim of better understanding the spatial characteristics, evolution and propagation of these waves and their subsequence dynamics. Our main conclusions include:

1) Strong, sharp waves are abundant at a mooring located on a 100-m mid-shelf (*ChaBa*), while wider, weaker bores are observed at moorings located about 15-20 km onshore on the 42-m inner-shelf (Mooring CA and TH). Fewer waves are detected at moorings elsewhere. NLIWs at *ChaBa* are mostly internal solitary waves that arrive in wave packets, while waves at CA and TH are mostly internal bores, indicating significant evolution of the waves as they transit between the moorings. Both wave packets and bores arrive semi-diurnally with the internal tide, indicating the same source for these waves;

2) Wave arrival times detected at *ChaBa*, CA and TH have a difference of $\sim$ 10 hr between *ChaBa* and CA and $\sim$ 8 hr between *ChaBa* and TH;

3) The travel time Δ for each wave packet at *ChaBa* is predicted at CA and TH using the ray-tracing techniques for a range of propagation directions θ_w between 10^o and 80^o. Comparison to the observed travel times suggests that our prediction of Δ is consistent for waves with $70^o < \theta_w \leq 80^o$, but inconsistent for waves in the other directions. This disagreement indicates that the background currents with shear also affect propagation of NLIWs. A shelf current orientation that is equator-ward in the alongshore direction is demonstrated to advect the waves more towards the east as suggested by these calculations.

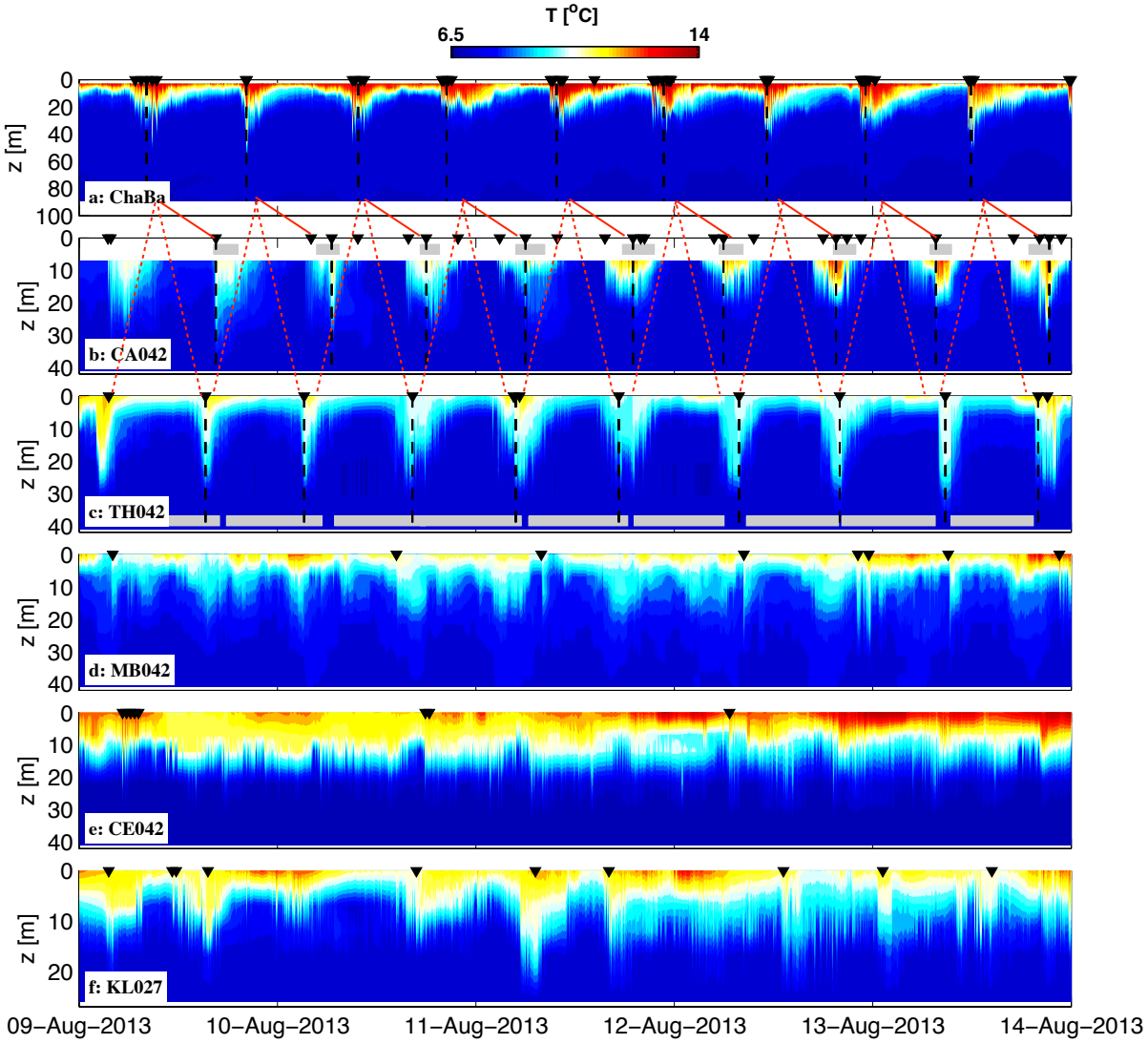

Figure 4.2: Temperature time series during August 9 - 14, 2013 from *ChaBa* (a), CA042 (b), TH042 (c), MB042 (d), CE042 (e) and KL027 (f). Black triangles and vertical dashed lines are detected arrival times of waves and wave packets at each mooring, respectively. Grey bars in (b) and (c) are predicted wave arrival times (see text). Red solid (dashed) lines indicate corresponding waves between *ChaBa* and CA (TH).

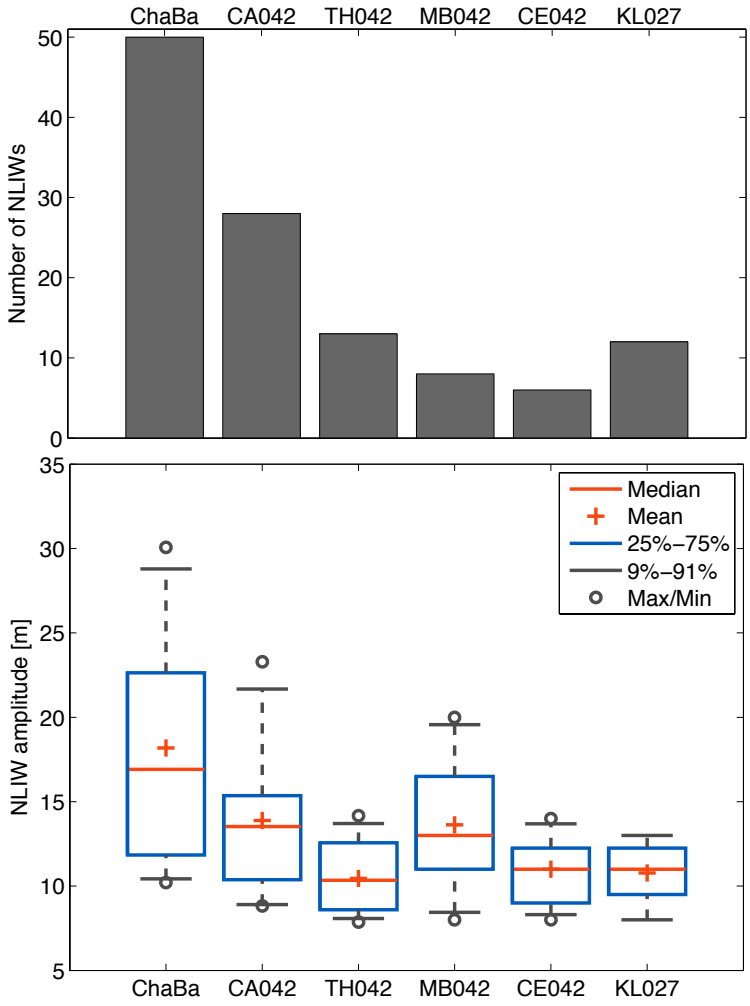

Figure 4.3: Bar plots showing number of waves (upper) and histograms with whiskers showing wave amplitude η_w (lower) for detected NLIWs at *ChaBa*, CA, TH, MB, CE and KL in Figure 4.2.

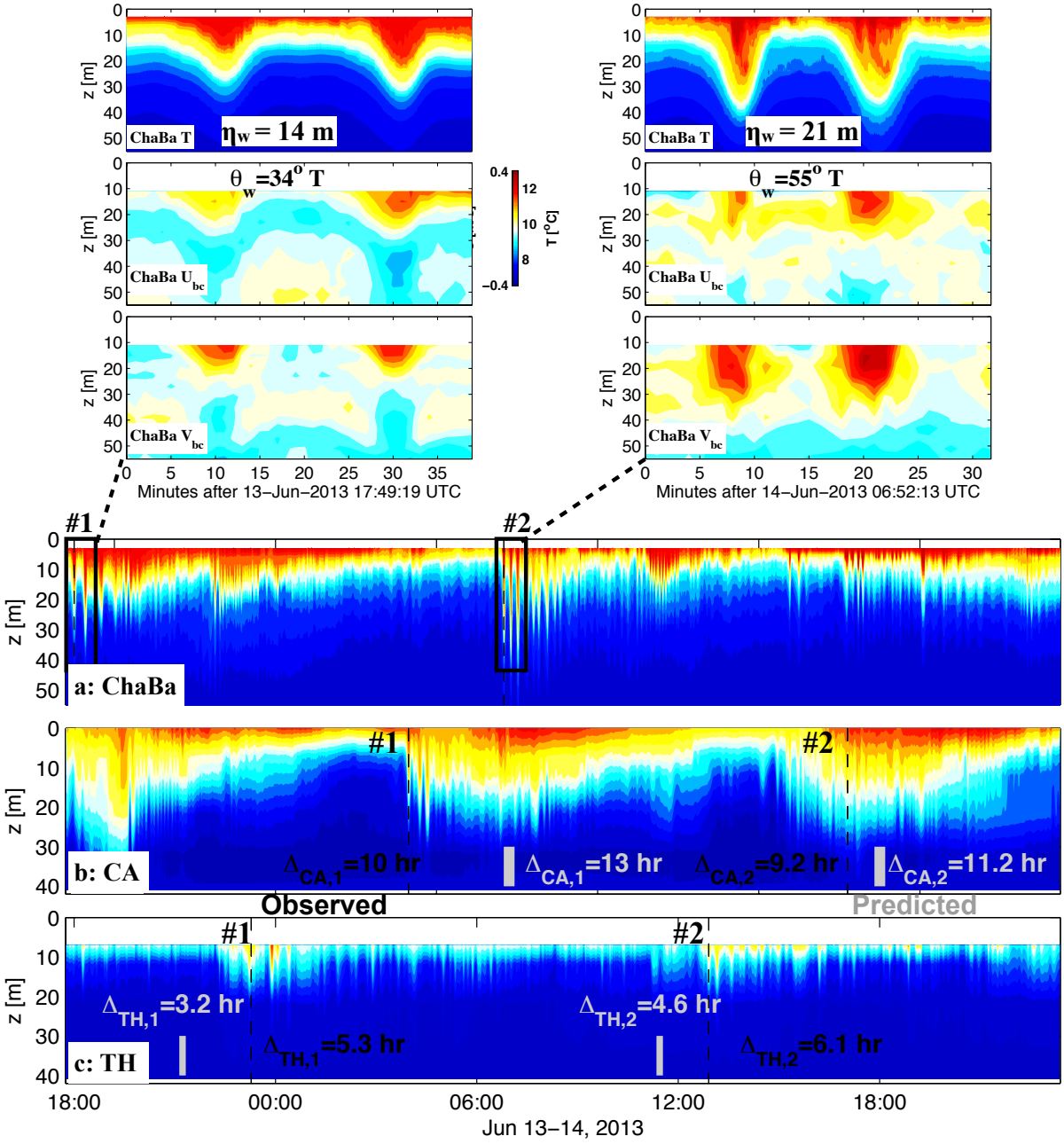

Figure 4.4: Time series of temperature from *ChaBa* (a), CA (b) and TH (c) during June 13-14, 2013, with zoomed-in plots for Wave Case #1 (upper left) and Wave Case #2 (upper right).

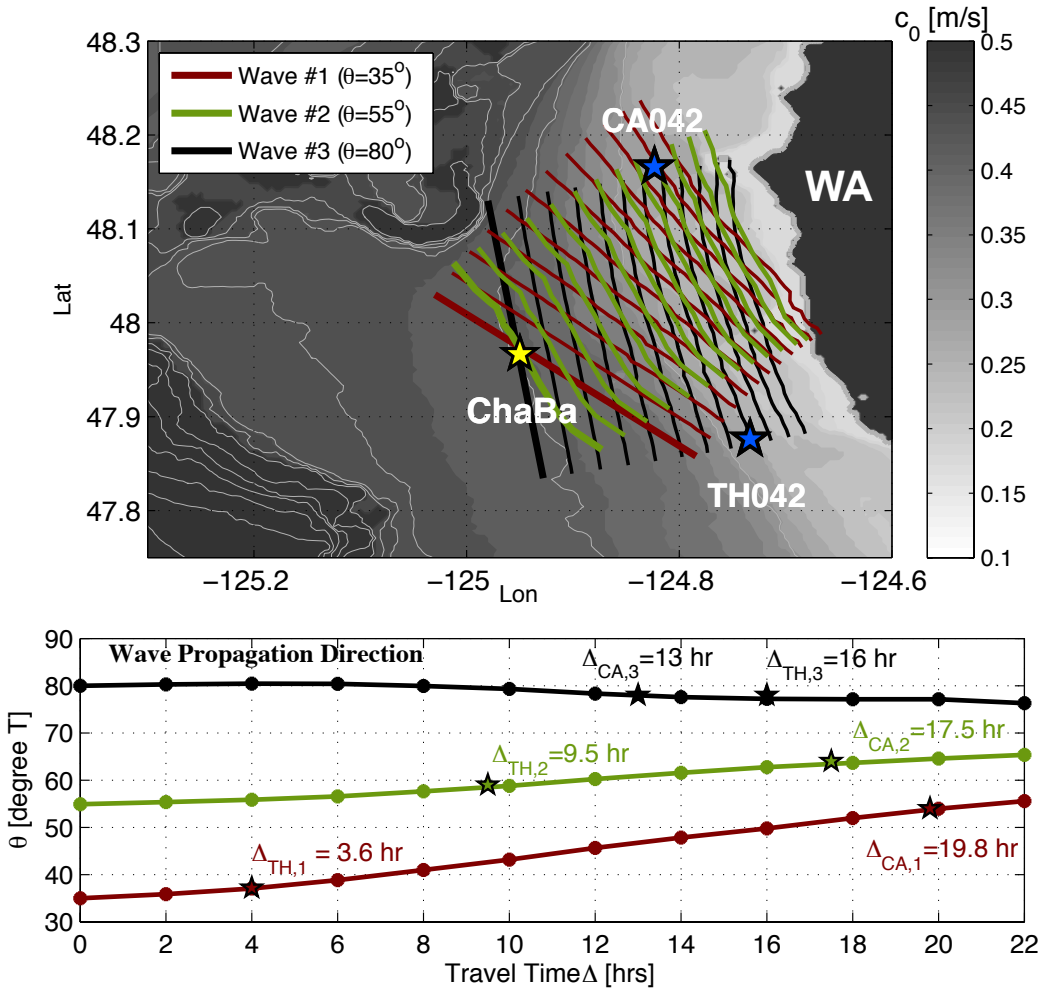

Figure 4.5: (upper) A map of linear phase speed c_0 with bathymetry embedded on. Wave crests with three initial angles (35^o, 55^o and 80^o) at *ChaBa*, corresponding to the two examples (Wave #1, #2) in Figure 4.4 and Wave #3, respectively, are plotted as red, green and black line for every 2 hours. (lower) Wave propagation direction θ plotted over the wave travel time Δ for Wave #1, #2 and #3.

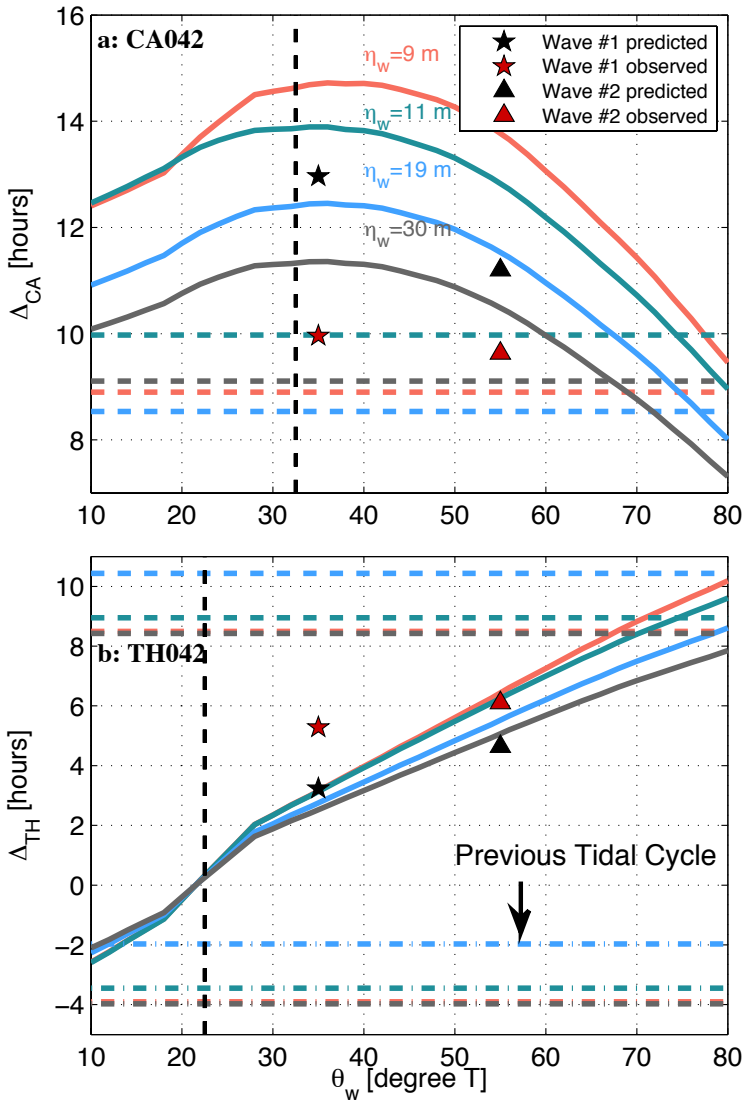

Figure 4.6: (a) Predicted (color solid lines) and observed (color dashed lines) travel times at CA (Δ_{CA}) plotted over wave propagation direction θ_w for 4 wave packets (see text). Two wave cases in Figure 4.4 are overplotted as star (Wave #1) and triangle (Wave #2), showing both observed (red) and predicted (gray) values of Δ_{CA}. (b) Same as in (a) but for TH. Dash-dot lines in (b) are observed wave travel times using waves in a previous tidal cycle (see text).

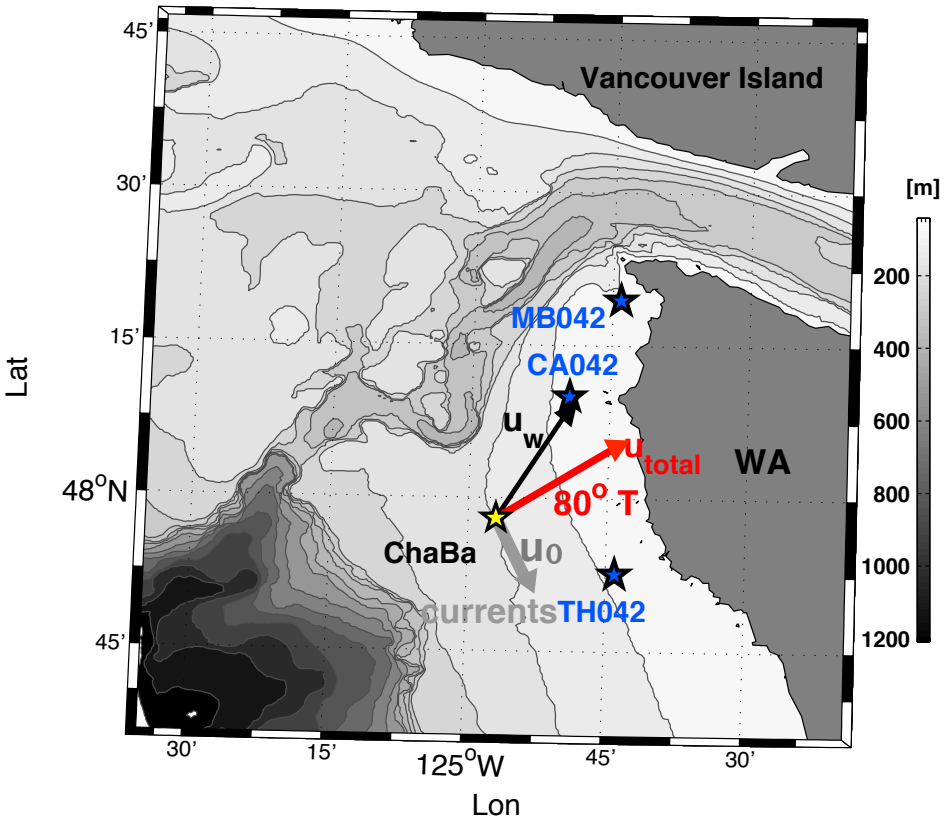

Figure 4.7: A map of the Washington coast with bathymetry, mooring locations (*ChaBa* as yellow and OCNMS moorings as blue), a background current of 0.22 m s^{-1} equatorward in the along-shelf direction (grey arrow), a wave velocity $\mathbf{u_w}$ of 0.5 m s^{-1} towards 35^o T (black arrow), and a total velocity for the wave $\mathbf{u}_{\text{total}}$ towards 80^o T, with a magnitude of 0.52 m s^{-1} (red arrow).

Chapter 5

CONCLUSIONS

This dissertation characterizes the nonlinear internal waves (NLIW) observed on the Washington (WA) continental shelf based on measurements from a moored ADCP/thermistor chain with varied vertical spacing during 2010-2013. Strong, sufficient NLIWs are detected and their temporal/spatial variabilities documented. The current study is the first detailed study focused on characterizing NLIWs off the WA coast and exploring their characteristics, generation, transport, instabilities and spatial variability. The main conclusions include

- Based on a long time series of 4 years, a large number (> 1500) of NLIWs are detected and their taxonomy (internal solitary waves, solitary wave trains and internal bores) documented. Observed wave characteristics in four years have similar features: onshore propagation direction towards the northeast; significant amplitude relative to water depth (up to 51 m in 100 m water); and wave energy up to $\sim O(10^8$ J m$^{-1})$. Waves are generally weak in spring/early summer, strong in late summer/fall, and absent in winter, presumably due to variations in background stratification and currents that impact wave generation and propagation.

- NLIWs appear to be generated by shoaling of remotely-incident internal tides (IT) instead of by local barotropic conversion, suggested by 1) semi-diurnal wave arrivals are often phase-locked with the internal tide; 2) the propagation direction of NLIWs and the IT energy flux direction are consistent, with NLIWs steered more onshore by the bathymetry; 3) NLIW and IT energy flux

are correlated; and 4) NLIW energy flux and the local barotropic forcing are uncorrelated.

- Estimated onshore transport by the waves can equal or exceed offshore Ekman transport, suggesting the waves may play an important role in the mass balance on the continental shelf.

- Waves with overturning instabilities are examined and their Thorpe-scale-inferred turbulence documented based on a 6-month dataset with temperature sampled at a 2-m vertical interval. Categorized based on the instability mechanisms by which NLIWs induce mixing, waves are identified as shear-instability (Type I: Fr <1) waves and convective instability (Type II: Fr > 1) using a Froude (Fr) number criterion. Strong temporal variability exists in wave-induced mixing. The wave-induced instability is highly variable in depth and time, with no correlation with background parameters such as wave amplitude or stratification. In spite of this absent correlation with background states, composites are constructed by averaging over all waves in each category to examine the mean spatial structure of dissipation for each. Turbulence is the highest at the sheared interface for Type I waves and throughout the wave core for Type II waves, consistent with previous studies by *Moum et al.* (2003) and *Shroyer et al.* (2010a) but based on a much larger wave set.

- wave spatial variability is examined using 6 synchronous mooring arrays deployed on the WA continental shelf. Strong, sharp internal solitary wave trains evident at the 100-m mid-shelf, transform to wider, weaker internal bores as they propagate onto the 42-m inner-shelf moorings, and are much weaker and fewer at moorings elsewhere. Based on their regular arrivals, the same waves can be detected between mooring pairs and their travel times recorded. Based on ray-tracing techniques with impacts from bathymetry only, the wave travel

time, Δ, is estimated as a function of wave propagation direction θ. Comparison with observation suggests that our prediction of Δ is in agreement with observation for waves towards the east ($70^o < \theta \leq 80^o$ T), but inconsistent for waves towards the north-northeast ($15^o < \theta \leq 50^o$ T) with errors up to 4 hours. This disagreement indicates that bathymetry alone does not fully explain the evolution and propagation of NLIWs. A shelf current orientation that is directed equator-ward alongshore is demonstrated to advect the waves eastward and alter the wave travel times.

BIBLIOGRAPHY

Alford, M., and R. Pinkel (2000a), Patterns of turbulent and double diffusive phenomena: Observations from a rapid profiling conductivity probe, *J. Phys. Oceanogr.*, *30*, 833–854.

Alford, M. H. (2003), Energy available for ocean mixing redistributed through long-range propagation of internal waves, *Nature*, *423*, 159–163.

Alford, M. H., and R. Pinkel (2000b), Observations of overturning in the thermocline: The context of ocean mixing, *J. Phys. Oceanogr.*, *30*, 805–832.

Alford, M. H., and Z. Zhao (2007), Global patterns of low-mode internal-wave propagation, Part I: Energy and energy flux, *J. Phys. Oceanogr.*, *37*(7), 1829–1848.

Alford, M. H., M. C. Gregg, and M. A. Merrifield (2006), Structure, propagation and mixing of energetic baroclinic tides in Mamala Bay, Oahu, Hawaii, *J. Phys. Oceanogr.*, *36*(6), 997–1018.

Alford, M. H., R. Lien, H. Simmons, J. M. Klymak, Y. Yang, D. Tang, and M. Chang (2010), Speed and evolution of nonlinear internal waves transiting the South China Sea, *J. Phys. Oceanogr.*, *40*(6), 1338–1355.

Alford, M. H., J. B. Mickett, S. Zhang, Z. Zhao, and J. Newton (2012), Internal waves on the Washington continental shelf, *Oceanography*, *25*(2), 66–79.

Allen, S., and B. Hickey (2010), Dynamics of advection-driven upwelling over a shelf break submarine canyon, *Journal of Geophysical Research*, *115*(C8), C08,018.

Apel, J., L. Ostrovsky, Y. Stepanyants, and J. Lynch (2006), Internal solitons in the ocean, *Tech. rep.*, Woods Hole Oceanographic Institution.

Apel, J. R., J. R. Holbrook, A. K. Liu, and J. J. Tsai (1985), The Sulu Sea internal soliton experiment, *J. Phys. Oceanogr.*, *15*, 1625–1651.

Baines, P. (1974), the generation of internal tides over steep continental slopes, *277*, 27–58.

Banas, N., E. Lessard, R. Kudela, P. MacCready, T. Peterson, B. Hickey, and E. Frame (2009), Planktonic growth and grazing in the columbia river plume region: A biophysical model study, *Journal of Geophysical Research: Oceans (1978–2012)*, *114*(C2).

Batchelor, G. K. (1959), Small-scale variation of convected quantitites like temperature in turbulent fluid, *J. Fluid Mech.*, *5*, 113–139.

Bogucki, D., and C. Garrett (1993), A simple model for the shear-induced decay of an internal solitary wave, *J. Phys. Oceanogr.*, *23*, 1767–1776.

Bogucki, D., T. Dickey, and L. Redekopp (1997), Sediment resuspension and mixing by resonantly generated internal solitary waves, *J. Phys. Oceanogr.*, *27*(7), 1181–1196.

Chang, M., R. Lien, Y. Yang, and T. Tang (2011), Nonlinear internal wave properties estimated with moored adcp measurements, *Journal of Atmospheric and Oceanic Technology*, *28*(6), 802–815.

Colosi, J. A., R. C. Beardsley, J. F. Lynch, G. Gawarkiewicz, C. S. Chiu, and A. Scotti (2001), Observations of nonlinear internal waves on the outer New England continential shelf during the summer Shelfbreak Primer Study, *J. Geophys. Res.*, *106*(C5), 9587–9601.

D'Asaro, E., R. Lien, and F. Henyey (2007), High-frequency internal waves on the oregon continental shelf, *J. Phys. Oceanogr.*, *37*(7), 1956–1967.

Dillon, T. M. (1982), Vertical overturns: A comparison of Thorpe and Ozmidov length scales, *J. Geophys. Res.*, *87*, 9601–9613.

Dillon, T. M., and D. R. Caldwell (1980), The Batchelor spectrum and dissipation in the upper ocean, *J. Geophys. Res.*, *85*(C4), 1910–1916.

Duda, T. F., and D. M. Farmer (1999), The 1998 whoi/ios/onr internal solitary wave workshop: contributed papers, *Tech. rep.*, DTIC Document.

Duda, T. F., J. F. Lynch, J. D. Irish, R. C. Beardsley, S. Ramp, C.-S. Chiu, T.-Y. Tang, and Y.-J. Yang (2004), Internal tide and nonlinear internal wave behavior at the continental slope in the northern South China Sea, *IEEE J. of Oceanic Engr.*, *29*(4), 1–27.

Ekman, V. W. (1905), On the influence of the earth's rotation on ocean-currents, *Ark. Mat. Astron. Fys.*, *2*, 1–52.

Farmer, D. M., and L. Armi (1999), The generation and trapping of solitary waves over topography, *Science*, *283*, 188–190.

Farmer, D. M., and J. D. Smith (1980), Generation of lee waves over the sill in Knight Inlet, in *Fjord Oceanography*, edited by H. J. Freeland, D. M. Farmer, and C. Levings, pp. 259–269, Plenum Press, New York.

Gerkema, T. (1995), A unified model for the generation and fission of internal tides and solitary waves, *J. Mar. Res.*, *54*, 421–450.

Gill, A. E. (1982), *Atmosphere-Ocean Dynamics*, 662 pp., Academic.

Helfrich, K. R., and R. H. J. Grimshaw (2008), Nonlinear disintegration of the internal tide, *J. Phys. Oceanogr.*, *38*, 686–701.

Helfrich, K. R., and W. Melville (1986), On long nonlinear internal waves over slope-shelf topography, *Journal of Fluid Mechanics*, *167*(1), 285–308.

Helfrich, K. R., and W. K. Melville (2006), Long nonlinear internal waves, *Ann. Rev. Fluid Mech.*, *38*, 395–425.

Henyey, F. S. (1999), Exact solitary wave solutions in shallow water, in *Aha Huliko'a Hawaiian Winter Workshop*, pp. 89–93, DTIC Document.

Henyey, F. S., and A. Hoering (1997), Energetics of borelike internal waves, *J. Geophys. Res.*, *102*(C2), 3323–3330.

Hickey, B. M. (1989), Patterns and processes of circulation over the washington continental shelf and slope, *Elsevier Oceanography Series*, *47*, 41–115.

Hickey, B. M. (1995), Coastal submarine canyons, in *Topographic Effects in the Ocean, Proceedings Hawaiian Winter Workshop, Jan. 17–20, 1995*, edited by P. Müller and D. Henderson, pp. 95–110, Hawaii Institute of Geophysics, Honolulu, HI 96822.

Hickey, B. M., and N. E. S. Banas (2008), Why is the northern California Current so Productive? , *Oceanography*, *21*(4), 90.

Hickey, B. M., and N. S. Banas (2003), Oceanography of the U.S. Pacific Northwest coastal ocean and estuaries with application to coastal ecology, *Estuaries*, *26*(4B), 1010–1031.

Holliday, D., and M. E. McIntyre (1981), On potential energy density in an incompressible, stratified fluid, *J. Fluid Mech.*, *107*, 221–225, (verified).

Howard, L. N. (1961), Note on a paper of John W. Miles, *J. Fluid Mech.*, *10*, 509–512.

Huthnance, J. M. (1995), Circulation, exchange and water masses at the ocean margin: the role of physical processes at the shelf edge, *Progress in Oceanography*, *35*(4), 353–431.

Inall, M., G. Shapiro, and T. Sherwin (2001), Mass transport by non-linear internal waves on the Malin Shelf, *Continental Shelf Research*, *21*(13), 1449–1472.

Inall, M. E., T. P. Rippeth, and T. J. Sherwin (2000), Impact of nonlinear waves on the dissipation of internal tidal energy at a shelf break, *J. Geophys. Res.*, *105*(C4), 8687–8705.

Kang, D., and O. Fringer (2010), On the calculation of available potential energy in internal wave fields, *Journal of Physical Oceanography*, *40*(11), 2539–2545.

Klymak, J. M., and J. N. Moum (2003), Internal solitary waves of elevation advancing on a shoaling shelf, *Geophys. Res. Lett.*, *30*(20), 2045, doi:10.1029/2003GL017,706.

Klymak, J. M., R. Pinkel, C. Teng Liu, A. K. Liu, and L. David (2006), Prototypical solitons in the South China Sea, *J. Geophys. Res.*, *33*(L11607), doi:10.1029/2006GL025,932.

Lamb, K. (2002), A numerical investigation of solitary internal waves with trapped cores formed via shoaling, *Journal of Fluid Mechanics*, *451*, 109–144.

Lamb, K. (2010), Energetics of internal solitary waves in a background sheared current, *Nonlin. Processes Geophys*, *17*, 553–568.

Lamb, K. G. (1997), Particle transport by nonbreaking, solitary internal waves, *Journal of Geophysical research*, *102*(C8), 18,641–18.

Lamb, K. G. (2003), Shoaling solitary internal waves: on a criterion for the formation of waves with trapped cores, *Journal of Fluid Mechanics*, *478*, 81–100.

Lamb, K. G. (2007), Energy and pseudoenergy flux in the internal wave field generated by tidal flow over topography, *Continental shelf research*, *27*(9), 1208–1232.

Lamb, K. G. (2014), Internal wave breaking and dissipation mechanisms on the continental slope/shelf, *Ann. Rev. Fluid Mech.*, *46*, 231–254.

Lamb, K. G., and V. T. Nguyen (2009), Calculating energy flux in internal solitary waves with an application to reflectance, *Journal of Physical Oceanography*, *39*(3), 559–580.

Lamb, K. G., and B. Wan (1998), Conjugate flows and flat solitary waves for a continuously stratified fluid, *Physics of Fluids*, *10*, 2061.

Lee, C.-Y. u., and R. C. Beardsley (1974), The generation of long nonlinear internal waves in a weakly stratified shear flow, *J. Geophys. Res.*, *79*(3), 453–462.

Legg, S., and A. Adcroft (2003), Internal Wave Breaking at Concave and Convex Continental Slopes, *J. Phys. Oceanogr.*, *33*(11), 2224–2246.

Lentz, S. J. (1992), The surface boundary layer in coastal upwelling regions, *J. Phys. Oceanogr.*, *22*(12), 1517–1539.

Levine, M. D., and T. J. Boyd (2006), Tidally forced internal waves and overturns observed on a slope: Results from HOME, *J. Phys. Oceanogr.*, *36*(6), 1184–1201.

Lien, R., E. A. D'Asaro, F. Henyey, M. Huei Chang, T. Yung Tang, and Y.-J. Yang (2012), Trapped core formation within a shoaling nonlinear internal wave, *J. Phys. Oceanogr.*, *42*(4), 511–525.

Lien, R.-C., T. Y. Tang, M. H. Chang, and E. A. D'Asaro (2005), Energy of nonlinear internal waves in the South China Sea, *Geophys. Res. Lett.*, *32*(L05615), doi:10.1029/2004GL022,012.

Lien, R.-C., T. B. Sanford, S. Jan, M.-H. Chang, and B. B. Ma (2013), Internal tides on the east china sea continental slope, *Journal of Marine Research*, *71*(1-2), 1–2.

Long, R. R. (1953), Some aspects of the flow of stratified fluids.I. A theoretical investigation, *Tellus*, *V*, 42–58.

MacFadyen, A., B. Hickey, and W. Cochlan (2008), Influences of the Juan de Fuca Eddy on circulation, nutrients, and phytoplankton production in the northern California Current System, *Journal of Geophysical Research*, *113*(C8), C08,008.

MacKinnon, J. A., and M. C. Gregg (2003), Mixing on the late-summer New England Shelf- Solibores, shear, and stratification, *J. Phys. Oceanogr.*, *33*, 1476–1492.

MacKinnon, J. A., and M. C. Gregg (2005), Spring mixing: Turbulence and internal waves during restratification on the New England Shelf, *J. Phys. Oceanogr.*, *35*(12), 2425–2443.

Mater, B. D., S. M. Schaad, and S. K. Venayagamoorthy (2013), Relevance of the thorpe length scale in stably stratified turbulence, *PHYSICS OF FLUIDS*, *25*(076604).

Maxworthy, T. (1980), On the formation of nonlinear internal waves from the gravitational collapse of mixed regions in two and three dimensions, *Journal of Fluid Mechanics*, *96*(1), 47–64.

McCreary, J. P., P. K. Kundu, and S.-Y. Chao (1987), On the dynamics of the california current system, *Journal of Marine Research*, *45*(1), 1–32.

Miles, J. W. (1961), On the stability of heterogeneous shear flows, *J. Fluid Mech.*, *10*, 496–508.

Moum, J., and J. Nash (2009), Mixing measurements on an equatorial ocean mooring, *J. Atmos. Ocean. Tech.*, *26*, 317–336.

Moum, J., D. Farmer, E. Shroyer, W. Smyth, and L. Armi (2007a), Dissipative losses in nonlinear internal waves propagating across the continental shelf, *Journal of Physical Oceanography*, *37*(7), 1989–1995.

Moum, J. N., D. M. Farmer, W. D. Smyth, L. Armi, and S. Vagle (2003), Structure and generation of turbulence at interfaces strained by internal solitary waves propagating shoreward over the continental shelf, *J. Phys. Oceanogr.*, *33*, 2093–2292.

Moum, J. N., J. M. Klymak, J. D. Nash, A. Perlin, and W. D. Smyth (2007b), Energy transport by nonlinear internal waves, *J. Phys. Oceanogr.*, *37*, 1968–1988.

Nagovitsyn, A., E. Pelinovsky, and Y. Stepanyants (1991), Observation and analysis of solitary internal waves in the coastal zone of the Sea of Okhotsk, *Soviet J. Phys. Oceanogr.*, *2*(1), 65–70.

Nash, J. D., M. H. Alford, and E. Kunze (2005), Estimating internal-wave energy fluxes in the ocean, *J. Atmos. Ocean. Tech.*, *22*(10), 1551–1570.

Nash, J. D., S. M. Kelly, E. L. Shroyer, J. N. Moum, and T. F. Duda (2012), The unpredictable nature of internal tides and nonlinear waves on the continental shelf, *J. Phys. Oceanogr.*, *42*(11), 1981–2000.

Ostrovsky, L. A. (1978), Nonlinear internal waves in the rotating ocean, *Oceanography*, *18*, 119–125.

Ostrovsky, L. A., and Y. Stepanyants (1989), Do internal solitons exist in the ocean?, *J. Geophys. Res.*, *27*, 2906–2926.

Pineda, J. (1991), Predictable upwelling and the shoreward transport of planktonic larvae by internal tidal bores., *Science(Washington)*, *253*(5019), 548–551.

Pineda, J. (1999), Circulation and larval distribution in internal tidal bore warm fronts, *Limnology and Oceanography*, pp. 1400–1414.

Sandstrom, H., and J. A. Elliott (1984), Internal tide and solitons on the scotian shelf: A nutrient pump at work, *J. Geophys. Res.*, *89*(C4), 6415–6426, doi: 10.1029/JC089iC04p06415.

Sandstrom, H., and N. S. Oakey (1995), Dissipation in internal tides and solitary waves, *J. Phys. Oceanogr.*, *25*, 604–614.

Schafstall, J., M. Dengler, P. Brandt, and H. Bange (2010), Tidal-induced mixing and diapycnal nutrient fluxes in the mauritanian upwelling region, *Journal of Geophysical Research: Oceans (1978–2012)*, *115*(C10).

Scotti, A., and J. Pineda (2004), Observation of very large and steep internal waves of elevation near the massachusetts coast, *Geophys. Res. Lett.*, *31*(L22307), 1–4.

Scotti, A., and J. Pineda (2007), Plankton accumulation and transport in propagating nonlinear internal fronts, *Journal of Marine Research*, *65*(1), 117–145.

Scotti, A., B. Butman, R. C. Beardsley, P. S. Alexander, and S. Anderson (2005), A modified beam-to-earth transformation to measure short-wavelength internal waves with an acoustic doppler current profiler, *J. Atmos. Ocean. Tech.*, *22*, 583–591.

Scotti, A., R. Beardsley, and B. Butman (2006), On the interpretation of energy and energy fluxes of nonlinear internal waves: an example from Massachusetts Bay, *J. Fluid Mech.*, *561*, 103–112.

Scotti, A., R. Beardsley, B. Butman, and J. Pineda (2008), Shoaling of nonlinear internal waves in massachusetts bay, *J. Geophys. Res.*, *113*(C08031).

Sharples, J., C. M. Moore, A. E. Hickman, P. M. Holligan, J. F. Tweddle, M. R. Palmer, and J. H. Simpson (2009), Internal tidal mixing as a control on continental margin ecosystems, *Geophysical Research Letters*, *36*(23), L23,603.

Shroyer, E., J. Moum, and J. Nash (2010a), Energy transformations and dissipation of nonlinear internal waves over new jersey's continental shelf, *Nonlinear processes in Geophysics*, *17*, 345–360.

Shroyer, E., J. Moum, and J. Nash (2011), Nonlinear internal waves over New Jersey's continental shelf, *J. Geophys. Res.*, *116*(C03022), 1–16.

Shroyer, E. L., J. N. Moum, and J. D. Nash (2010b), Vertical heat flux and lateral mass transport in nonlinear internal waves, *Geophysical Research Letters*, *37*(8).

Stansfield, K. C., C. Garrett, and R. Dewey (2001), The probability distribution of the Thorpe displacement within overturns in Juan de Fuca Strait., *J. Phys. Oceanogr.*, *31*, 3421–3434.

Stanton, T. P., and L. A. Ostrovsky (1998), Observations of highly nonlinear internal solitons over the continental shelf, *Geophys. Res. Lett.*, *25*(14), 2695–2698, doi: 10.1029/98GL01772.

Stastna, M., and K. Lamb (2002), Large fully nonlinear internal solitary waves: The effect of background current, *Physics of Fluids*, *14*, 2987.

Stepanyants, Y. (2006), On stationary solutions of the reduced ostrovsky equation: Periodic waves, compaction and compound solitons, *Chaos Solitons Fractals*, *28*, 193–204.

Venayagamoorthy, S., and O. Fringer (2012), Examining breaking internal waves on a shelf slope using numerical simulations, *Oceanography*, *25*(2), 132–139.

Wang, Y. H., C. F. Dai, and Y. Y. Chen (2007), Physical and ecological processes of internal waves on an isolated reef ecosystem in the South China Sea, *Geophys. Res. Lett.*, *34*, doi:10.1029/2007GL030658.

Waterhouse, A. F., S. E. Allen, and A. W. Bowie (2009), Upwelling flow dynamics in long canyons at low Rossby number, *Journal of Geophysical Research: Oceans (1978–2012)*, *114*(C5).

Winters, K. B., and R. Barkan (2013), Available potential energy density for boussinesq fluid flow, *Journal of Fluid Mechanics*, *714*, 476–488.

Zhang, S., and M. H. Alford (submitted), Instabilities in nonlinear internal waves on the washington continental shelf.

Zhang, S., M. H. Alford, and J. B. Mickett (submitted), Characteristics of nonlinear internal waves on the washington continental shelf, *Journal of Geophysical Research: Oceans*.

Zilberman, N. V., M. A. Merrifield, G. S. Carter, D. S. Luther, M. D. Levine, and T. J. Boyd (2011), Incoherent nature of m2 internal tides at the hawaiian ridge, *J. Phys. Oceanogr.*, *41*(11), 2021–2036, doi:10.1175/JPO-D-10-05009.1.

Appendix A

T-S FIT AND CALCULATION OF STRATIFICATION N^2

A piece-wise linear-fitted T-S relationship is obtained every 3 hours using time series of T and S at depths where both of them are sampled. The vertical motions of the waves during the 3-hour period fill in the T-S space sampled at the finite depths (Figure A.1a, colored crosses). Values of S at depths lacking salinity measurements are estimated by T measurements along the fitted line (Figure A.1a, black line). Buoyancy frequency $N = \sqrt{\frac{g}{\rho}\frac{d\rho}{dz}}$, where g is the acceleration due to gravity, ρ is the potential density, is calculated using observed and fitted T, S together. Full-depth T, S measurements from the glider when it was within 15 km of the mooring (Figure A.1b) provides a validation of the calculation. The fitted S profile and calculated N^2 profile from the mooring are in agreement with the glider observations (Figure A.1, de). Note that the salinity offset in the upper 30 m (Figure A.1, ad) is not a calibration error but a lateral gradient as displayed in the glider spatial measurements (not shown).

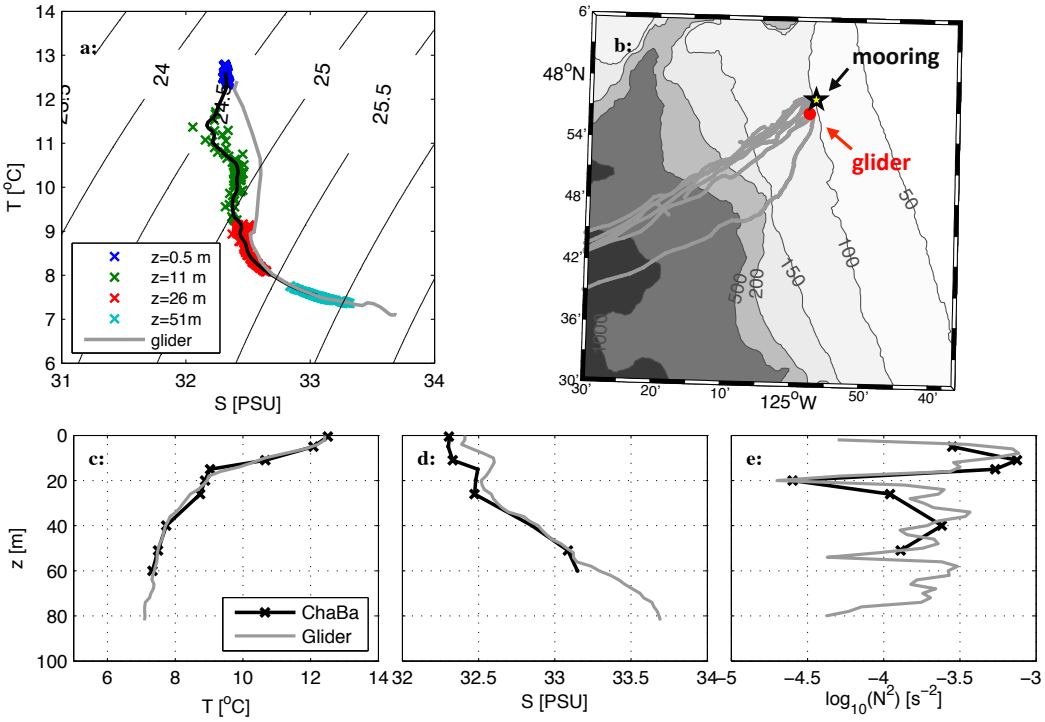

Figure A.1: (a) A piece-wise linear fit of salinity using 3-hour temperature (T) and salinity (S) measurements at depths $0.5, 11, 26$ and 51 m on Aug 9, 2010, when the glider 2.8 km from the mooring (b, red dot); (b) Locations of the mooring (star), glider lines (gray lines) and the position of glider (profiles in a); (c)-(e) comparing T, fitted S, and calculated stratification profiles from the mooring (black) and glider (gray), when the glider was at the position shown in (b).